ANALYSIS AND WIND TUNNEL TESTING OF A SUPERELASTIC

SLAT-COVE FILLER FOR AIRFRAME NOISE REDUCTION

A Thesis

by

WILLIAM DAVID SCHOLTEN

Submitted to the Office of Graduate and Professional Studies of
Texas A&M University
in partial fulfillment of the requirements for the degree of

MASTER OF SCIENCE

Chair of Committee,	Darren Hartl
Co-Chair of Committee,	Thomas Strgnanc
Committee Members,	Richard Malak
	Paul Cizmas
	Travis Turner
Head of Department,	Rodney Bowersox

December 2016

Major Subject: Aerospace Engineering

ABSTRACT

During low speed maneuvers, such as landing and approach, a significant portion of the noise generated by transport aircraft is due to airframe noise. The leading-edge slat is a primary source of airframe noise. Previous work has shown that the slat-cove filler (SCF) is effective at mitigating the noise generated by the slat. The objective of this work was to further the development of a superelastic shape memory alloy (SMA) SCF concept by investigating fluid-structure interaction (FSI) behavior via computational and physical models.

Structural optimization of a SCF design for a representative, transport-class airfoil was first conducted considering the SCF response to aerodynamic and slat retraction loads. The objective of the optimization was to minimize the actuation force needed to retract the slat and SCF. A monolithic SMA SCF was found to minimize the actuation force while satisfying constraints, which agreed with findings from prototype testing on the bench-top apparatus.

The success of the design optimization motivated further work that sought to determine how the SCF responded in flow using a combination of finite volume fluid models and finite element structural models based on a small-scale wind tunnel model of a conventional multi-element wing configuration with a SCF. Multiple angles of attack and deployment states of high lift devices were considered for computational fluid dynamics (CFD) analysis to gain an initial understanding of the flow around the wing. FSI analysis of the SCF in flow was conducted for multiple load cases using a framework that was compatible with custom material subroutines (for SMA material response). Wind tunnel testing of a physical model of the multi-element wing configuration was used to begin validation of the CFD and FSI models.

ii

ACKNOWLEDGEMENTS

TABLE OF CONTENTS

LIST OF FIGURES

viii

LIST OF TABLES

1. INTRODUCTION AND CONCEPT OF THE SMA SCF*

1.1   Introduction

One the main factors in wing design of conventional transport aircraft is cruise efficiency. At cruise and other high speed phases of flight, the wing must generate sufficient lift for steady level flight. However, in low speed phases of flight such as approach and landing, high-lift devices are deployed to improve the aircraft's lift and stall characteristics. High-lift devices typically include a leading-edge slat and a trailing edge flap. These high-lift devices, normally flush against the wing in cruise for reduced drag, present geometric discontinuities (gaps, edges, coves) to the airflow resulting in unsteadiness and the production of aeroacoustic noise. The noise produced by the leading-edge slat is the focus of this work.

Environmental and community noise is an ever-increasing problem because of continued growth of population in the vicinity of airports and growth in the air-transport industry itself. Reduction of noise produced by the slat has been studied for many years and a number of concepts have been proposed. Lockard and Khorrami used extended blade seals [1] while Dobrzynksi and Mau used a brush-based concept to mitigate the noise produced by the slat [2]. A third concept, proposed 14 years ago by Gleine and his coworkers was the slat-cove filler (SCF) [3]. The SCF fills the aft cavity of the deployed slat, modifying the airflow in such a way that its unsteadiness is reduced that in turn reduces aeroacoustic noise. Both experimental and computational results have shown that the SCF is effective at noise reduction [4, 5, 6]. It has furthermore been shown that a SCF shape that is dictated by

---

*Figure 1.1 is from "Development and Analysis-Drive Optimization of Superelastic Slat-Cover Fillers for Airframe Noise Reduction" by Scholten, W. and Hartl, D. and Turner, T. and Kidd, R.; reprinted by permission of the American Institute of Aeronautics and Astronautics, Inc.

the total pressure distribution between the slat and main wing at nominal landing conditions produces the maximum noise reduction. Development of the SCF concept was previously hindered by creating a SCF that could meet three conflicting goals common to morphing aerostructures [7]: i) compliance for morphing, ii) stiffness under aerodynamic loading, and iii) low weight. These conflicting design goals are illustrated in the requirement triangle of Fig. 1.1[8] (modeled after [7]).
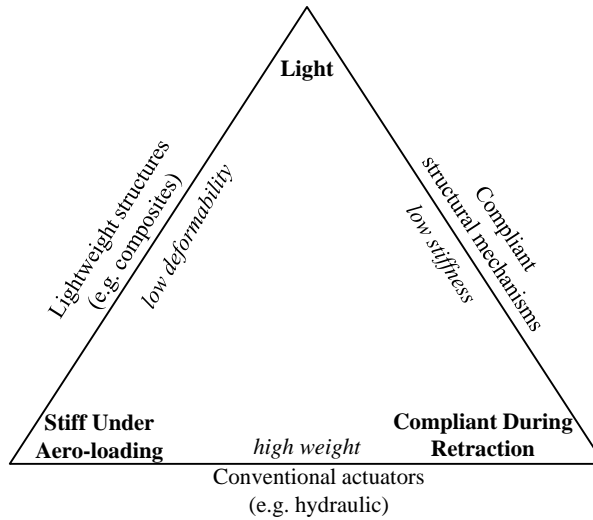
Figure 1.1: Morphing aero-structures requirement triangle.

In this work, shape memory alloys (SMAs), a type of active material, was incorporated into the design of the SCF. SMA materials have many qualities that make them suitable for morphing structure applications including a high energy density (for actuator applications) and an ability to undergo large amounts of recoverable deformation without yielding, allowing for a reduction in system complexity [9]. The legacy method of smart structures design required many expensive and protracted cycles of designing, constructing and testing physical models to reach an

2

optimal design. Using high-speed computational tools, analysis-driven optimization can be performed more efficiently to solve design problems involving SMAs. Many SMA design efforts using optimization techniques are discussed in a recent review [10, 11]. Gradient-based optimization has been used in applications such as SMA wire-actuated rotors [12] and active SMA panel structures [13]. Design optimizations using genetic algorithms have been considered in biomedical and aerospace applications. With regards to designs incorporating SMAs, genetic algorithms have been used in the design of spring actuation components [14] and structural damping mechanisms [15]. A design effort with goals similar to this work was the Boeing-developed variable geometry chevron (VGC) [16]. The goal of the VGC was to reduce the noise produced by the engine through modification of the exhaust nozzle airflow. Many optimization efforts [10, 11, 13] were motivated by the VGC's success. The design optimization methods developed in these efforts are incorporated into this work to find the optimal SCF design.

Morphing aerostructures, such as the SCF, can have significant effects on the surrounding airflow that in turn can affect the loading of the structure. To capture this interaction, fluid-structure interaction (FSI) analysis was considered. This type of analysis has been used for adaptive and morphing structures in many works. MacPhee and Beyene performed FSI analysis on a two-dimensional passive, morphing wind turbine blade under variable loading to demonstrate increased efficiency of passive morphing compared to conventional active control in wind energy conversion systems [17]. Similarly, Heo and coworkers investigated in-plane flexible properties of cellular structures and its use in a passive morphing airfoil application by constructing and analyzing a two-dimensional FSI model of an airfoil with a honeycomb core [18]. FSI analysis has also been incorporated into optimization frameworks. Maute and Reich performed design optimization of a quasi-three-dimensional adap-

tive wing section considering both structural and aerodynamic design criteria using a FSI model and compared the optimal design to another design from a conventional two-step approach [19]. A computational framework for the design and analysis of bio-inspired flapping wings was developed by Willis and coworkers, and design sweeps of models with varying fidelity models were conducted [20]. Daynes and Weaver developed and analyzed an FSI model of a morphing flap on a wind turbine blade for the purpose of load reduction and increased energy output. In addition, a wind tunnel model of the morphing flap was tested and the experimental results were compared to the FSI analysis [21].

Limited FSI analysis has been conducted on morphing structures incorporating SMAs. Nam and coworkers incorporated an SMA spar into a structural model of a wing and performed a parametric study of the design to assess effects of the SMA spar on wing performance[22]. Using FSI analysis, Strelec and coworkers developed and optimized the design of a morphing airfoil incorporating SMAs wire actuators that altered the airfoil shape to improve efficiency at various stages of flight. Strelec and coworkers also developed and tested a physical wind tunnel model of the optimal design [23]. Oehler and coworkers developed an FSI model of the Boeing VGC to better model the aeroelastic response of the VGC to airflow. Both the VGC tip deflection and nozzle pressure ratio were examined and compared to wind tunnel tests of the VGC [24].

While computational analysis is useful for understanding complex interactions (such as fluid-structure) and allows for efficient design optimization, validation of computational models using physical models is needed. For the SCF application in the present work, validation was done using a scaled wind tunnel model incorporating an SMA SCF. Some of the works previously described that featured FSI analysis with SMAs included wind tunnel testing [23, 24]. Many wind tunnel tests with

4

models incorporating SMAs are described in a recent review of SMA applications in morphing aircraft [25]. Ruggeri and coworkers tested a three blade rotor system with embedded SMA torque tubes that controlled the blade twist [26]. Kudva presents a summary of the DARPA Smart Wing Project that developed and tested a full span model with SMA-actuated leading and trailing edge control surfaces [27]. Singh and Chopra designed and tested a SMA wire-actuated tracking tab for a rotor blade to study its ability to reduce vibrations caused by differences in the rotor blades of a helicopter. Popov and coworkers investigated a morphing wing with SMA actuators that changed the shape of the overall wing [28].

1.2   SMA-Based Slat-Cove Filler Concept

As previously mentioned, a primary source for aeroacoustic noise on a typical transport aircraft is the leading-edge slat cove. The flow field in this region for a conventional airfoil at a typical landing condition is shown in Fig. 1.2. The flow bifurcates at the stagnation point resulting in two flows that follow the upper and lower surfaces of the slat. At the forward-most edge of the slat-cove, the lower portion of the flow separates resulting in a shear layer that later reattaches near the slat trailing edge. The shear layer encompasses a recirculating region of flow in the slat cove and supports considerable unsteadiness that are airframe noise sources.

Noise reduction is possible with the SCF due to the guiding of the flow in the vicinity of the deployed slat along a desired that removes removing the circulation within the slat-cove and the unsteady shear layer (see Fig. 1.3). The SCF profile shown in Fig. 1.3 is the contour dictated by total pressure and minimizes the flow unsteadiness and noise. When the slat is retracted for cruise, the SCF must sustain large deformations to allow the slat to nest tightly and cleanly with the main wing. The resulting strain in the SCF from the deformation (approximately 2-5% [29])
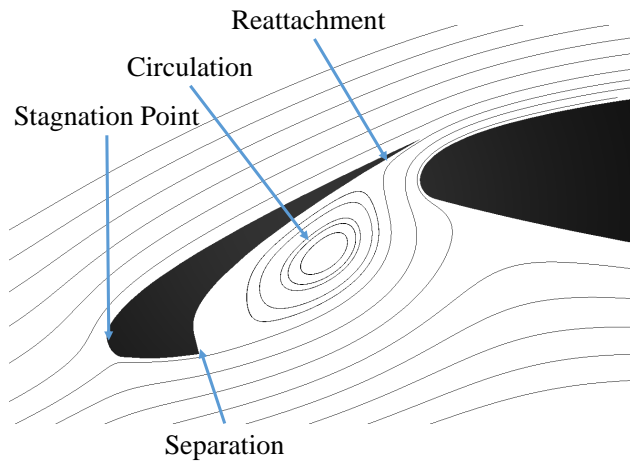
Figure 1.2: Illustration of flow in region of slat for conventional airfoil without SCF.
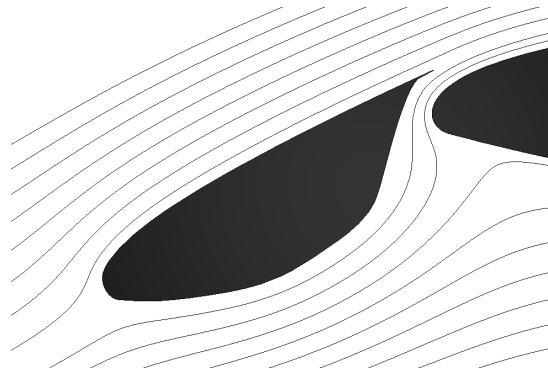
Figure 1.3: Illustration of flow in region of slat for conventional airfoil with SCF.

surpasses the limit of standard aerospace materials. This deformation, along with the previously mentioned requirement of stiffness under aerodynamic loading led to consideration of superelastic SMAs. This type of SMA is processed such that it is in the austenite phase while unloaded at normal operating temperatures. When given a sufficient applied stress, superelastic SMA undergoes a solid-to-solid phase transformation to the martensite phase allowing for large deformation. Once unloaded, the superelastic SMA undergoes a reverse transformation back into the austenite phase,

returning to its original configuration.

Retraction and deployment of the SMA SCF is shown in Fig. 1.4. The considered SMA SCF system includes the SCF, main wing, slat, and a hinge mounted on the slat cusp to assist with SCF retraction and deployment. As the slat is retracted from its fully deployed configuration (**1**), the SMA flexures of the SCF contact the main wing (**2**) causing localized stress in the flexure and in turn phase transformation from austenite to martensite. The localized transformation of the SMA flexures causes the SCF to deform into a configuration suitable for the small space between the slat and wing (**3** and **4**). During slat deployment (**5**), the SMA flexures are unloaded as the SCF loses contact with the wing, resulting in a return to the original configuration (**6**) if properly designed.
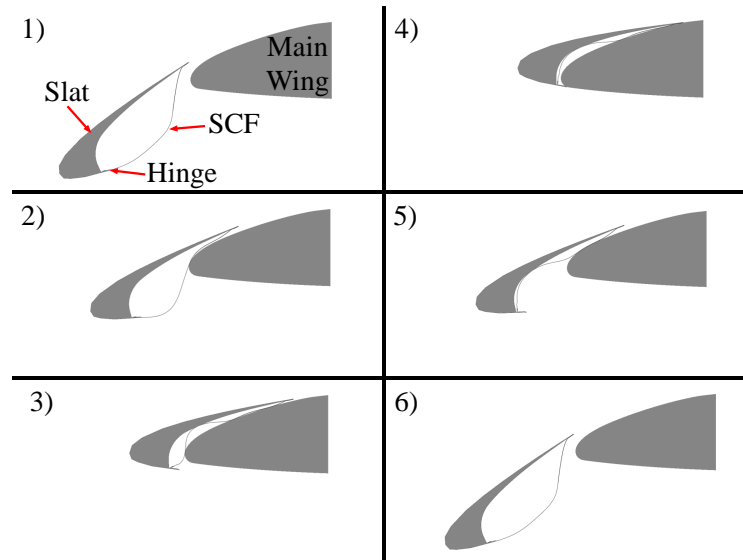
Figure 1.4: SMA SCF retraction/deployment.

Analyzing the stress on the SCF during retraction of the slat demonstrates the need for SMA materials in this application. Figure 1.5 shows the relation between

actuation force and percent retraction for SCFs made entirely out of SMA, steel, aluminum and titanium with scaled thicknesses such that each SCF has the same deflection from a representative static aerodynamic load.[1] Material properties for the SMA are from previous work [8] while the properties for the other materials are from the Metallic Materials Properties Development and Standards database [30]. As shown in Fig. 1.5, with scaled thicknesses, the SCFs have approximately the same actuation force curve. The sharp drop in moment near 90% retraction is due the hinge snapping into its retracted position. The hinge snap is a dynamic event in the quasi-static analysis and resulting drop in moment should not be not be trusted. Note that the SMA SCF has a higher moment past 80% retraction due to contact between main wing and slat. he The trailing edge of the SCFs made out of typical standard materials were able to fit in the small space between the leading edge of the main wing and trailing edge of the slat better than the SMA SCF since they were thinner. Examining the stress in each SCF shows that every standard material SCF exceeds the yield stress. The steel and aluminum SCFs exceeded the yield stress at relatively the same percentage of retraction (21.6% for steel and 22.4% for aluminum). The titanium SCF successfully retracts but exceeds the yield stress at full retraction. Some adjustments could be made to the slat-cove to slightly lower the stress on the titanium SCF. However, the titanium SCF would still be loaded to high levels of stress that overtime could be detrimental. The yielding of the standard material SCFs is due to large amount of strain encountered during retraction. Standard aerospace materials have a linear relation between stress and strain until the onset of plasticity while SMAs exhibit a hysteresis effect allowing for large amounts of recoverable inelastic strain (see Fig. 1.6).

---

[1]The thicknesses for the SMA, steel, aluminum and titanium were 0.0762 mm, 0.00481 mm, 0.0681 mm and 0.05825 mm, respectively.
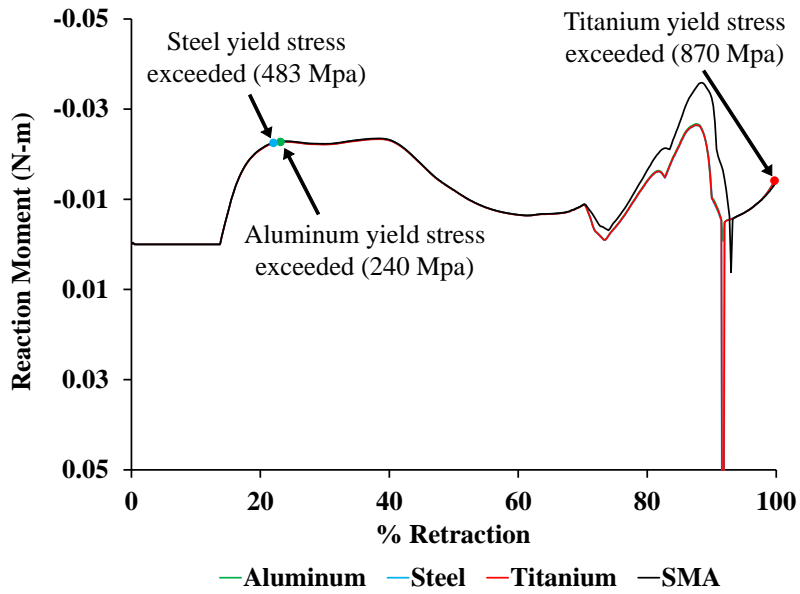
Figure 1.5: Actuation force vs. % retraction for SMA and standard material SCFs.
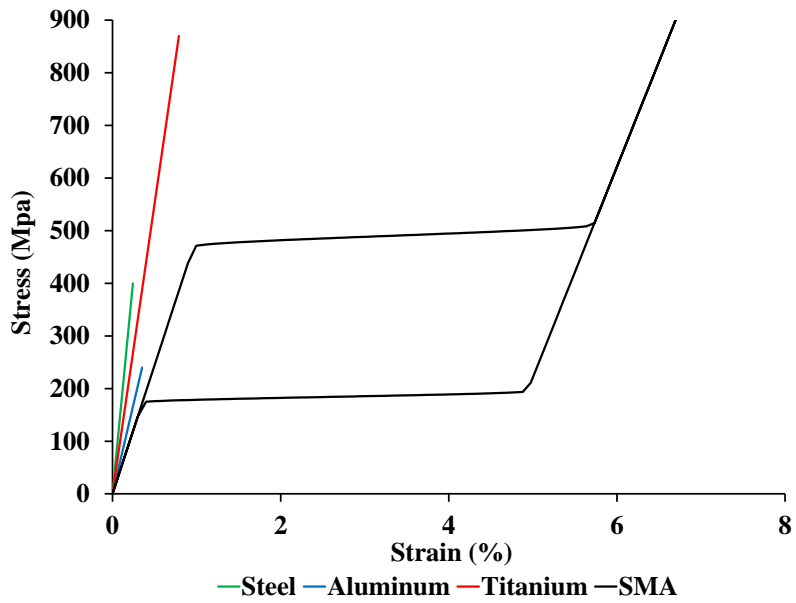
Figure 1.6: Comparison of stress-strain curves for SMA and typical materials.

9

1.3   Physical Bench-top Model

Previous work done by NASA engineers regarding the SCF concept focused on the development of a physical bench-top model of the SCF [29]. Initial designs of the SCF featured elastomers and SMA wires, but the results from those models led NASA engineers to consider SMA sheet-based designs. Section 1.3 will describe the development of the SMA sheet-based SCF bench-top model that was the template for all models developed in the current work.

Figure 1.7 shows a schematic of SMA sheet-based concept. The sheet of superelastic SMA material would be heat treated (shape set) into a stress-free form that matched the desired (total pressure) SCF contour in the deployed configuration, as shown by the red contour in Fig. 1.7. To accommodate the contact of the slat cusp with the main wing in the retracted configuration, a conventional hinge was introduced at the location of the lower attachment between the slat and the SCF. A lap joint between the hinge arm and the SCF positioned the outer surface of the SCF flush with the slat at the cusp. Another lap joint between the slat trailing edge and the SCF accommodated the tight clearance between the main wing and slat trailing edge during retraction.

During retraction, the SCF was envisioned to deform by transforming to the martensite phase in areas of high stress. The contact between the main wing and the SCF was such that stress was initially concentrated near the SCF trailing edge and transformation initialized there. Transformation ensued elsewhere adaptively in regions of high stress to allow the SCF to deform and conform to the main wing, thus accommodating the deformation requirement. By choosing the appropriate transformation characteristics and geometric parameters, the force needed to stow the SCF could be minimized. Proper storage of recoverable strain energy in the
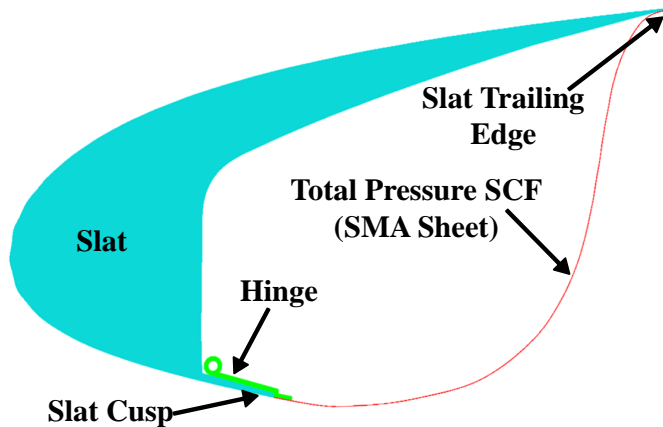
Figure 1.7: Deformable, thin-shell SCF schematic.

SMA during retraction enabled autonomous deployment of the SCF when the slat was moved away from the wing. While in the deployed configuration and under aerodynamic loads, transformation was not anticipated and the SCF was expected to maintain its shape due to the relatively moderate magnitude and smooth distribution of the aerodynamic load applied normally to the surface of the curved (and thus inherently stiff to the aerodynamic load) SMA structure.

It was unknown at the initiation of concept development if a single monolithic SMA flexure was feasible for use as a slat-cove filler. Cost savings and potential retract/deploy kinematic advantages might be realized by including stiffened regions in the SCF. Thus, a parametric study was planned to examine the design space in terms of the number of deforming and non-deforming SCF regions, their thicknesses, and their sizes in order to minimize the force needed to retract the slat-SCF assembly. Feasible designs also needed to retain proper retraction and self-deployment functionality and exhibit sufficiently high SCF stiffness given an applied, static aerodynamic load when deployed.

Initial SCF work used large (75% scale) physical apparatuses to test various SCF

11

designs. For the shell-based SCF design, physical apparatus with a 1.9 cm span (effectively making it a 2-D prototype) was used (see Fig. 1.8). This enabled a faster and less expensive parametric study of the superelastic SMA concept and was more compatible with available SMA forms. Bearings were mounted underneath the slat that, when moved within machined slots in the baseplate, enforced proper 2-D kinematics between the leading edge of the main wing and the slat.
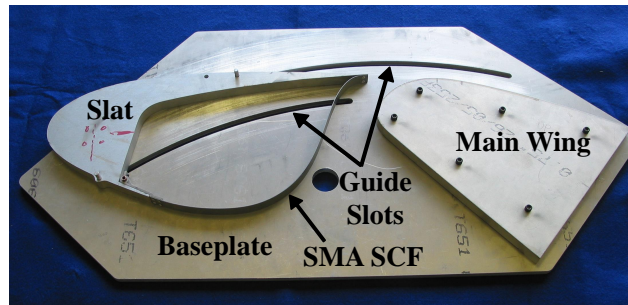
Figure 1.8: Bench-top apparatus used in parametric study of SCF prototypes incorporating SMA flexures.

Superelastic SMA flexures that were shape-set to the total pressure SCF profile were obtained in thicknesses ranging from 0.51 mm to 1.27 mm (increments of 0.127 mm). The heat treatment and composition of the flexures gave them a superelastic response at room temperature.

Initial work using the simplified bench-top apparatus of Fig. 1.8 led to two prototypes: a) the long hinge monolithic-SMA prototype (Fig. 1.8 and Fig. 1.9(a)), which consisted of one superelastic SMA flexure and b) the multi-flexure prototype (Fig. 1.9(b)), which consisted of a forward SMA flexure, a non-deforming intermediate link (mid-link), and an aft SMA flexure. In either design, the hinge arm was configured such that SCF stowage space and mobility were maximized. It was

qualitatively found that the long hinge monolithic prototype, being in general more flexible, required less force during retraction than the multi-flexure prototype. In fact, the increase in compliance (and associated decrease in actuator load) during retraction motivated a further reduction in hinge length, resulting in a third design: *c*) the short hinge monolithic SCF (Fig. 1.9(c)). The length of the hinge arm was minimized by creating the abrupt "z-curve" in the SMA flexure needed to maintain a continuous outer mold line at the slat cusp (inset of Fig. 1.9(c)).

(a) Long hinge monolithic SMA SCF.

(b) Multi-flexure SMA SCF.

(c) Short hinge monolithic SMA SCF.
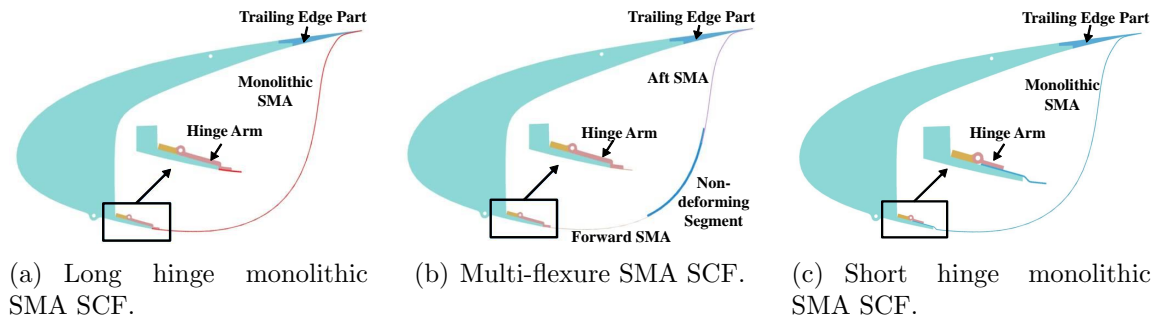
Figure 1.9: FEA model of SCF assembly (mesh hidden).

The multi-flexure design clearly required consideration of more design variables and thus provided more design flexibility in balancing the stowage force versus the resistance to aerodynamic loading and in adjusting the kinematics of retraction and deployment. The multi-flexure SCF prototype consisted of three components: a 0.51 mm forward SMA flexure, a 1.02 mm aft SMA flexure, and a non-deforming mid-link. Each component spanned roughly 1/3 of the overall curvilinear length of the SCF profile. This configuration was found to provide the best compromise regarding design goals for the multi-flexure designs considered; a change in the thickness of either SMA flexure resulted in unacceptable shifts in the balance between compliance during stowage and stiffness under aerodynamic loading. The retraction and

deployment sequence for the multi-flexure design is shown in Fig. 1.10. Note that, although this multi-flexure SCF retracted into the slat cavity with acceptable force, no such configuration tested would self-deploy without the installation of additional components (e.g., a restoring spring), which would increase both retraction force and system complexity.
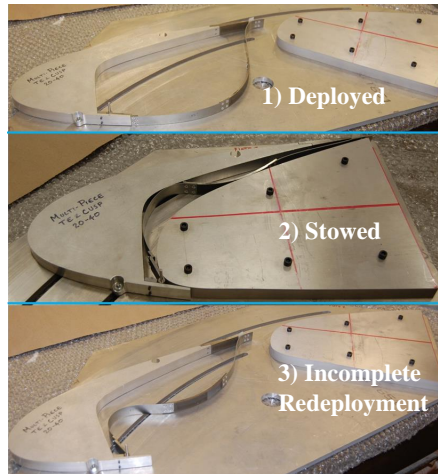
Figure 1.10: Multi-flexure-SMA SCF with 0.51 mm thick forward flexure and 1.02 mm thick aft flexure: 1) deployed, 2) stowed and 3) redeployed (exhibiting bi-stable behavior).

Both the longe hinge monolithic (baseline) and the short hinge monolithic prototypes employed a continuous 1.02 mm thick SMA flexure. Both autonomously redeployed and met the contradictory stowage compliance and aeroelastic stiffness requirements. Figure 1.11(a) and Fig. 1.11(b) show the retraction and deployment of the two monolithic prototypes. The short hinge prototype exhibited a noticeable decrease in stowage force (measured qualitatively) relative to the long hinge due to the additional length of compliant SMA. Both designs had a similar response to a distributed force configured to approximate the aerodynamic load. During physi-

cal prototype testing the load was approximated using shot bags. Having shown smooth response, successful self-deployment, and sufficient aeroelastic stiffness, the short hinge monolithic concept was deemed superior to other design configurations tested.
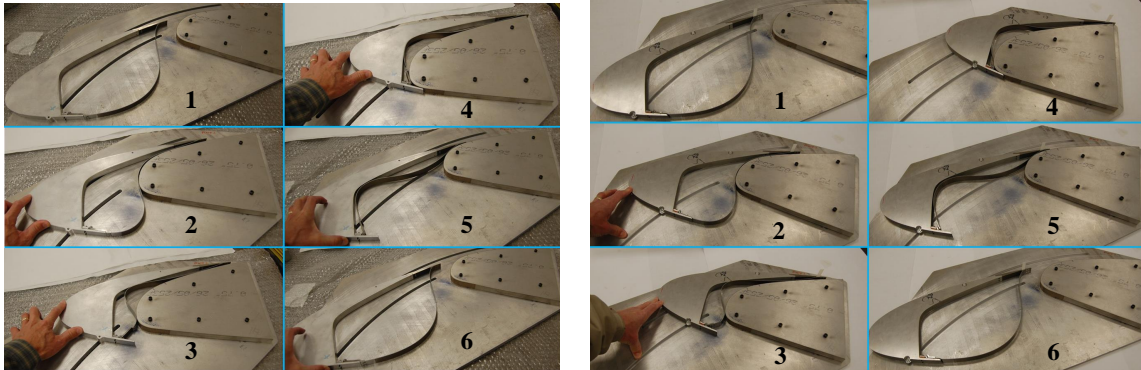
(a) Long hinge monolithic. (b) Short hinge monolithic.

Figure 1.11: Monolithic prototypes with 1.02 mm flexure thickness: 1) deployed, 2) SCF flexing around leading edge, 3) hinge clearing leading edge, 4) stowed, 5) slat at ∼75% redeployment and 6) autonomously redeployed.

1.4 Research Issues

There are important research issues concerning the development of the SCF that must be addressed. These issues include the balancing of the three conflicting design goals (stiffness to aerodynamic loads, compliance to retraction/deployment and low weight), the behavior of the SMA SCF in flow, the sensitivity of the SMA SCF to changes in temperature and the manufacturing of the SMA SCF.

Due to the hysteresis of SMAs, incorporating SMAs into the SCF design provides a means to meet the requirements of light weight, stiffness to aerodynamic loading, and compliance to retraction/deployment. However, the SMA SCF must be designed

correctly. An overly stiff SMA SCF would meet the design requirements during aerodynamic loading, but could require an actuation force that exceeds the maximum force in current slat actuation systems or it could damage the main wing resulting in significant loss of aerodynamic effectiveness. In addition, overly stiff designs may yield during retraction due to the increased stress. Conversely, a very compliant SMA SCF design will meet the retraction/deployment requirement, but may be unable to maintain its shape under aerodynamic loading, potentially compromising structural stability or limiting the noise mitigation effectiveness. The incorporation of SMAs into the SCF design allows allows for the possibility of designs that can meet the three conflicting requirements, but fail in the autonomous redeployment of the SMA SCF due to bi-stability. Satisfaction of the three requirements in addition to autonomous redeployment are addressed by performing design optimizations of the SMA SCF.

The second issue is understanding the behavior of the SMA SCF in flow. Currently, all wind tunnel tests related to the SMA SCF have used rigid models. It is unknown how the SMA SCF will behave in flow. Airflow could either assist or hinder the retraction and deployment of the SMA SCF. In addition, since the SMA SCF is a thin shell spanning the length of the wing, it may vibrate which could produce as much noise as the wing without the SMA SCF. Performing both wind tunnel tests and fluid structure interaction (FSI) analysis of a high-lift wing with a flexible SMA SCF would assist in the understanding of the SMA SCF in flow. These tests are not trivial. Scaled wind tunnel models can be difficult to manufacture due to part sizes. Fastened, brazed or welded joints at full scale may be limited to adhesive joints at model scale. Computational FSI analysis will require a complex model that can handle many complicated features such as contact, large deformation, nonlinear materials, turbulent fluid flow and CFD mesh adaptation (including elimination of fluid volume) due to airfoil reconfiguration.

The third issue for the SMA SCF research is the sensitivity of the SMA SCF to temperature changes. This issue is significant since transport aircraft can undergo a wide range of temperatures depending on the flight origin and destination. Material response of SMAs, such as the transformation temperatures, are highly dependent on the operating temperature, potentially effecting the performance of the SMA SCF. In addition if the temperature is low enough, the SMA could transform prematurely into the martensite phase with no loading, ruining the superelastic effect. The SMA material for the SCF will need to have a composition and training such that it minimizes its sensitivity to temperature. Alternatively, there will need to be a temperature control system that can maintain the temperature of the SMA material at the optimal condition.

The final issue for the development of the SMA SCF is the physical implementation of the SMA SCF. Current physical full scale models of the SMA SCF have only been a few inches in span. At wind tunnel scales, this is not an issue since the curvilinear length of the SMA SCF will only be a few inches. At full scale the SMA SCF system will span almost the entire length of the wing. This size exceeds what current SMA (specifically NiTi) manufacturers can achieve. This issue will be resolved as SMA manufacturing processes improve. However, using current technology the full scale operational SCF will have to be created in small spanwise slices.

1.5   Research Objectives and Plan

This research will focus specifically on development and understanding of the SMA SCF using both computational and physical models. The following is a list of objectives for the research presented in this document.

- Develop a structural model of the SMA-SCF and perform design optimization considering both aerodynamic and retraction/deployment load cases.

- Develop and analyze CFD and FSI models of a scaled SCF for a conventional high-lift system at various angles of attack and slat/flap deployment.

- Develop and test a scaled wind tunnel model of the SCF for a conventional high-lift system to validate computational models using experimental results.

A finite element structural model of the full scale SMA SCF, based on the physical model developed by NASA [29], will be presented and used to analyze the SCF response to aerodynamic and slat retraction loads with the goal of optimization. The objective of the optimization will be the minimization of the actuation force needed to retract the slat-SCF assembly while subject to constraints involving aeroelastic deflection of the SCF when deployed, maximum stress in the SMA flexures, autonomous deployment of the SCF during slat deployment. The design optimization will consider the SMA flexure thicknesses and lengths of various SCF components as design variables. The results of design of experiment (DOE) studies will be presented and used to guide the optimization.

The wind tunnel model will be presented and is based on a 2D section from the mid-span of the outboard slat on the Common Research Model (CRM) [31] with a SCF for the specific section. The CRM is a theoretical wing developed by Boeing and NASA with available geometry (fixed wing and multiple slat/flap positions) and computational fluid dynamics (CFD) results that can serve as validation checks for early CFD and FSI models of the SCF. The wind tunnel model consists of 3D printed and metal "off-the-shelf" parts. In addition, actuators are used to simulate the retraction and deployment of the slat and flap. Results from wind tunnel tests at various angles of attack and slat/flap deployment will be presented. Results will include measurements of lift and drag using load cells, SCF deflection using a laser displacement sensor and pressure at discrete points on the main wing using a

Scanivalve system. An FSI model of the scaled wind tunnel model, created using a combination of Abaqus (structural solver) and SC/Tetra (fluid solver), will be presented. The FSI model will be analyzed at flow conditions, angles of attack and slat/flap deployment levels similar to the wind tunnel tests. The FSI model has provisions to accommodate the large deformations of the SCF and to capture the SMA material response. The FSI analysis will present more data regarding the behavior of the SCF in flow. Deflection data for the entire SCF profile will be presented from the FSI analysis while only data for discrete points will be presented from the wind tunnel tests. In addition, the pressure and velocity distributions throughout the entire tunnel will be presented from the FSI analysis. The FSI results will compared and correlated with the experimental results (lift, drag, SCF displacement) from the wind tunnel tests.

2. STRUCTURAL MODEL DEVELOPMENT AND ANALYSIS-DRIVEN OPTIMIZATION OF BENCHTOP SCF MODEL*

The first part of this work was a computational study of the superelastic SMA SCF concept. The ultimate goal of this computational study was a design optimization of the SCF. In this section the computational framework and analytical model of the SCF are presented, followed by a discussion of the design variables, goals and constraints of the design optimization. Results from the investigation of design variable influence are discussed and optimization results are presented.

2.1 Structural Model and Computational Framework

In Section 2.1, the creation of a capable computational framework and a representative structural model subjected to meaningful load cases are discussed. The superelastic SMA SCF benchtop prototype served as a basis for the development of the computational model. Computational analysis offered a more efficient way to examine the SCF designs compared to the long and expensive physical development.

2.1.1 Computational Framework

To analyze various morphing structure configurations for the purpose of obtaining an optimal design, an efficient computational analysis framework was needed. The chosen framework made use of a combination of a commercial finite element analysis (FEA) suite (Abaqus) [32] and custom constitutive model implementations for the SMA that included algorithms intended to decrease runtime. A simulation process management tool (ModelCenter) [33] was then used to automate this combination

---

*This section was from "Development and Analysis-Drive Optimization of Superelastic Slat-Cover Fillers for Airframe Noise Reduction" by Scholten, W. and Hartl, D. and Turner, T. and Kidd, R.; reprinted by permission of the American Institute of Aeronautics and Astronautics, Inc.

[10] such that desired FEA models representing trial designs were automatically generated and analyzed. A likewise automated post-processor was used to extract local and global analysis results associated with each trial design, these being passed to the optimization algorithm that considered model response and fulfillment of design requirements to determine new trial configurations to be analyzed.

SMA materials exhibit complex thermomechanical behaviors that require the use of specialized constitutive models. For this work, the phenomenological constitutive model based on continuum thermodynamics by Lagoudas, Hartl, and coworkers [34] was utilized. This model was implemented in Abaqus as a Fortran custom User MATerial (UMAT) subroutine and calibrated using experimental data. The overall analysis-driven design framework was flexible and allowed for various FEA tools, constitutive models, or simulation process managers to be substituted.

2.1.2 Constitutive Model Description

A general description of the constitutive model for the behavior of the SMA flexures is provided. A more detailed description can be found elsewhere [35]. The constitutive model considers two tensorial external state variables, stress $\boldsymbol{\sigma}$ and strain $\boldsymbol{\varepsilon}$, in addition to the scalar, absolute temperature T. The two internal state variables, the scalar martensitic volume fraction ξ and the recoverable inelastic transformation strain tensor $\boldsymbol{\varepsilon}^t$, account for the microstructural state of the SMA. The temperature and total strain are assumed to be given values in displacement-driven FEA, leaving three unknowns (total of 13 scalar components) to be calculated. Additive strain decomposition is assumed per

$$\boldsymbol{\varepsilon} = \boldsymbol{S}(\xi)\boldsymbol{\sigma} + \boldsymbol{\alpha}(T - T_0) + \boldsymbol{\varepsilon}^t, \tag{2.1}$$

where T_0 is a reference temperature, $\boldsymbol{S}(\xi)$ is the phase-dependent, fourth-order com-

pliance tensor, and $\boldsymbol{\alpha}$ is the second-order coefficient of thermal expansion tensor. $\boldsymbol{S}(\xi)$ is calculated by the rule of mixtures via

$$\boldsymbol{S}(\xi) = \boldsymbol{S}^A + \xi(\boldsymbol{S}^M - \boldsymbol{S}^A). \tag{2.2}$$

The time rate of change of the inelastic transformation strain can be determined by

$$\dot{\boldsymbol{\varepsilon}}^t = \dot{\xi}\boldsymbol{\Lambda}^t; \qquad \boldsymbol{\Lambda}^t = \begin{cases} H\frac{3}{2}\frac{\boldsymbol{\sigma}'}{\bar{\sigma}} & \dot{\xi} > 0 \\ \frac{\boldsymbol{\varepsilon}^{t-r}}{\xi^r} & \dot{\xi} < 0 \end{cases}, \tag{2.3}$$

where $\boldsymbol{\Lambda}^t$ is the transformation direction tensor, $\boldsymbol{\sigma}'$ is the deviatoric stress tensor, and H is the maximum uniaxial transformation strain. During forward transformation from austenite to martensite (i.e., during loading or retraction; $\dot{\xi} > 0$), transformation strain is generated as in Mises plasticity. The Mises equivalent stress $\bar{\sigma}$ is given as

$$\bar{\sigma} = (\frac{3}{2}\boldsymbol{\sigma}' : \boldsymbol{\sigma}')^{1/2}, \tag{2.4}$$

In reverse transformation (unloading or deployment; $\dot{\xi} < 0$), the transformation strain direction and magnitude are specified in such a way that the transformation strain present at the end of forward transformation is fully recovered, allowing the SMA to fully transform back into austenite. The memory variables $\boldsymbol{\varepsilon}^{t-r}$ and ξ^r are the transformation strain tensor and the martensitic volume fraction at transformation reversal, respectively.

The criteria for phase transformation during loading and unloading is quantified by the transformation function Φ^t. The constraints on the evolution are specified as

$$\Phi^t \leq 0, \qquad \dot{\xi}\Phi^t = 0, \qquad 0 \leq \xi \leq 1. \tag{2.5}$$

The martensitic volume fraction can only range from 0 (pure austenite) to 1 (pure martensite). Due to the different stress levels inducing forward and reverse transformation, the branched form of Φ^t is considered, given by

$$\Phi^t = \begin{cases} \Phi^t_{fwd}; & 0 \leq \xi < 1; \quad \dot{\xi} \geq 0 \\[2mm] \Phi^t_{rev}; & 0 < \xi \leq 1; \quad \dot{\xi} \leq 0 \end{cases}. \tag{2.6}$$

The forward transformation function is given as

$$\begin{aligned} \Phi^t_{fwd} &= (1-D)H\bar{\sigma} + \tfrac{1}{2}\boldsymbol{\sigma} : \tilde{\boldsymbol{S}}\boldsymbol{\sigma} + \rho\tilde{s}_0 T - \rho\tilde{u}_0 \\ &\quad - \left[\tfrac{1}{2}a_1(1 + \xi^{n_1} - (1-\xi)^{n_2}) + a_3\right] - Y_0^t, \end{aligned} \tag{2.7}$$

while the reverse transformation function is given by the following

$$\begin{aligned} \Phi^t_{rev} &= -(1+D)\frac{\boldsymbol{\sigma}:\boldsymbol{\varepsilon}^{t-r}}{\xi^r} - \tfrac{1}{2}\boldsymbol{\sigma} : \tilde{\boldsymbol{S}}\boldsymbol{\sigma} - \rho\tilde{s}_0 T + \rho\tilde{u}_0 \\ &\quad + \left[\tfrac{1}{2}a_2(1 + \xi^{n_3} - (1-\xi)^{n_4}) - a_3\right] - Y_0^t \end{aligned} \tag{2.8}$$

The parameters $\boldsymbol{S}_A$, $\boldsymbol{S}_M$, $\boldsymbol{\alpha}$, $\rho\tilde{s}_0$, $\rho\tilde{u}_0$, Y^t, D, a_1, a_2, a_3, n_1, n_2, n_3, and n_4 are calibrated using the method described in Section 2.1.3.

2.1.3 Constitutive Model Parameters and Calibration

The constitutive model was calibrated using experimental data from tension tests (per F-2516 ASTM standard [36]) on superelastic SMA supplied and tested by Johnson Matthey Inc. that was used in the physical benchtop model described in the previous section. Figure 2.1 shows the stress-strain diagram for this material.

The thermoelastic behavior is described by $\boldsymbol{S}_A, \boldsymbol{S}_M$, and $\boldsymbol{\alpha}$ (Equations (1) and (2)), which are easily calibrated using standard isotropic forms [37, 38]. The maximum magnitude of the evolving transformation strain is described by the scalar H; in this study is assumed to be a constant. It is common to employ a stress-
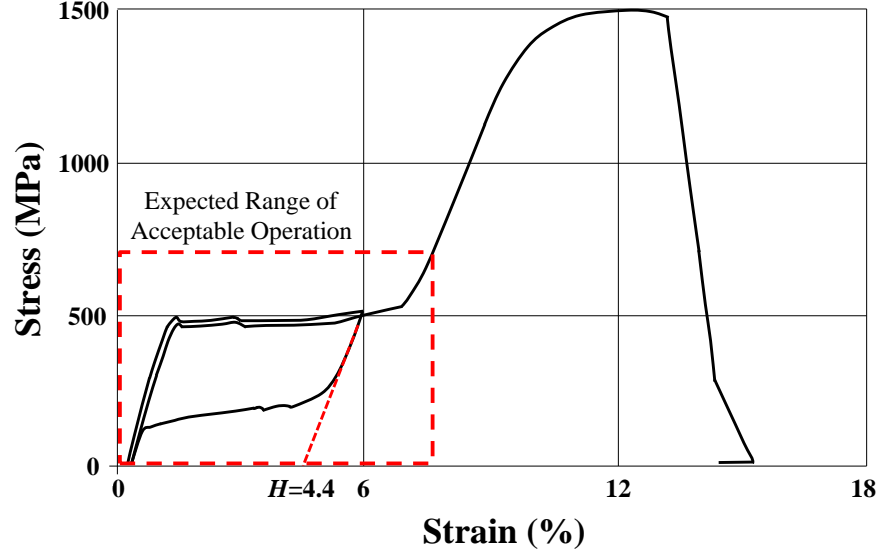
Figure 2.1: Stress-strain data of the superelastic SMA material used for full scale models.

temperature *phase diagram* to graphically describe the transformation criterion and then to calibrate the thermodynamic model parameters (D, Y_0^t, $\rho\tilde{u}_0$, $\rho\tilde{s}_0$, a_1, a_2, and a_3). The phase diagram assumed for the SMA material used in this portion of the work (cf. Fig. 2.1) is shown in Fig. 2.2. The slanted pairs of lines denote the transformation limits and have slopes C_M and C_A for forward and reverse transformation, respectively. The constitutive model is formulated to consider the zero stress transformation temperatures (M_s, M_f, A_s, A_f).
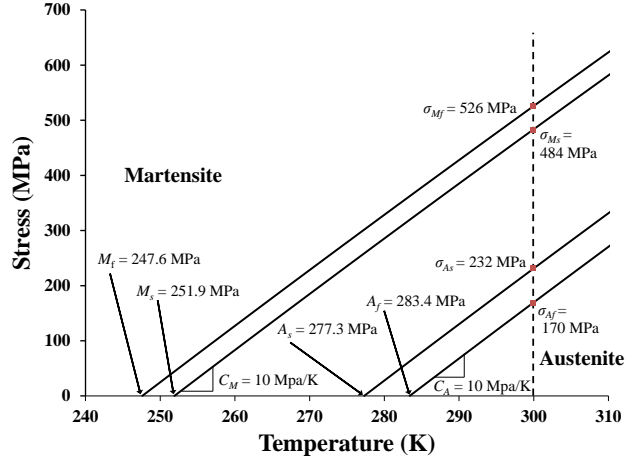
Figure 2.2: Phase diagram of SMA material associated with the calibrated constitutive model.

Knowing the value of H (see Fig. 2.1) and the properties from the phase diagram (Fig. 2.2), the criteria for the transformation criterion Φ^t_{fwd} and Φ^t_{rev} are calibrated as shown [35]:

$$a_1 = \rho \tilde{s}_0 (M_f - M_s), \tag{2.9}$$

$$a_2 = \rho \tilde{s}_0 (A_s - A_f), \tag{2.10}$$

$$a_3 = -\frac{a_1}{4}\left(1 + \frac{1}{n_1 + 1} - \frac{1}{n_2 + 1}\right) + \frac{a_2}{4}\left(1 + \frac{1}{n_3 + 1} - \frac{1}{n_4 + 1}\right), \tag{2.11}$$

$$\rho \tilde{u}_0 = \frac{\rho \tilde{s}_0}{2}\left(M_s + A_f\right), \tag{2.12}$$

$$Y_0^t = \frac{\rho \tilde{s}_0}{2}\left(M_s - A_f\right) - a_3, \tag{2.13}$$

$$\rho \tilde{s}_0 = \frac{-2H\left(C_M C_A\right)}{\left(C^M + C^A\right)}, \tag{2.14}$$

$$D = \frac{\left(C_M - C_A\right)}{\left(C_M + C_A\right)}. \tag{2.15}$$

The transformation hardening coefficients parameters n_1, n_2, n_3, and n_4 are selected such that the best fit for the four corners of the transformation hysteresis can be obtained.

The material properties for the SMA material considered in this portion of the work are shown in Table 2.1. Properties were based on the tension tests (E_A, E_M, M_s, M_f, A_s, A_f and H) or were assumed to be a typical value for this type of material (ν_A, ν_M, C^A, C^M and ρ). These properties were validated by superimposing the hysteresis loop generated by the calibrated model onto experimental results as shown in Fig. 2.3.[1] Clearly the hysteresis loop generated by the model matches the experimental response closely.
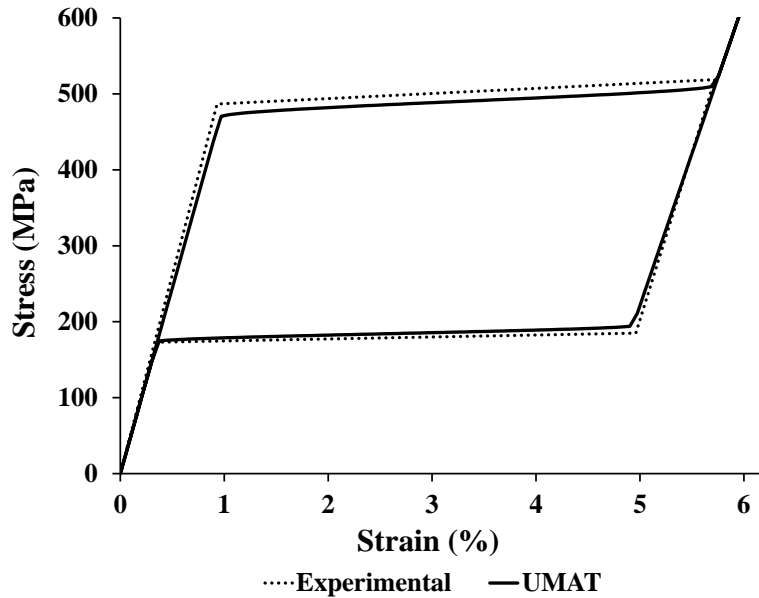
Figure 2.3: Hysteresis loop generated using calibrated model and superimposed on the experimental data.

---

[1]The experimental hysteresis loop in Fig. 2.3 was produced by plotting only key stress-strain points from Fig. 2.1 to facilitate comparison with the data from the constitutive models.

Table 2.1: SMA material properties for full scale models.

Property	Value
(Elastic Properties)	
E_A, E_M	48.9 GPa, 40.0 GPa
$\nu_A = \nu_M$	0.33
(Phase Diagram Properties)	
M_s, M_f	251.9 K, 247.6 K
A_s, A_f	277.3 K, 283.4 K
$C^A = C^M$	10.0 MPa/K
(Transformation Strain Properties)	
$H = H_v$	4.4%
(Smooth Hardening Properties)	
n_1, n_2, n_3, n_4	0.5
(Other Properties)	
ρ	6480 kg/m^3
$\alpha_M = \alpha_A$	0

2.1.4   FEA Model

The three-dimensional finite element model was based on the simplified physical bench-top prototype and can be seen in Fig. 2.4(a). The main wing, slat and hinge arm were considered to be non-deforming, though the slat and hinge arm could undergo rigid body motion. The hinge arm was able to freely rotate about the hinge axis through the use of a connector element. The SCF was attached to the mating surfaces of the hinge arm and the slat near the trailing edge through "contact tie" constraints. The entire SCF was modeled as a single geometric part in Abaqus, where partitions were used to subdivide the overall SCF into four sections; the SCF-hinge

arm (stiff), the forward SMA flexure, the aft SMA flexure, and the mid-link (stiff) (see Fig. 2.4(b)). These partitions were defined through the use of parametrized datum planes, which will be subsequently referred to as partition planes, such that the lengths of the SCF sections could be easily adjusted through the specification of these design variables in the scripted model, as shown in Fig. 2.5.

(a) Overall assembly.

(b) Sections of the SCF.
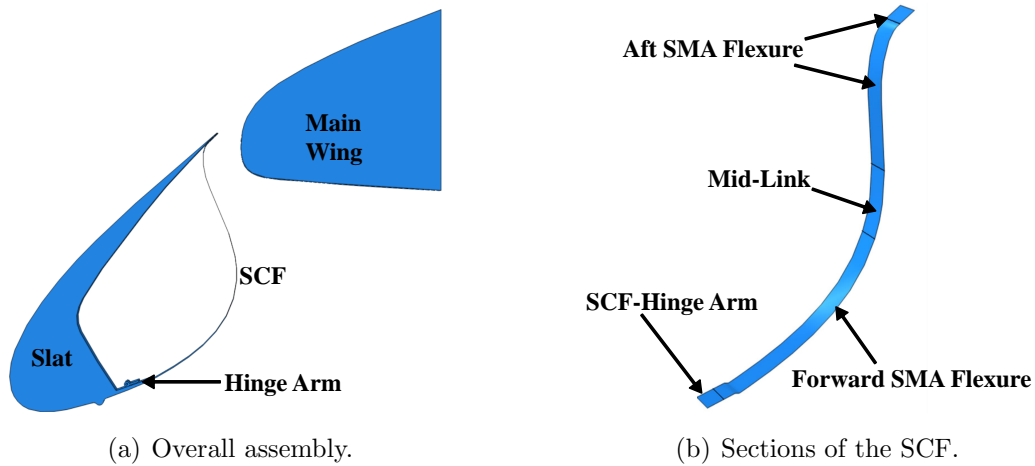
Figure 2.4: FEA model of SCF assembly (mesh hidden).

The location of each partition plane was determined by its offset from the preceding plane, preventing section inversion. Upper and lower bounds on these offset parameters prevented unreasonable designs. To model different lengths of the hinge arm, the length of the SCF-hinge arm section was adjusted by moving the "SCF-hinge" plane and assigning this small partition of the SCF stiff (nearly rigid) elastic properties to approximate the hinge arm. The rigid hinge arm part shown in Fig. 2.5, for example, represented the smallest hinge arm length considered (1.52 cm). Monolithic designs could be considered by allowing the length of the mid-link (i.e., the offset between the "Mid-Link" and "Forward SMA" planes) to be reduced to
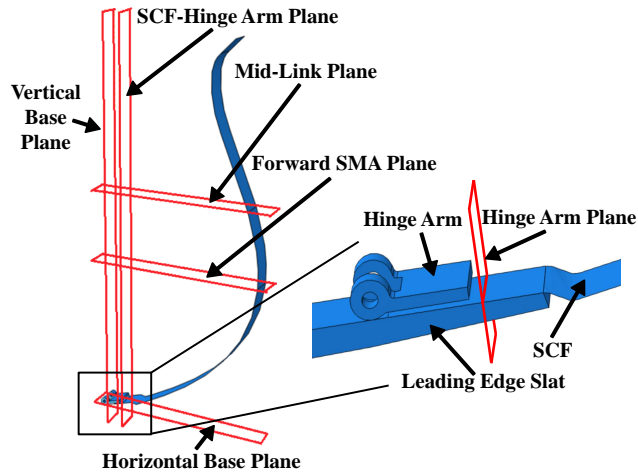
Figure 2.5: Sectioning of SCF into SMA, mid-link, and hinge regions via partition planes.

nearly zero (0.254 cm), which approximated the absence of a mid-link. 172 general shell elements (type S4 [32]) were evenly distributed chord-wise along the total SCF (see Fig. 2.6).[2] A "2.5-dimensional" model was created by utilizing only one element in the width (span-wise) direction and specifying symmetry conditions along both edges of the SCF. This "2.5-dimensional" approach was chosen in order to develop a model consistent with the bench-top prototype, allowing for eventual comparisons between the physical and computational models. In addition, a "2.5-dimensional" model allowed for the estimation of actuation force for a longer (more realistic) SCF using only a small segment of it. The mid-link and hinge arm sections of the SCF were assigned thicknesses and material properties compatible with their experimental counterparts and were much stiffer than the SMA sections (i.e., deformations were taken to be negligible). Positioning and movement of the partition planes, shown in Fig. 2.5, gave rise to the reference dimensions shown in Fig. 2.7 that will be

---

[2]Mesh convergence studies were conducted on initial versions of the FEA model, but not on the current iteration. The element size was based on the minimum size of the mid-link section (approximately 0.6% of the total SCF curvilinear length).

used later in this document. The dimensions denote the length of the SCF-hinge arm (L_h), the length of the forward SMA flexure (L_{fwd}), the length of the mid-link (L_{ML}) and the two SMA flexure thicknesses (t_{fwd} and t_{aft}). The aft SMA flexure length (L_{aft}) is dependent on the other lengths because the overall SCF length is fixed. Note that these length dimensions are linear in the vertical direction from the horizontal base plane and not contour lengths along the respective components.
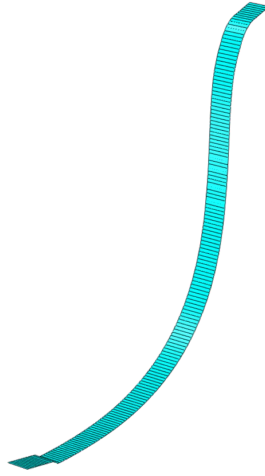
Figure 2.6: FEA mesh of the SCF, the only deformable part in the model.

An Abaqus surface-to-surface contact formulation was utilized to model the contact between the SCF and the main wing or slat. A simple linear penetration law was used to reduce the runtime of the analysis and avoid excessively long optimization processes. The linear contact stiffness was selected to be sufficiently high so as to prevent unreasonable surface penetrations. Contact between the SCF and the main wing or slat was considered to be frictionless in the tangential direction.
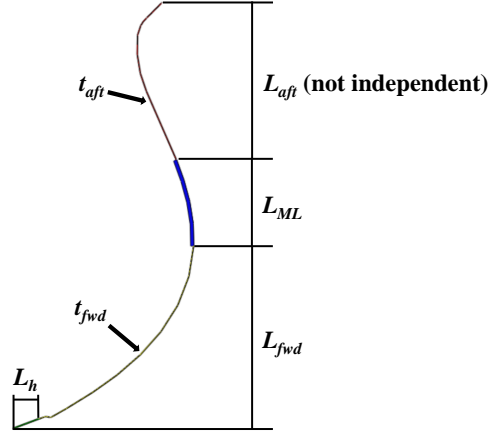
Figure 2.7: Illustration of SCF design variables considered during the optimization.

2.1.5   Load Cases

To perform accurate FEA of the SCF, meaningful loads were needed. In this study, the SCF response to a representative aerodynamic load and to retraction and deployment processes were assumed to be decoupled and were thus assessed separately.

2.1.5.1   Aerodynamic Load Case

The elastic SCF response to a representative aerodynamic load was analyzed using quasi-static mechanical analysis (*Static step in Abaqus).[3] Aerodynamic loading was considered only in the fully-deployed configuration and the rigid slat was held stationary during the analysis. Other aerodynamic loadings due to slat and SCF positions or flight conditions were not considered because there was no available data. The distributed aerodynamic load was obtained from a wind tunnel test of a relevant aircraft model at typical landing conditions and was applied to

---

[3]The aerodynamic load case required approximately 1 minute of computational time using a standard workstation laptop and 1 CPU.

the FEA model as a normal pressure through the use of X,Y,Z point data. The pressure was assumed to be constant in the spanwise (Z) direction. Figure 2.8 shows the pressure distribution plotted along the SCF, where it can be seen that positive pressure presides over the leading portion of the SCF and is replaced by suction in the aft section.
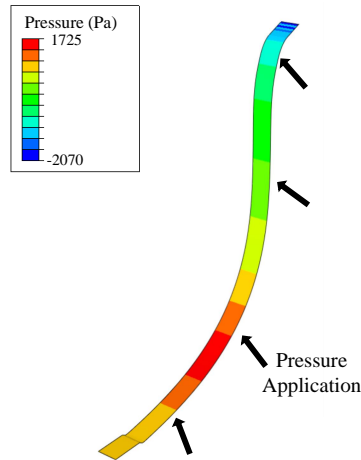
Figure 2.8: Distribution of aerodynamic pressure load plotted along the SCF (Note that positive pressure is pushing while negative pressure is suction).

2.1.5.2   Retract/Deploy Load Case

Aerodynamic loads were neglected for simulation and analysis of the retract/deploy case. The retract/deploy load case required movement of the slat and resulted in unstable dynamic motion of the SCF. Thus, the implicit dynamic solver was used (*Dynamic Implicit step in Abaqus).[4] The quasi-static application was employed to improve computational speed at the expense of not resolving transient behavior accurately.

---

[4]Depending on the SCF configuration, the retraction and deployment load case required approximately 20-40 minutes of computational time using a standard workstation laptop and 2 CPU.

The slat was retracted and deployed through specification of a prescribed z-axis rotation about the slat reference point, as shown in Fig. 2.9. The hinge arm was constrained to move with the slat via a multi-point constraint that was defined between the slat reference point and the hinge axis. A rotation of 0.57 rad (32.7°) was required to move the slat-SCF assembly between the fully-retracted and fully-deployed configurations. The hinge was able to freely rotate about its own local axis during retraction and deployment of the slat through the use of a connector element.
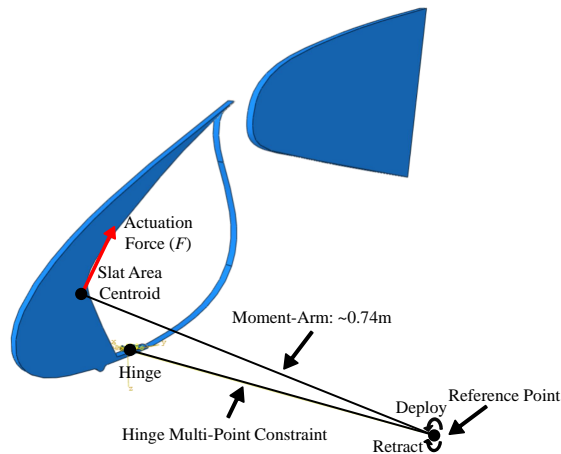
Figure 2.9: Schematic of model for retraction and deployment analysis.

Figure 2.10 shows an example FEA analysis for SCF retraction and deployment corresponding to a monolithic (no mid-link) design. Lengths of the hinge, forward flexure and mid-link were 1.52 cm (the minimum possible), 5.08 cm and 0.254 cm (the minimum possible), respectively, and the thickness of the forward and aft flexures were equal at 0.089 cm for this design. In general, the maximum SMA stress occurred near frame (**3**) in Fig. 2.10 and was largest between the hinge and the SCF/main wing contact point for this case. At such locations, the SMA flexure

locally deformed into the martensite phase, providing the compliance necessary for reconfiguration. In poor design configurations, the SMA became "pinched" at critical locations, causing the stress to greatly increase. These effects were considered in the constrained optimization process to follow.
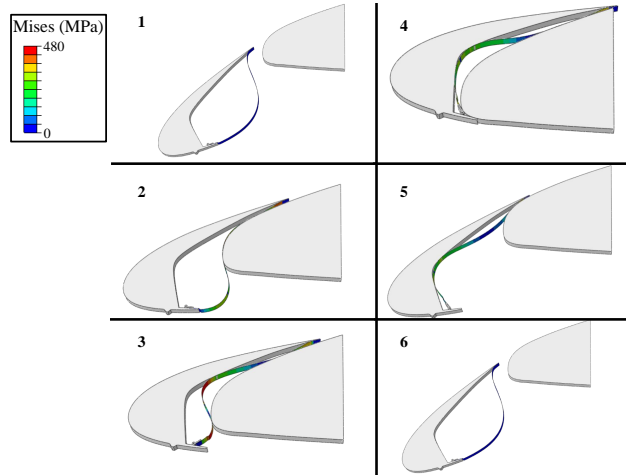
Figure 2.10: Example FEA of retraction and deployment for a nominally monolithic SCF design: L_h=1.52 cm, L_{fwd}=5.08 cm, L_{ML}=0.254 cm, t_{fwd}=0.089 cm, t_{aft}=0.089 cm.

2.2 Design Optimization Problem

The overall goal of the analysis-driven optimization described in this work was to minimize the peak actuation force F_{max} that was needed to retract the slat-SCF assembly. In the FEA model, the actuation force was calculated by dividing the reaction moment on the reference point about which the slat pivots by the distance between the slat area centroid and its reference point (see Fig. 2.9). A smaller actuation force would require less power (for a known retraction time) and was naturally correlated with a lighter weight actuation system, making the SMA-based SCF more

viable for implementation. Special considerations regarding the calculation of F_{max}, especially the complexities of dynamic response, are described in the Appendix A.

The constraints for this optimization were that i) the SCF must self-deploy upon slat deployment, ii) the maximum Mises stress anywhere in the SMA flexures during retraction (σ_{max}^{SMA}) must be less than 690 MPa, and iii) the maximum deflection (U_{max}) anywhere in the SCF must be less than 0.254 cm under the previously described aerodynamic load. By requiring the SCF to self-deploy, the complexity and weight of the system was reduced significantly. SCF self-deployment was determined by tracking the rotation of the hinge, θ_{hinge}. If $\theta_{hinge} < 0.1$ rad after slat deployment, as measured relative to the fully-deployed configuration, then the SCF was known to have successfully self-deployed [39]. While the SMA flexures were relatively compliant when undergoing the stress-induced transformation during retraction, excessive localized stresses occurring *after* completion of transformation could lead to plastic deformation, resulting in permanent modification of the SCF shape, potential failure to self-deploy, and likely acceleration of fatigue. Finally, when the slat was deployed during landing and takeoff, the SCF experienced aerodynamic loads. It was estimated that resulting localized displacements larger than 0.254 cm would lead to losses in lift or reduced aeroacoustic effectiveness.

In summary, the design variables considered in this work were (see Fig. 2.7): the length of the forward SMA flexure (L_{fwd}), the length of the mid-link (L_{ML}), the length of the SCF-hinge arm (L_h), and the two SMA flexure thicknesses (t_{fwd} and t_{aft}). The aft SMA flexure length is not a design variable because it is dependent on the lengths of the other two SCF components.

The design optimization problem is summarized as follows:

<div style="border:1px solid black; padding:1em;">

SCF Design Optimization Problem

Minimize:

The maximum actuation
force needed to retract
the slat-SCF assembly (F_{max})

by varying
design variables:

SCF-hinge Arm Length (L_h)
Forward flexure Length (L_{fwd})
Mid-link Length (L_{ML})
Flexure Thicknesses (t_{fwd}, t_{aft})

subject to constraint
on *outputs:*

$U_{max} \leq 0.254\,\text{cm}$
$\sigma_{max}^{SMA} \leq 690\,\text{MPa}$
$\theta_{hinge} \leq 0.1\,\text{rad}$

</div>

2.3 Towards Optimization: Understanding the Influence of Design Variables

The overarching goal of this study was a comprehensive understanding of the design trade-offs involved in selecting a SCF configuration. Therefore in a manner similar to the experimental studies in previous work [29], the analysis-driven design efforts were started by performing a thorough design of experiment (DOE) to establish trends between design variables (inputs) and SCF structural responses (outputs). In following a path first employed in a previous preliminary study [39], the aerodynamic load analysis and the retract-deploy analysis were conducted in separate DOE studies. Only the most significant results are reported herein due to the large amount of information obtained from this DOE study.

The bounds for the DOE studies are shown in Table 2.2. The chosen ranges for the design variables were considered to be physically reasonable given the overall physical design of the wing, the slat, and its cove while also being large enough to consider wide design variations. The lower limit of L_h corresponded to the length of the hinge arm for the baseline part. The lower limit of L_{fwd} was chosen so that its corresponding partition plane would not cross the SCF-hinge arm partition plane, avoiding unreasonably small forward flexures. The lower limit of L_{ML} (0.254 cm) corresponded to an approximation of a monolithic design (mid-link eliminated).[5] The upper limits of both the forward SMA flexure and the mid-link lengths were chosen such that the aft SMA flexure would not be eliminated. The lower limit for both SMA flexure thicknesses was chosen based on results from previous work [39], which showed that flexures with a thickness of less than 0.0508 cm were infeasible due to insufficient stiffness under aerodynamic loading (i.e., $U_{max} \leq 0.254$ cm consistently exceeded). The upper limit of the flexure thickness was a design constraint that prevented the flexures from penetrating the slat when it is in the fully retracted configuration.

2.3.1   Aerodynamic Load DOE

The first DOE study assessed how the aerodynamic load affected the SCF when in the deployed (reference) configuration. Because the complexities of retraction (contact, dynamics, snap-through, etc.) were not encountered, static elastic analysis was sufficient and this phase of design investigation was highly computationally efficient. Using the ModelCenter Design of Experiment [33] feature and a three-level full factorial array (three equally spaced values based on ranges in Table t:Parameters),

---

[5]The lower limit is not 0 cm because that would remove the mid-link section from the FEA model and destabilize the model.

Table 2.2: Ranges used in the exploration of the design space for the DOE studies (Aerodynamic and Retract/Deploy).

Design Variable	Range
L_h	1.52-5.08 cm
L_{fwd}	5.08-15.2 cm
L_{ML}	0.254-15.2 cm
t_{aft}	0.0508-0.127 cm
t_{fwd}	0.0508-0.127 cm

$3^5 = 243$ configurations of L_h, L_{fwd}, L_{ML}, t_{fwd}, and t_{aft} were analyzed.[6] The main outputs were U_{max} and σ_{max}^{SMA}. Fig. 2.11 shows a scatter-plot matrix of the results. As seen in this figure, thicker SMA flexures were generally associated with lower deflection and lower stress under aerodynamic loading, as expected and shown in rectangles a), b), c) and d). The nearly-linear relation observed in rectangle e) between maximum deflection and maximum stress was also expected due to the linearity of the response to the static load.

The results from this study reinforced previous work [39]. The factor-effects plot, shown in Fig. 2.12, indicates that the SMA flexure thicknesses (specifically t_{fwd}) had the greatest effect on maximum SCF displacement under static aerodynamic loading, while the length of the hinge arm had little effect. This was consistent with the role of the flexures as the compliant portion of the structure. A more informative illustration of the relation between flexure thicknesses and maximum aerodynamic displacement is shown in Fig. 2.13. The figure shows a general trend of increased stiffness resulting from increased flexure thickness, though strong non-linear effects

---

[6]Note that 17 of the 243 runs failed to converge due to excessive deflection of the SCF associated with poor designs having flexures of insufficient thickness.
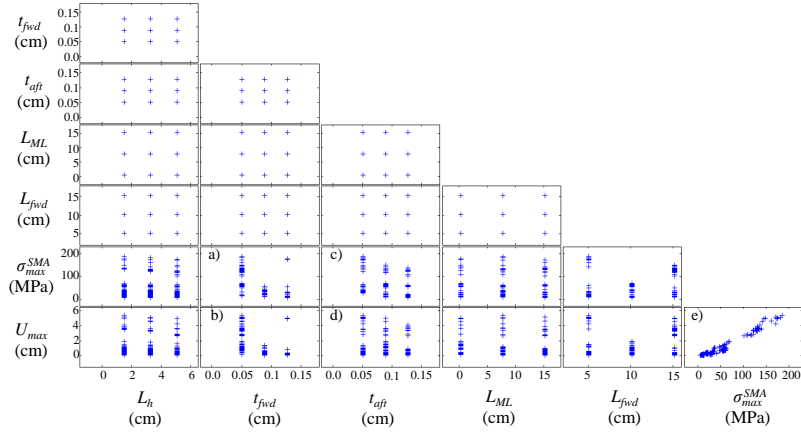
Figure 2.11: Scatter-plot matrix for aerodynamic load DOE.
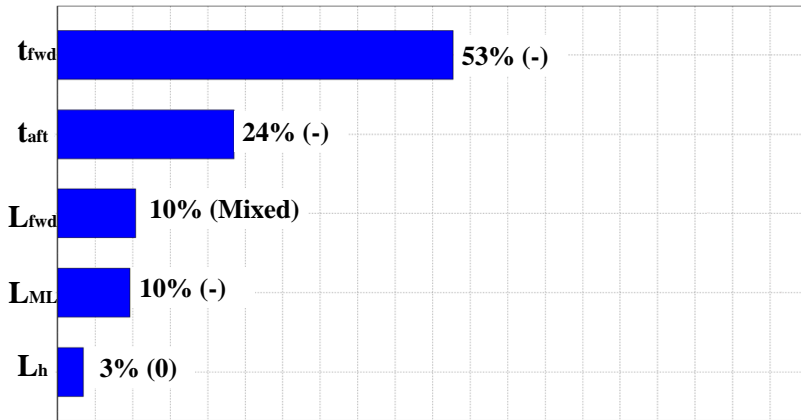
Figure 2.12: Design parameter influence on maximum SCF displacement (U_{max}) under aerodynamic loading.

were observed at lower deflections, especially when one flexure was much stiffer than the other. It was also observed that as the length of the stiff mid-link increased, the maximum displacement decreased as the overall structural stiffness increased. Finally, it was observed that no design configuration exhibited a maximum von Mises stress exceeding 200 MPa, indicating that aeroelastic overstressing need not be considered during design optimization.

39
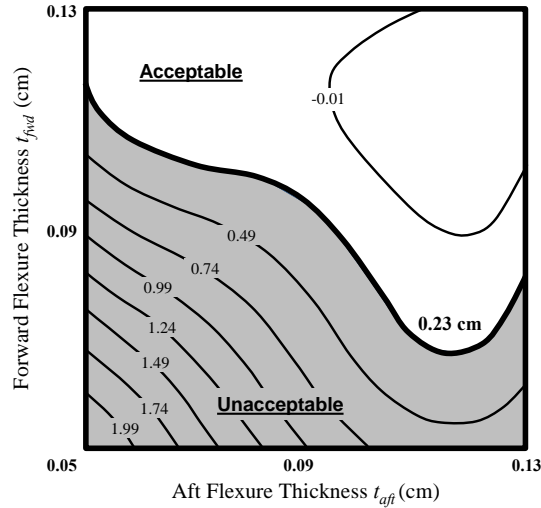
Figure 2.13: Contour plot showing effect of flexure thicknesses on maximum SCF displacement under static aerodynamic loading (L_h=1.52 cm, L_{fwd}=10.2 cm, L_{ML}=8.89 cm).

2.3.2   Retract-Deploy DOE

The second DOE study focusing on the retract-deploy response was similarly performed. Here, all components of the computational analysis framework were used (UMAT, Abaqus, and ModelCenter). Due to the time required to perform a single run, a full-factorial array was not considered feasible. Instead a Design Explorer Orthogonal Array was used in conjunction with the Design of Experiment feature in ModelCenter, such that 125 combinations of L_h, L_{fwd}, L_{ML}, t_{fwd}, and t_{aft} were analyzed.[7] It was observed that approximately half of these runs did not complete due to excessive and non-physical deformations that prevented numerical convergence, such as the SMA flexures being severely "pinched" (i.e., very tightly bent) by the slat or main wing. An example is shown in Fig. 2.14. It was observed

---

[7]Orthogonal arrays uses the minimum number of runs that gives full information regarding design variable influence on the outputs. More layers results in more combinations of the design variables. Five layers were chosen since it was unknown how many designs would fail.

that these failed runs exhibited a combination of flexure thicknesses and mid-link length that also did not satisfy the displacement constraint according to the results of the aerodynamic-load DOE. Thus, the failed runs were considered to be infeasible designs.[8] Figure 2.15 shows a scatter-plot matrix of the data from the retract/deploy DOE. As expected, a larger rigid mid-link typically resulted in an increased maximum retraction force, as observed in rectangle a), and larger SMA thicknesses also typically corresponded to larger F_{max}, as observed in rectangles b) and c). Other key outputs of this analysis included the maximum Mises stress in the SMA flexures and the rotational displacement of the hinge after the slat was deployed.
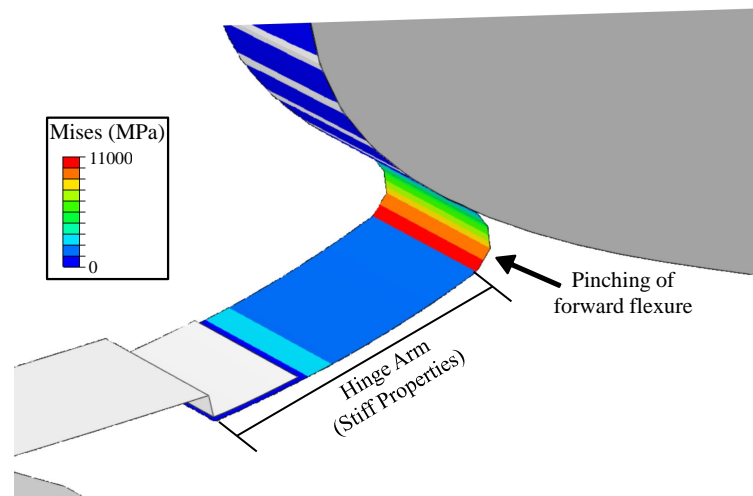
Figure 2.14: "Pinching" of forward SMA flexure due to excessive hinge arm length. Note that deformation curvatures of this magnitude are not physically feasible and thus the mesh refinement is no longer applicable.

Based on the results of this DOE study, the length of the hinge arm had a strong effect on the maximum stress in the SMA flexures due to the propensity of the

---

[8]57 of the 125 designs failed to converge.
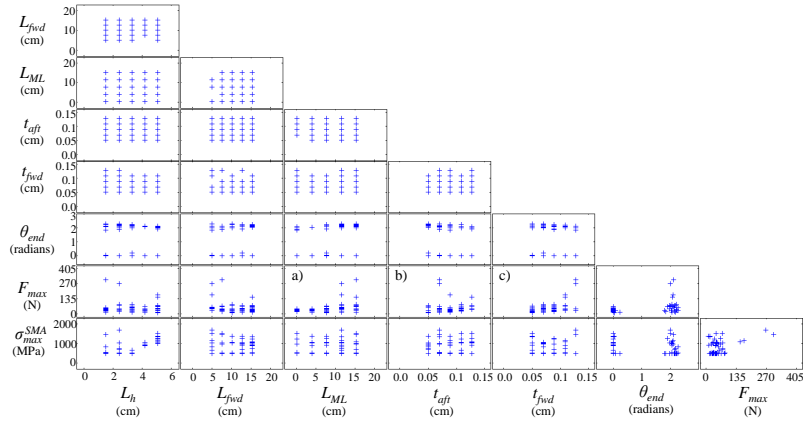
Figure 2.15: Scatter-plot matrix for retract-deploy DOE.

flexure to be "pinched" when poor hinge configurations were considered. As seen in Fig. 2.16, the maximum stress in the SMA flexures increased greatly for SCF-hinge arm lengths greater than 3.3 cm. This result was not intuitively expected, and it was decided that hinges over 4.19 cm in length should not be considered during the optimization phase to follow.[9] A contour plot showing the relation between the maximum retraction force and the flexure thicknesses can be seen in Fig. 2.17. Clearly, the force increased as either of the flexure thicknesses increased, though t_{fwd} had a greater effect since the forward flexure was undergoing the most bending deformation. However, as shown in Fig. 2.13, a design with thin flexures does not satisfy the displacement constraint under static aerodynamic loading. Thus, determination of flexure thickness was identified as a key outcome of the optimization process.

---

[9]The upper value was set to 4.19 cm in order to consider designs that might converge between 3.3 cm and 4.19 cm.

42
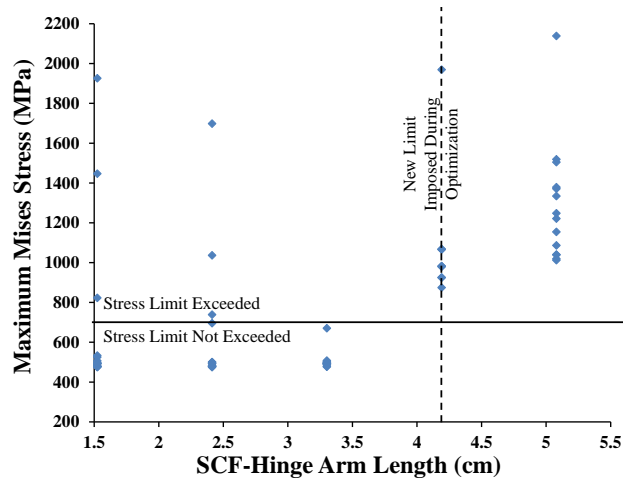
Figure 2.16: Relation between the SCF-hinge length and the maximum Mises stress. Note the increase in stress to unreasonable levels as the hinge length increases due to "pinching" of the SCF (see Fig. 2.14).
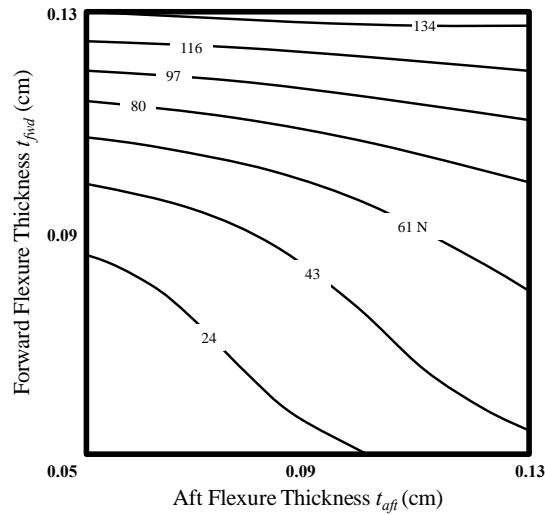
Figure 2.17: Contour plot showing the relation between the maximum actuation force and the flexure thicknesses (L_h=1.52 cm, L_{fwd}=10.2 cm, L_{ML}=8.89 cm).

43

2.4 Constrained Optimization

The results from both DOE studies were used to determine the design variable bounds for the optimization, which are provided in Table 2.3. The only bound that was adjusted from the DOE studies was the length of the SCF-hinge arm, the upper bound of which was changed from 5.08 cm to 4.19 cm because of the "pinching" of the forward flexure (see Fig. 2.14 and Fig. 2.16). The bounds of the flexure thicknesses were unchanged due to their opposing effects on the aeroelastic deflection and the maximum actuation force. The bounds for L_{fwd} or L_{ML} were not adjusted because nearly every combination resulted in a feasible design, depending on other variables.

Table 2.3: Range of design variables used in the optimization.

Design Variable	Range
L_h	1.52-4.19 cm
L_{fwd}	5.08-15.2 cm
L_{ML}	0.254-15.2 cm
t_{aft}	0.0508-0.127 cm
t_{fwd}	0.0508-0.127 cm

The optimal design that minimized actuator force was expected to correspond to thin flexures. This obvious trend was constrained, however, by the need of the SCF to maintain the deployed shape under aerodynamic loading. Due to the opposing effects of flexure thicknesses on aeroelastic deflection and retraction actuation force, both the simple aeroelastic analysis and more intensive retract-deploy analysis needed to be run during the optimization.

44

To perform the optimization, all components of the analysis framework (FEA, UMAT, simulation process control) along with the Design Explorer tool from ModelCenter were employed [10, 33].[10] A flowchart depicting the optimization process is shown in Fig. 2.18. 213 runs were needed to converge on an optimized solution.

Table 2.4 shows the design variables and the model outputs of the optimized design. Figure 2.19 shows the design configuration with a rendered thickness for the optimal design.
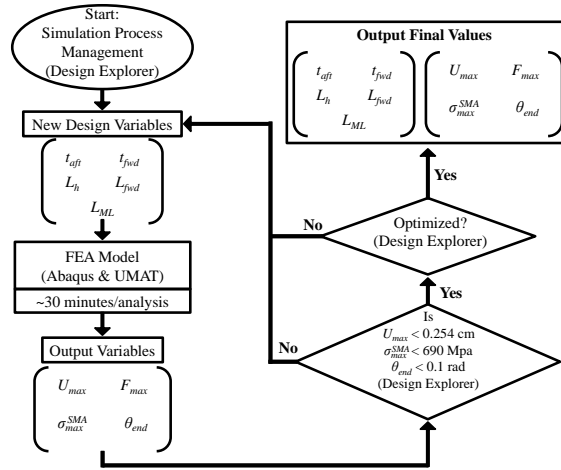
Figure 2.18: Flowchart of the optimization process.

As shown in Table 2.4 for the given constraints, the optimal design solution for the SCF was a short hinge, monolithic SMA configuration with a constant flexure thickness of approximately 0.10 cm. As stated earlier, the physical realization of the

---

[10]The Design Explorer tool invokes a surrogate-based optimization scheme in which Kriging surfaces for the goals and constraints are fit to initial DOE data and then further improved with additional analysis. Mathematical optimization is performed over these surrogate models. Final convergence requires accurate correspondence between the Kriging surfaces and the analysis results in the neighborhood of the optimal design point. In this work, the default settings of the Design Explorer tool were used which included an initial search of 49, a maximum number of functional evaluations of 500, and a convergence tolerance of 10^{-5}.

short hinge, monolithic prototype had a noticeable reduction in the amount of force required to retract the SCF, validating the results of the optimization.

Table 2.4: Optimized design inputs and output parameters.

Design Variable	Optimized Value	Nearest Bound
L_h	1.65 cm	1.52 cm
L_{fwd}	15.2 cm	15.2 cm
L_{ML}	0.254 cm	0.254 cm
t_{fwd}	0.103 cm	0.127 cm
t_{aft}	0.0975 cm	0.127 cm
Output Parameters	Optimized Value	Nearest Constraint
U_{max}	0.253 cm	0.254 cm
σ_{max}^{SMA}	478 MPa	690 MPa
Self-Deploy?	Yes	
F_{max}	22.3 N	
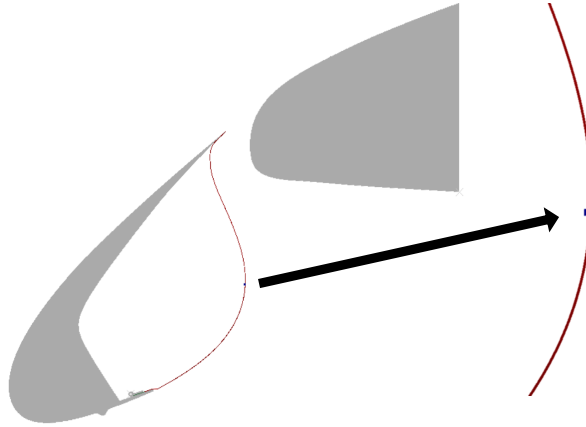
Figure 2.19: Optimized design configuration for SMA-based SCF.

Based on the optimization results, the constraint on the maximum displacement was the active constraint. In order to examine how sensitive the optimal design was to the displacement constraint, the constraint was increased by 10% (new constraint of 0.2794 cm). The forward and aft flexure thickness (design variables with most effect on outputs) were decreased till this new constraint was reached. The resulting design had forward and aft flexure thicknesses of 0.101 cm and 0.0956 cm, respectively (approximately 2% decrease in the thickness for both flexures) with a maximum displacement of 0.278 cm. Under retraction/deployment loading, the design was able to redeploy and had a maximum actuation force of approximately 21.0 N (approximately 6% decrease from optimal design).

3. COMPUTATIONAL FLUID DYNAMICS ANALYSIS AND FLUID-STRUCTURE INTERACTION ANALYSIS OF SCF FOR CRM GEOMETRY

The success of the design optimization of the SCF motivated further work on the SCF concept. Specifically, focus shifted to the development and testing of CFD and FSI models of the SCF in order to gain an understanding of how the SCF behaved in flow.[1] For this portion of the work, a new airfoil system (and thus a new SCF profile) was chosen to align with other efforts related to the SCF. Note that much of the work conducted in this section was done in congruence with the next section on wind tunnel testing of the physical analog to the computational models.

3.1 CRM Model Geometry

The SCF profile considered in this portion of the work was developed for a high-lift version of the CRM. The CRM is an open-geometry, transport-class aircraft developed collaboratively developed by NASA and Boeing for the purpose of CFD analysis validation and testing new technologies [40, 31]. For this portion of the work, the base geometry of the computational and physical models[2] was from a 6.25% scaled 2D section aligned with freestream flow at mid-span of the outboard slat (see Fig. 3.1). This scale was chosen to avoid significant blockage effects in the wind tunnel. At 6.25% scale, the chord of the retracted wing was approximately $0.32\,\text{m}$ ($1\,\text{ft}$). Due to sweep and taper of the wing, the shape of the slat and flap in the 2D section (see Fig. 3.1) are different at each deployment level. To make articulation of the slat and flap possible in both the computational and physical

---

[1]Prior to this shift, design optimization was conducted on a similar SCF profile and further reduction of actuation loads was examined.

[2]See the following section for a detailed description of the physical model

models, the retracted versions of the slat and flap were used.
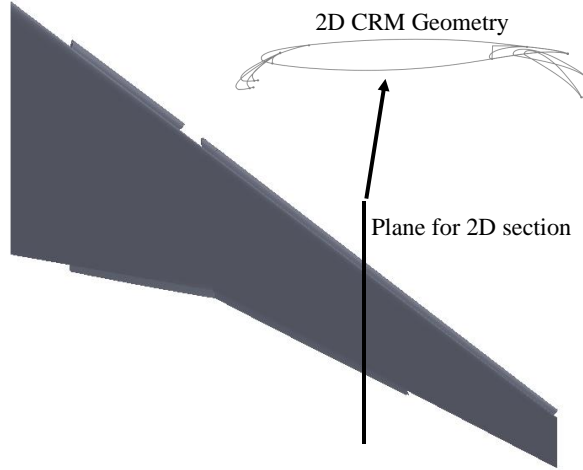
Figure 3.1: Solidworks model of 3D CRM wing configuration used to obtain 2D section. Note that the 2D section shown is not the same scale as the 3D wing.

3.2   Effect of Scaling on Structural Model Load Cases

Section 3.2 will serve as a transition between the previous section and the current section by discussing how scaling the SCF geometry effects the aerodynamic loading and retraction/deployment load cases. For this discussion, a scale factor λ_x is introduced which relates a physical quantity x at full scale to the same physical quantity at a smaller scale by the following equation,

$$\lambda_x = \frac{x_{SmallScale}}{x_{FullScale}} \tag{3.1}$$

The scaling presented in this work utilizes static aeroelastic scaling theory that is extensively described elsewhere[41]. General aeroelastic similitude requires that a scale model have the same Reynolds number, Mach number, shape, ratio between stiffness of the structure and aerodynamic forces, mass ratio, reduced frequency and

Froude number. Depending on the wind tunnel used for small scale tests, meeting all of these requirements may not be possible. The scaling theory assumes that effects due to change in mass ratio, Reynolds number and Froude number can be neglected for static aeroelastic scaling. Applying these assumptions to the relation between force and deflection results in the following equation,

$$\lambda_{EI} = \lambda_{\bar{q}}\lambda_L^4 \tag{3.2}$$

where λ_{EI}, $\lambda_{\bar{q}}$ and λ_L are the stiffness, dynamic pressure and size scale factors, respectively. Static aeroelastic scaling requires that this equation be maintained. Also, this equation implies that the scale factor for displacement due to loading λ_d is equal to the size scale factor.

We will now apply the scaling to the load cases of the SCF. Since we are only interested in the landing and approach phases of flight (generally low altitude), we can assume that the wind tunnel model and full scale vehicle are at the same atmospheric conditions changing Eq. 3.2 to the following,

$$\lambda_{EI} = \lambda_M^2\lambda_L^4 \tag{3.3}$$

where λ_M is the scale factor for the Mach number. For the case where the mach number for the wind tunnel model and full scale vehicle is equal and assuming the same material properties for the SCF, Eq. 3.3 (and thus $\lambda_d = \lambda_L$) can be maintained by scaling the entire structure by λ_L. This is shown in Fig. 3.2(a). At full scale ($\lambda_L = 1$) the displacement of a sample SCF configuration is on the order of $0.1\,\mathrm{cm}$ while at 10% scale ($\lambda_L = 0.1$) the displacement is on the order of $0.01\,\mathrm{cm}$ (10% of the displacement at full scale). In addition, the distribution of the displacement is the same. As a result of Mach number being equal and using the same material

50

properties for both full scale and small scale, the actuation force is scaled by a factor (λ_F) that is equal to (λ_L^2). As shown in Fig. 3.2(b), at full scale the actuation force is on the order of $10\,\text{N}$ while at 10% scale the actuation force is on the order of $0.1\dot{\text{N}}$ (1% of the force at full scale).

(a) Displacement due to aerodynamic loading.

(b) Actuation force versus retraction.
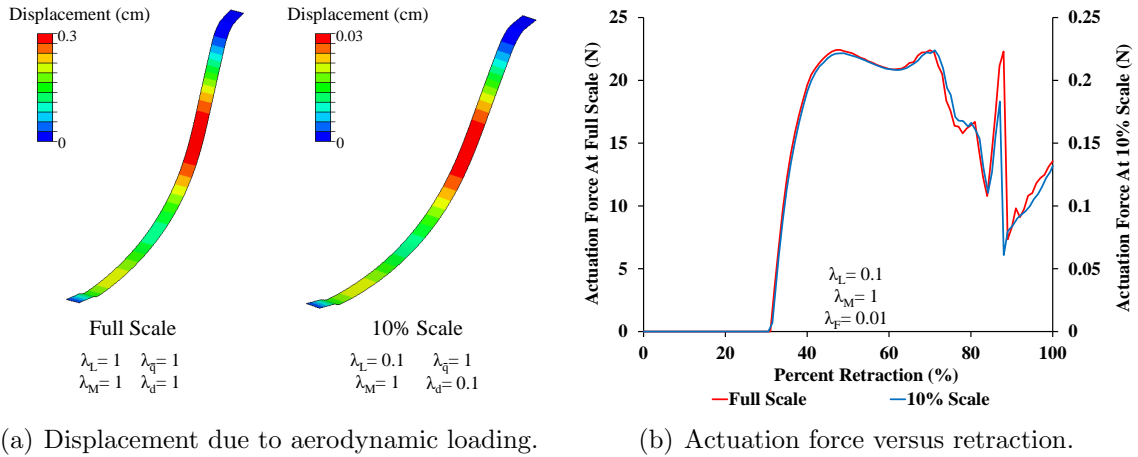
Figure 3.2: Effect of scaling when Mach number is the same between full scale and small scale.

For the case where the Mach number of the wind tunnel model is not the same as the Mach number at full scale, assuming that the pressure distribution on the SCF will scale in the same manner as the dynamic pressure $(\lambda_{\bar{q}} = \lambda_M^2)$, Eq. 3.3 can be maintained by adjusting the structural stiffness of the SCF.[3] Ideally, the same material is used between full scale and wind tunnel scale $(\lambda_E = 1)$, so only inertia can be changed. The scale factor for the inertia λ_I is equal to λ_L^4. Since the SCF is a thin shell in flow, the thickness can be changed to adjust the inertia. Scaling the thickness of the SCF (λ_t) separately from its overall size scaling results in the scale

---

[3]Note that a case of different Mach numbers is not presented in the work from which the scaling theory is obtained. This case is simply further manipulation of the relation between applied force and displacement.

factor for inertia being equal to $\lambda_t^3 \lambda_L$. Substituting this relation between the scale factors for inertia (and thus stiffness), thickness and size into Eq. 3.3 and solving for scale factor of the thickness results in the following equation,

$$\lambda_t = \lambda_M^{2/3} \lambda_L. \tag{3.4}$$

This equation solves for the scale factor of thickness that is required to maintain Eq. 3.3. Figure 3.3(a) shows the SCF displacement 10% scale for two cases with scale factors of the Mach number. With the proper scaling of the pressure distribution and SCF thickness, the displacement for both cases is the same as the displacement for the SCF when the Mach number matched (see Fig. 3.2(a)). Since the thickness of the SCF is changed to maintain Eq. 3.3, the scale factor for the actuation force is now calculated as follows:

$$\lambda_F = \lambda_M^2 \lambda_L^2. \tag{3.5}$$

For example, a 10% scale model of the SCF with a Mach number scale factor of 0.5 has a scale factor for the thickness of 0.063 resulting in a scale factor of 0.0025 for the actuation force. This is shown in Fig. 3.3(b), where the actuation force of the 10% scale model is 0.25% of the full scale version.

As previously stated, the geometry for both computational and physical models in the current work is scaled by 6.25% from the full scale wing ($\lambda_l = 0.0625$). During landing and approach for full scale the CRM wing, the Mach number is 0.2. Current physical tests and computational analysis are conducted with a free stream velocity of $15\,\mathrm{m/s}$ which corresponds to a Mach number of 0.044 ($\lambda_M = 0.22$). Based on the size and Mach number scale factors, the scale factor for the thickness should be 0.0238. However, design optimization has not been conducted for the SCF from the

(a) Displacement due to aerodynamic loading.

(b) Actuation force versus retraction.
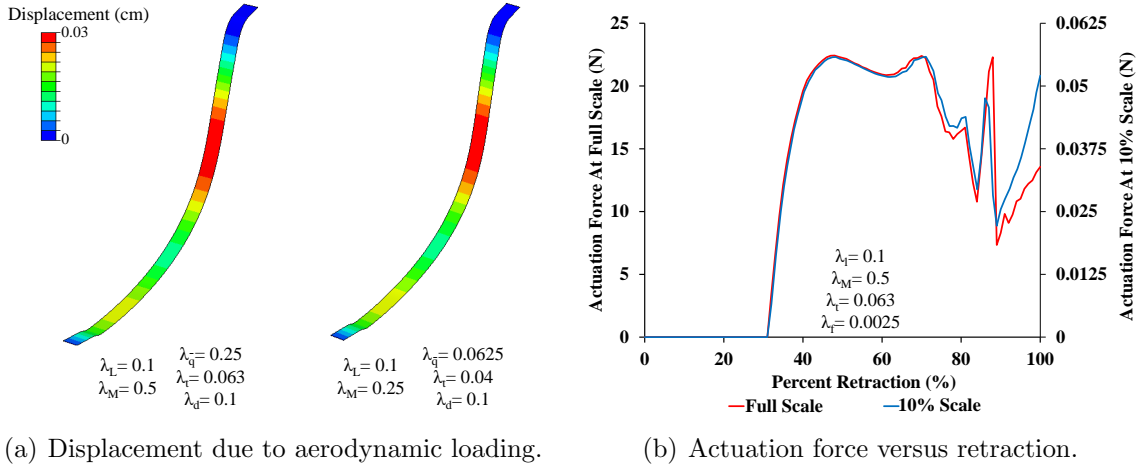
Figure 3.3: Effect of scaling when Mach number is not the same between full scale and small scale.

full scale CRM geometry. Based on the thickness of the optimal design of the SCF from the previous section (which was a 75% scale geometry), the thickness of the scaled SCF should be 0.03 mm (0.0012 in). Since the SCF geometry and pressure distribution being used for CFD/FSI and wind tunnel tests are different from the design optimization, this thickness is only used as an initial estimate.

3.3   CFD Model Development and Analysis

Before conducting FSI analysis on the SCF, CFD models of the SCF needed to be constructed. These models and their results would serve as a basis for the FSI models. CFD analysis was conducted using the thermo-fluid solver known as SC/Tetra [42]. This CFD suite utilized density and pressure based finite volume methods and unstructured meshing to solve both turbulent and laminar flows. Also, SC/Tetra made use of overset meshes[4] that can be incorporated in slat articulation and is connected to Abaqus with a built-in link, making FSI analysis easier to perform.

---

[4]A detailed description of overset meshes follows in the FSI portion of this section.

3.3.1 Turbulence Model Description

In Section 3.3.1, a general description of turbulence modeling, specifically the Shear-Stress Transport (SST) k-ω, is provided. More detailed descriptions of the SST k-ω can be found elsewhere [42, 43].

For laminar, incompressible flow (single species), fluid solvers such as SC/Tetra solve the conservation of mass, conservation of momentum and conservation of energy equations. For this problem, the change in temperature is not of interest so temperature is held constant. This simplifies the conservation equations and removes the need to solve the conservation of energy.

The conservation of mass is given as,

$$\frac{\partial u_i}{\partial x_i} = 0 \tag{3.6}$$

where x_i is the ith coordinate (i= 1 3 for a 3-dimensional system) and u_i is the velocity in the x_i direction. The conservation of momentum equation is,

$$\frac{\partial \rho u_i}{\partial t} + \frac{\partial u_j \rho u_i}{\partial x_j} = -\frac{\partial P}{\partial x_i} + \frac{\partial}{\partial x_j} \mu \left(\frac{\partial u_i}{\partial x_j} + \frac{\partial u_j}{\partial x_i} \right) \tag{3.7}$$

where ρ is the density (constant for incompressible fluid), t is time, p is the fluid pressure and μ is the viscosity.

Unlike the smooth, steady movement of laminar flow, turbulent flow is the unsteady movement of fluid. Turbulent flow can develop from laminar flow when the Reynolds number exceeds a critical value. A key characteristic of turbulent flow is the development of eddies (circular motion of flow) which increases the mixing of fluid. Eddies of various length scales are formed and need to be resolved to solve the turbulent flow. Capturing all of the eddies in turbulent flow is impossible due

to computer limitations. Instead, the change in mean velocity (or heat transfer) due to turbulence is obtained. For this reason instantaneous pressure and velocity are expressed as a summation of the mean values (detonated as $\overline{P}$ and $\overline{u_i}$) and the fluctuation (detonated as P' and u_i').

$$u_i = \overline{u_i} + u_i{}' \tag{3.8}$$

$$P = \overline{P} + P' \tag{3.9}$$

Substituting these values into conservation of mass and conservation of momentum results in the following, equations

$$\frac{\partial \overline{u_i}}{\partial x_i} = 0 \tag{3.10}$$

$$\frac{\partial \rho \overline{u_i}}{\partial t} + \frac{\partial \overline{u_j} \rho \overline{u_i}}{\partial x_j} = -\frac{\partial \overline{P}}{\partial x_i} + \mu \frac{\partial}{\partial x_j} \left(\frac{\partial \overline{u_i}}{\partial x_j} + \frac{\partial \overline{u_j}}{\partial x_i} \right) - \frac{\partial}{\partial x_j} \left(\rho \overline{u_i' u_j'} \right) \tag{3.11}$$

Equation 3.11 is known as the Reynolds equation. The term $-\rho \overline{u_i' u_j'}$ is known as the Reynolds shear stress and represents the shear stress produced by turbulent flow. This term cannot be solved practically without making some assumptions. Joesph Boussinesq proposed treating the Reynolds stress as the following

$$-\rho \overline{u_i' u_j'} = \mu_t \left(\frac{\partial \overline{u_i}}{\partial x_j} + \frac{\partial \overline{u_j}}{\partial x_i} \right) - \frac{2}{3} \rho k \delta_{ij} \tag{3.12}$$

where μ_t is a proportionality constant known as the eddy viscosity and k is the turbulent energy expressed as,

$$k = \frac{1}{2}\overline{u_i'u_i'} \tag{3.13}$$

The only remaining information to specify in Eq. 3.12 is the eddy viscosity μ_t. However, since the eddy viscosity changes with location and state it needs to be constantly redefined. This is accounted for by introducing fundamental quantities of turbulence and solving the transport equations related to the quantities.

The k-ω turbulence model proposed by Wilcox [44], uses the turbulent energy k and the dissipation rate per unit of turbulence energy ω. The dissipation rate per unit turbulent energy ω is proportional to ε/k where ε is the dissipation rate. In this model, eddy viscosity is expressed as,

$$\mu_t \mid_{k-\omega} = \rho\frac{k}{\omega} \tag{3.14}$$

The transport equations for k and ω are expressed as:

$$\frac{\partial \rho k}{\partial t} + \frac{\partial \overline{u_i}\rho k}{\partial x_i} = \frac{\partial}{\partial x_i}\left[\left(\mu + \frac{\mu_t}{\sigma_k}\right)\frac{\partial k}{\partial x_i}\right] + G_s - \rho\varepsilon \tag{3.15}$$

$$\frac{\partial \rho\omega}{\partial t} + \frac{\partial \overline{u_j}\rho\omega}{\partial x_i} = \frac{\partial}{\partial x_j}\left[\left(\mu + \frac{\mu_t}{\sigma_\omega}\right)\frac{\partial \omega}{\partial x_j}\right] + \frac{\gamma\rho}{\mu_t} + G_s - \beta\rho\omega^2 \tag{3.16}$$

$$G_s = \mu_t\left(\frac{\partial \overline{u_i}}{\partial x_j} + \frac{\partial \overline{u_j}}{\partial x_i}\right)\frac{\partial \overline{u_i}}{\partial x_j} \tag{3.17}$$

where $\varepsilon = C_\mu\, k\, \omega$. Note that C_μ, σ_k, σ_ω, β and γ are all model constants.

The model constant γ is calculated from the other constants by the following equation.

$$\gamma = \frac{\beta}{C_\mu} - \frac{\kappa^2}{\sigma_\omega \sqrt{C_\mu}} \tag{3.18}$$

where κ is another model constant. Note that the k-ω model can be analytically equivalent to the k-ε model (another popular turbulence model [42]) with the addition of the cross-diffusion term to the right side of the ω transport equation as follows,

$$CD_{k\omega} = 2\frac{\rho}{\sigma_\omega \omega}\frac{\partial k}{\partial x_j}\frac{\partial \omega}{\partial x_j} \tag{3.19}$$

In near-wall flow, the k-ω model has advantages over other turbulence models. It better estimates the boundary layer separation in flow with adverse pressure-gradients, and damping functions are not required for calculating the near-wall velocity. The k-ω model, however, is very dependent on boundary conditions such as the free stream turbulence properties. Also, in the outer free-steam layer of a boundary layer, the k-ω model loses accuracy. For these reasons, we consider a variation of the standard k-ω model known as the SST k-ω. This model, developed by Menter [43] uses a zonal treatment to avoid the numerical errors associated with the k-ω model in the outer boundary layer region. In the near-wall regions, the standard k-ω equations are used, while towards the outer regions, the equations are adjusted to match the behavior of k-ε turbulence models that are more accurate in the outer region. The shift in model behavior is performed using a product of the cross-diffusion term shown in Eq. 3.19 and a blending function that is dependent on the wall distance and turbulence quantities. In addition, the blending function is used to interpolate the model constants from given values for both the inner and outer regions.

The eddy viscosity for this model is represented by the following equation,

$$\mu_t \mid_{SST} = \rho \frac{a_1 k}{\Omega} \tag{3.20}$$

where a_1 is a constant (=0.31) and Ω is the magnitude of mean vorticity. Both Eq. 3.14 and Eq. 3.20 are interpolated using a blending function with arguments of wall distance and turbulence quantities.

3.3.2   Fluid Models

Both the tunnel and the scaled wing were modeled in the CFD software (shown in Fig. 3.4). In addition, there were three variants of the fluid CRM wing model (shown in Fig. 3.5): 1) retracted, 2) deployed, and 3) deployed with SMA SCF. The overall fluid model was based on the dimensions of the Texas A&M University 3 ft-by-4 ft tunnel (test section was 2.74 m in length), which was used for physical wind tunnel testing. The physical model spanned the entire width of the tunnel so a 2.5D (one element in spanwise, Z, direction) model was used for the analysis, reducing the computation time. The length of the models in the spanwise direction was set to 1.27 cm (0.5 in). The CFD model was broken into three closed volumes (aside from the solid parts): 1) outer, 2) middle, 3) inner. The inner region was based on a 10% chord offset from the wing. The middle region was a 1-chord by 2-chord box centered about the retracted mid-chord of the wing. The outer region was the remainder of the fluid domain. Each region was assigned an individual element size such that computational runtime was reduced while accuracy of flow results near the wing was maintained. Note that the mesh near the tunnel floor and ceiling in the outer region was refined to match the size of the inner mesh to accurately capture wall effects from the tunnel.

Mesh studies were performed on the deployed-with-SCF configuration to deter-
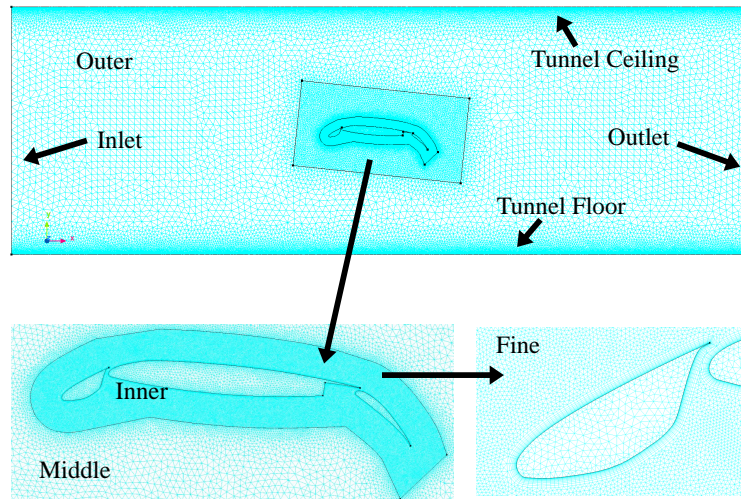
Figure 3.4: CFD model for Boeing-NASA CRM airfoil with mesh shown.
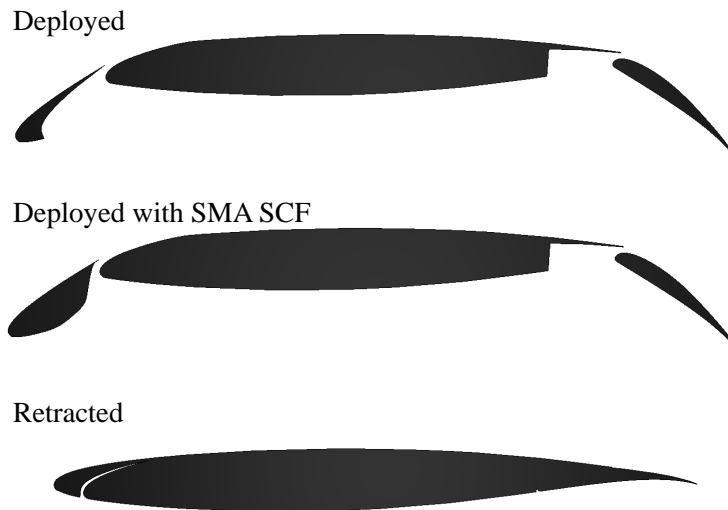
Figure 3.5: CRM CFD model variants.

mine the element sizes ($2.56\,\mathrm{cm}$, $0.64\,\mathrm{cm}$ and $0.08\,\mathrm{cm}$ for the outer, middle and inner regions, respectively) that would not significantly change the lift and drag of the wing with further refinement of the mesh (see Appendix A). Note that the solid wing sec-

tions were not heavily meshed as they do not impact the CFD analysis. Prism layers were inserted along the surface of the wing and tunnel ceiling/floor to capture the boundary layer. The thickness of the first layer, change of thickness between layers, and total number of layers were chosen based on a prism layer study using the deployed-with-SCF configuration that also evaluated changes in lift and drag (see Appendix A). It was assumed that the element and prism layer sizes would be sufficient for the deployed (no SCF) and retracted configurations. The deployed and deployed-with-SCF had approximately 200,000 elements (130,000 Prism and 70,000 Hexahedron) while the retracted configurations had approximately 187,000 elements (119,000 Prism and 68,000 Hexahedron). The origin of the model was placed at the mid-chord of the retracted configuration at an angle of attack of -1.48°, which was the orientation of the original CRM geometry and wind tunnel model. Different angles of attack were considered by rotating the medium, fine and wing closed volumes about the rotation point of the wing ((x=-44.45 mm, y=0 mm) from the physical model).

Three boundary conditions were placed on the CFD model: 1) the wing surface and tunnel floor/ceiling had a smooth no-slip wall condition, 2) the static pressure at the outlet was zero, and 3) the freestream velocity at the inlet was prescribed. Incompressible air (viscosity of 1.83×10^{-5} Pa-s and density of 1.206 kg/m^3), was used as the fluid. The turbulence properties (k, ε) at the inlet of the test section were unknown so two cases were considered: 1) inlet flow was almost laminar or 2) inlet flow had fully developed turbulence. For the first case, k and ε were set to default values (k=0.0001 m^2/s^2, ε=0.0001 m^2/s^3).

For fully developed turbulence at the inlet, k and ε are calculated using the follow equations

$$k = \frac{u^2}{100} \tag{3.21}$$

$$\varepsilon = \frac{0.09^{\frac{3}{4}} * k^{\frac{3}{2}}}{0.07D} \tag{3.22}$$

where D is the equivalent diameter of the test section (currently taken as the height of the tunnel $0.91\,\mathrm{m}$). At $15\,\mathrm{m/s}$, k and ε are $2.25\,\mathrm{m^2/s^2}$ and $8.66\,\mathrm{m^2/s^3}$, respectively.

3.3.3 CFD Results

Computational runtime for FSI analysis was significant. Therefore, an accurate model needed to be used. CFD analysis provided baseline results that could be compared to wind tunnel data, other fluid solvers and FSI results, giving confidence to researchers regarding the computational tools. For this purpose, CFD analysis was conducted for all three configurations mentioned earlier at angles of attack from -2° to 12° with an inlet velocity of $15\,\mathrm{m/s}$. Each CFD analysis was run until the solution appeared to be steady. Of particular interest were results between 4° and 8° angles of attack since that was the range of angles for approach and landing phases of flight for this wing.

Pressure and viscous forces acting on the surface of the wing in the vertical (Y) and horizontal (X) directions were extracted for each configuration and normalized by the retracted chord, span of the fluid model and dynamic pressure to obtain the lift (C_l) and drag (C_d) coefficients. Figure 3.6 shows the lift-AoA curves of the retracted and deployed configurations for both laminar inlet flow (denoted as Laminar Inlet) and turbulent inlet flow (denoted as Turbulent Inlet). As shown the zero lift-angle of

61

attack (AoA) of the retracted configuration for both inlet cases was slightly less than -2°. Between -2° and 6° for both inlet cases, the lift-AoA curves of the retracted configuration were approximately linear and had similar values. After 6° the two lift-AoA curves diverge due to the differences in inlet turbulence. For the laminar inlet flow case, the lift-AoA curve started to flatten as the angle of attack reached 8°, possibly indicating the configuration was near maximum lift. At 10° and 12° angle of attack, the lift coefficient decreased signaling that the configuration was stalling. For the turbulent inlet flow case, the lift-AoA curve remained linear till 8° but started to flatten between angles of attack of 8° and 12°, possibly indicating the configuration was approaching maximum lift. Unlike the laminar inlet flow case, at 12° with turbulent inlet flow the retracted configuration had not stalled indicating that the inlet turbulence was allowing flow to stay attached to the wing for higher angles of attack.
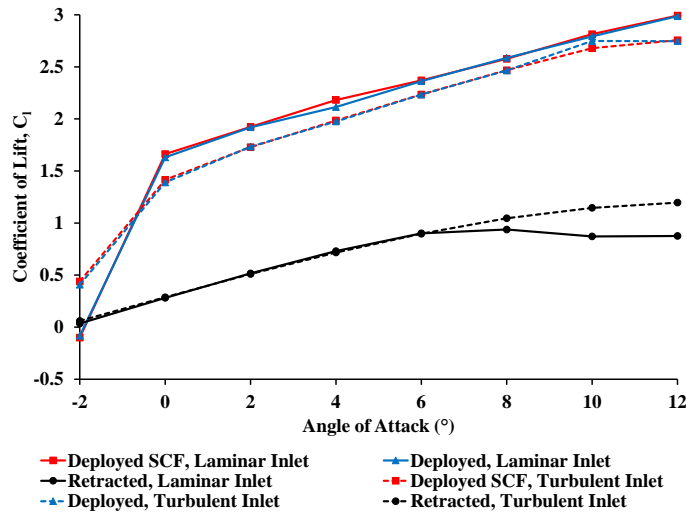
Figure 3.6: Lift-AoA curve for CRM configurations.

With the exception of an angle of attack of -2° with laminar inlet flow, all deployed cases exhibited a significant increase in the lift coefficient as compared to the retracted configuration. In addition for each inlet case, the lift coefficient between the two deployed configurations was approximately equal, showing that the SCF did not negatively affect the lift. For both inlet cases, the lift-AoA curve of the deployed configurations was near-linear between 0° and 10°. Under laminar inlet flow, the curve continued to be linear while under turbulent inlet flow, the lift-AoA curve flattened indicating that both deployed configurations were near maximum lift. Stall had not occurred for either deployed configuration at the maximum considered angle of attack of 12°, but given the flatness of the turbulent inlet flow lift-AoA curve, both configurations were near stall. Also, for both inlet cases, there was a significant decrease in lift below 0° since the slat started to cause separation that extended the entire length of the lower surface of the main wing, negatively impacting the lift characteristics of the wing. The main difference between the two inlet cases, was that the deployed configurations under laminar inlet flow generally had higher lift as compared to the turbulent inlet flow case, indicating that there was a loss of lift due to turbulence at the inlet.

Drag polars for the three configurations are shown in Fig. 3.7. For both inlet cases of the retracted configuration at low angles of attack, the lift coefficient significantly increased with small increases in the drag coefficient. As the wing approached higher angles of attack, the drag polar began to curve resulting in significant increases in drag for small increases in lift. For the laminar inlet flow case, maximum lift was achieved and the configuration began to stall, further increases in AoA led to increases in drag and decreases in lift due to flow separation.once the For the turbulent inlet flow case, maximum lift and stall had not occurred at 12° angle of attack since there was still an increase in lift. However, the significant increase in

drag for small increases in lift indicated that the configuration was near maximum lift. In general, having fully developed turbulence at the inlet results in higher drag at the same value of lift. Also, the drag polar had a smoother curve for turbulent inlet flow, while the drag polar for laminar inlet flow was almost vertical at low angles of attack, followed by a sharp turn as as the configuration began to stall.
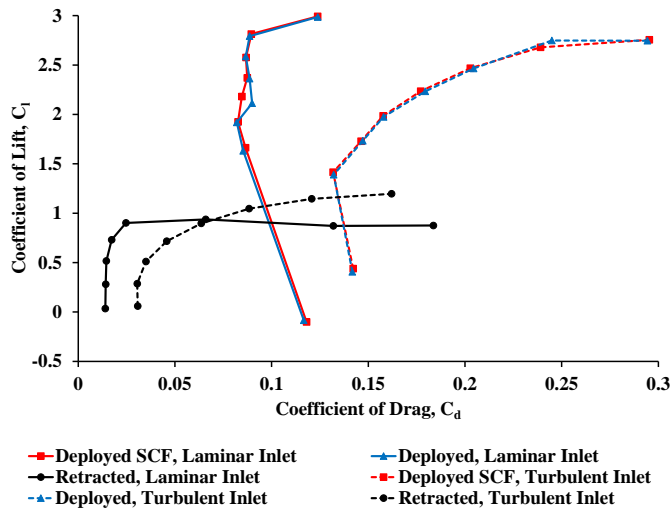
Figure 3.7: Drag Polar for CRM configurations.

For both inlet cases of the deployed configurations, the entire drag polar was shifted in the positive direction for both the lift and drag coefficients. In addition, for both inlet cases, the deployed configurations had similar values of lift and drag, indicating that the SCF did not negatively impact the wing. As with the retracted configuration, turbulent inlet flow increased the drag and created a smoother polar as compared to laminar inlet flow. For the laminar inlet flow case, the lift coefficient increased with little change in drag between angles of attack of 0° and 10°while for the turbulent inlet flow case with the same range of angles, the lift coefficient increased

with larger increases in drag. In addition for turbulent inlet flow, as the angle of attack increased, the change in lift decreased while the change in drag increased. At higher angles of attack for both inlet cases, there was significant increase in drag for small increases in lift, indicating that both deployed configurations were nearing stall. At -2° for both inlet cases, the lift significantly decreased while the drag increased since there was separation on the lower surface of the main wing.

The pressure coefficient distribution around the surface of the retracted configuration at multiple angles of attack for turbulent inlet flow can be seen in Fig. 3.8. [5] The x=0 mm location corresponds to the x coordinate of the retracted chord at mid-chord at -1.48° angle of attack (origin of CFD model). At lower angles of attack (Fig. 3.8(a) and Fig. 3.8(b)), the difference in the pressure coefficient between the lower and upper surfaces was small (with the exception of the leading and trailing edges), which led to the low lift coefficient values seen in Fig. 3.6. As the angle increased (Fig. 3.8(c) - Fig. 3.8(f)), the difference in pressure coefficient between the surfaces increased and the suction peak grew resulting in increased lift. Nearing the maximum lift (Fig. 3.8(f)), the change in pressure coefficient with respect to the angle of attack decreased.

Pressure distributions for the retracted configuration were also created using a panel-method code known as Javafoil in order to serve as a comparison with CFD results. The retracted geometry in Javafoil was a smooth airfoil variant with no gaps between the different components. Figure 3.9 shows the coefficient of pressure distributions from CFD and panel method analysis for two angles of attack in the range of interest. Panel method generated a similar distribution as CFD analysis. However, panel method had a higher suction peak at the leading edge and a larger

---

[5]The distributions for both inlet cases were approximately the same between -2° and 6°. Above 6°, the turbulent inlet case had higher pressure at the suction peak as compared to the laminar inlet case since the wing was stalling at high angles of attack under laminar inlet flow.
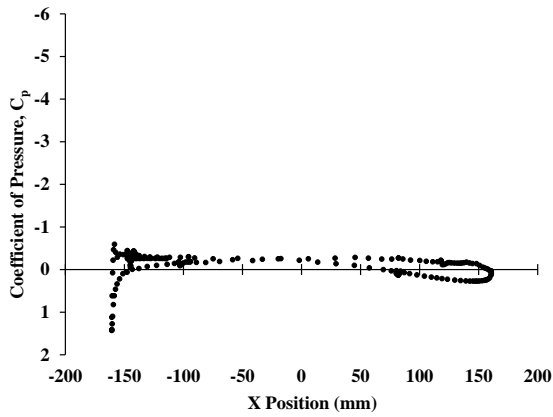
(a) -2° Angle of Attack.
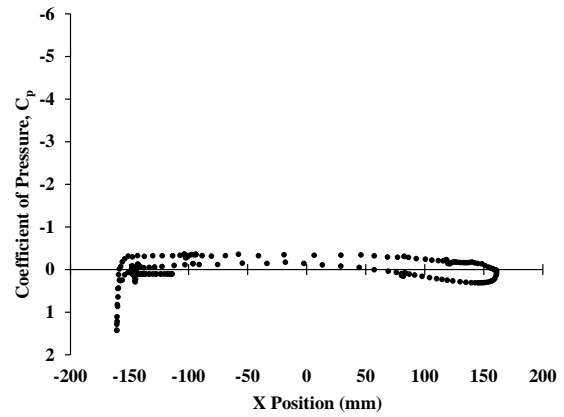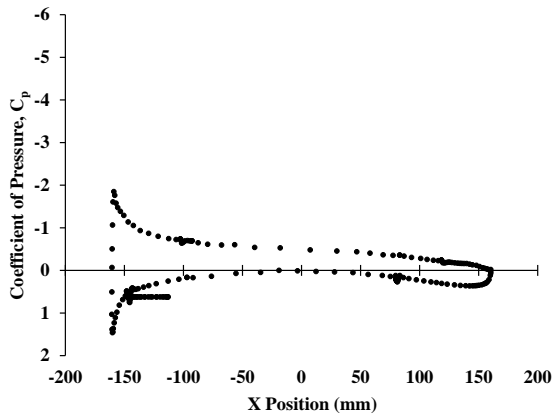
(b) 0° Angle of Attack.
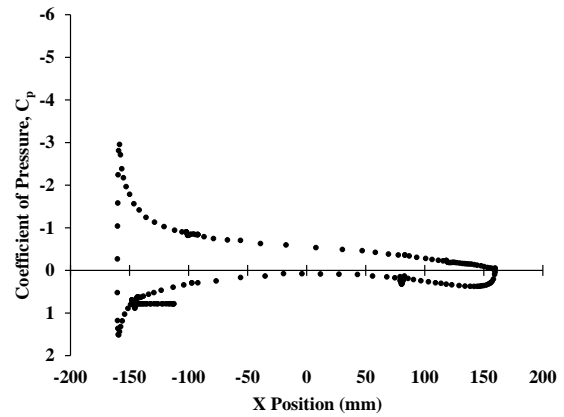
(c) 4° Angle of Attack.
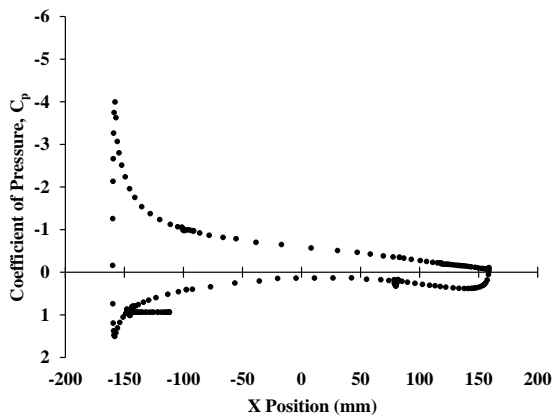
(d) 6° Angle of Attack.

(e) 8° Angle of Attack.

(f) 12° Angle of Attack.

Figure 3.8: Coefficient of pressure distribution for the retracted configuration.

distributions on the upper and lower surfaces of the wing.

(a) 4° Angle of Attack.

(b) 8° Angle of Attack.
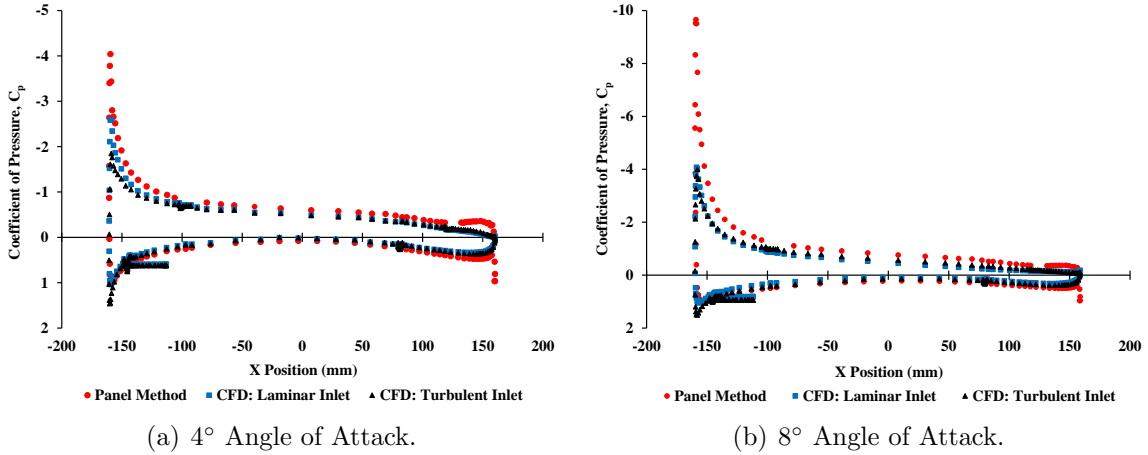
Figure 3.9: Comparison of coefficient of pressure distributions for the retracted configuration from CFD and panel method analysis.

Figure 3.10 shows the pressure coefficient distribution for both deployed configurations. [6] With the exception of 0° angle of attack, the pressure coefficient distribution was nearly identical for both deployed configurations. This result was understandable since the lift coefficients were also approximately equal. The difference in the 0° angle of attack configuration may be due to partial flow separation inside the slat cove. The main difference between the two deployed cases at higher angles of attack (Fig. 3.10(c) - Fig. 3.10(f)) was along the lower surface of the slat. A difference on the lower surface of the slat was understandable since the SCF modifies the shape of the lower surface. However, it should be noted that the difference in the pressure coefficient distribution between these two configuration was small so an

---

[6]The pressure distribution for the deployed configurations under laminar inlet flow generally had more developed suction peaks on the slat and main wing than as compared to turbulent inlet flow. This was understandable since the laminar inlet flow case predicted higher lift.

initial estimate of the pressure distribution along the SCF could be obtained from the distribution along the lower surface of the slat without the SCF.

At an angle of attack of -2° (Fig 3.10(a)), the difference in pressure coefficient distribution along both surfaces of the main wing and flap was small resulting in low lift. Most of upper surface of the slat had positive pressure while the lower surface had negative pressure. This was indicative of the flow separating along the lower surface of the wing (specifically at the leading edge of the slat) which accounted for the low value of lift at this angle. Increasing the angle of attack to 0° (Fig. 3.10(b)) resulted in the disappearance of flow separation along the lower surface, significantly changing the pressure coefficient distribution. Suction peaks for the main wing and flap were more developed and there was significant difference in pressure coefficient distribution between the upper and lower surfaces. Further increase in angle (Fig. 3.10(c) - Fig. 3.10(f)) resulted in growth of the slat suction peak as the slat became more effective. The rise in angle also increased the difference in pressure coefficient between the upper and lower surfaces of the main wing (which also corresponds to increased lift). Most of the change in pressure coefficient distribution was along the upper surfaces of the slat and main wing while the distribution along the flap surfaces changed the least.

Velocity profiles for the retracted configuration at various angles of attack for the turbulent inlet flow case are shown in Fig. 3.11. As expected, at low angles of attack, the flow remained attached for most of the wing. Increasing the angle resulted in an increased velocity at the leading edge as well as growth of the separation zone near the trailing edge. At 12° AoA, the flow was separating midway along the upper surface of the wing indicating that maximum lift was near or at 12°, which matched observations from the lift and pressure results. Further increases in angl would result in separation across the entire upper surface indicating that the wind had stalled.
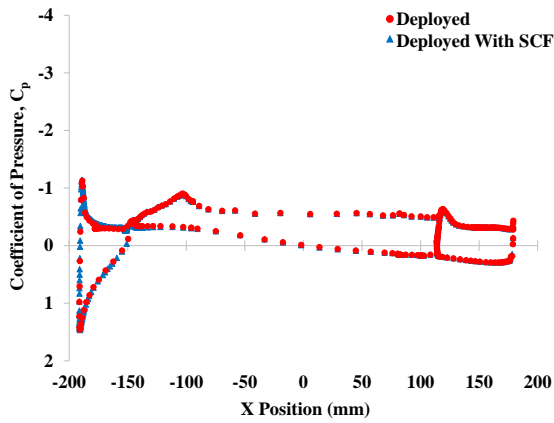
(a) -2° Angle of Attack.
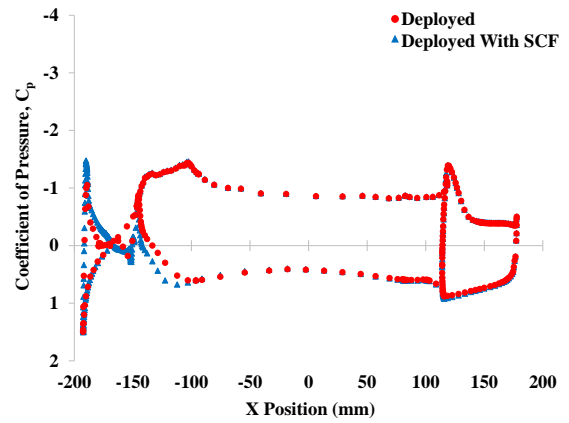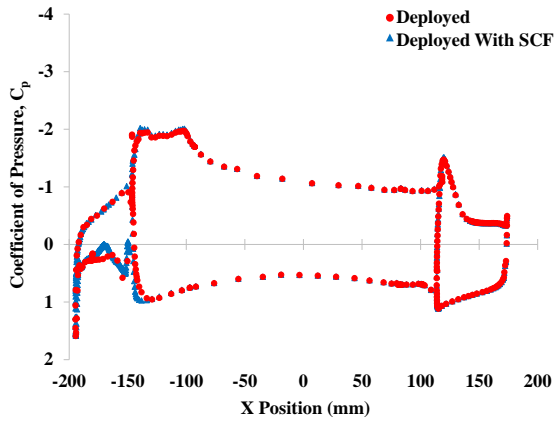
(b) 0° Angle of Attack.

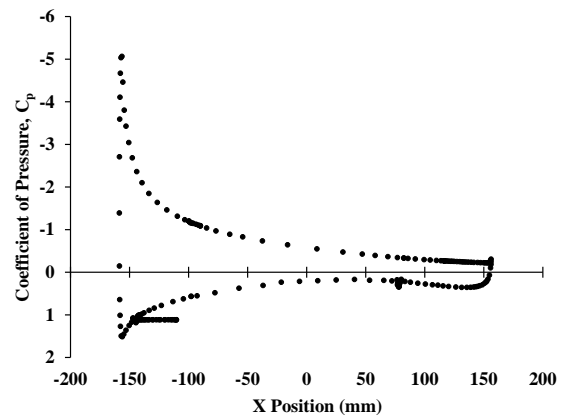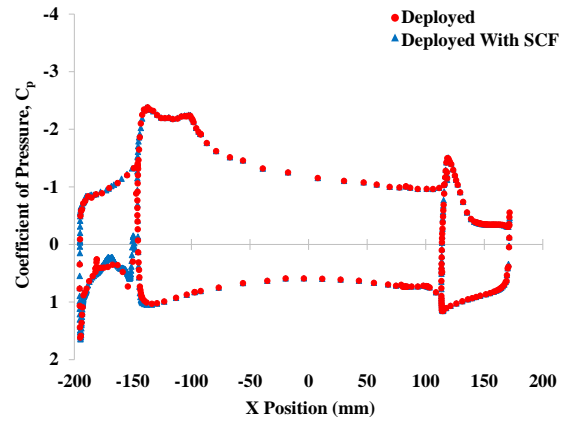(c) 4° Angle of Attack.
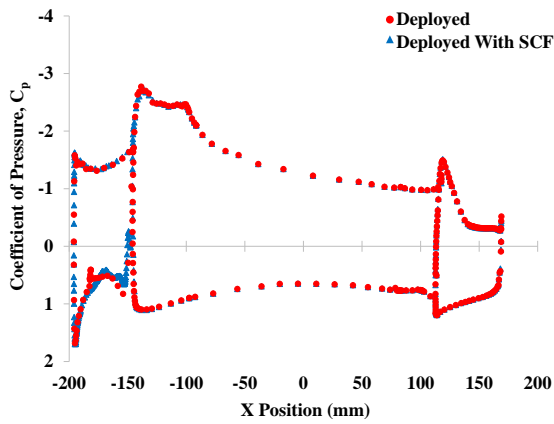
(d) 6° Angle of Attack.
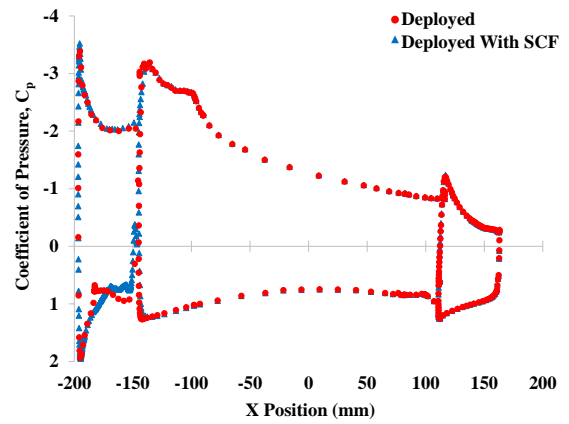
(e) 8° Angle of Attack.

(f) 12° Angle of Attack.

Figure 3.10: Coefficient of pressure distribution for the deployed configurations.

69
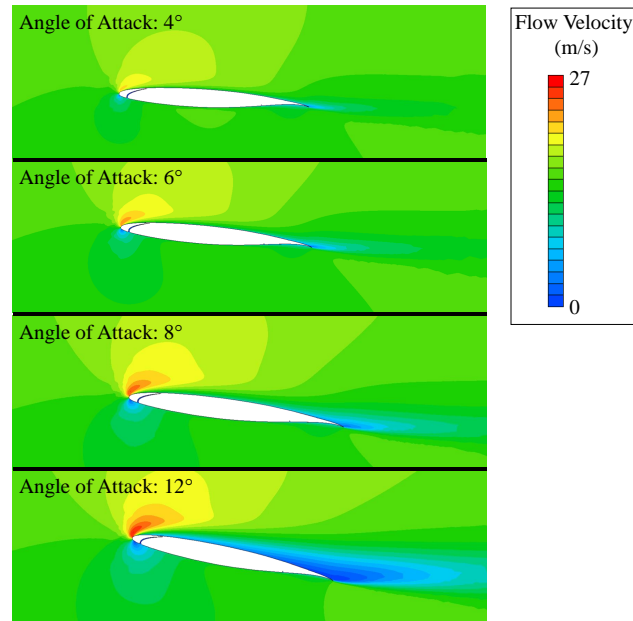
Figure 3.11: Velocity contours for retracted CRM configuration.

Figure 3.12 shows the velocity contours for both deployed configurations with turbulent inlet flow.As shown in Fig. 3.12, the velocity contours for both deployed configurations were similar at all angles of attack. At -2°, the flow separated over the entire lower surface of the wing and flap, resulting in significant decreases in lift. At higher angles of attack, where the slat was effective, the flow remained attached over most of the wing but separated along the upper surface of the flap. Also, the flow was energized at the leading edge of the main wing due to the slat. Similar to the retracted configuration, increased angle of attack led to an increase in the velocity at the leading edge of the main wing. Figure 3.12 also showed the effect of the SCF. At angles with an effective slat, the SCF removed the circulation in the cove of slat without significantly changing the velocity contour of the overall flow.
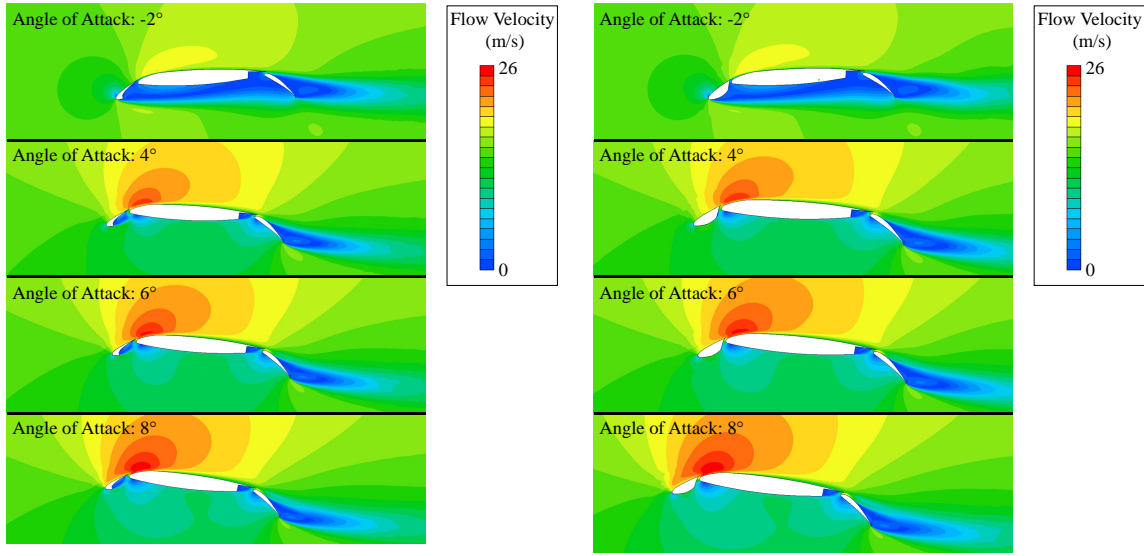
(a) Deployed Configuration.

(b) Deployed with SCF configuration.

Figure 3.12: Velocity contours for deployed CRM configurations.

3.4 FSI Model Development and Analysis

With the completion of CFD analysis for the CRM model, focus shifted to FSI analysis of the SMA SCF in flow. Details are given regarding the changes made to the fluid model required for FSI analysis and how the fluid and structural models were linked. In addition, analysis of model response to various load cases is presented.

3.4.1 FSI Structural Model

The structural FEA model of the scaled SMA SCF (shown in Fig. 3.13(a)) for FSI analysis was created in a similar manner as that described in Section 2.1.4. The spanwise (Z) length of all parts in the model was $10.27\,\mathrm{mm}$ ($0.5\,\mathrm{in}$). The slat, hinge and main wing were modeled as rigid bodies. The slat in the structural model was modified from the original CRM slat to accommodate the retracted SCF (see Fig. 3.14). The hinge was relatively simplistic. For FSI analysis, both its length

71

and position were chosen based on decisions made during the manufacturing process (see the next section for more details). The hinge axis was placed against the cove wall and the hinge arm was set to 8 mm long. Unlike the work described in the previous section, only a monolithic SMA SCF was considered due to the size of the SCF (approximately 5 cm in length). Structural optimization was not conducted for this SCF due to practical fabrication constraints at this scale such as custom SMA thickness and connecting the hinge to the slat and SCF. For FSI analysis, the SCF was set to 0.0762 mm (0.003 in) to match the physical model (see the next section for more details).[7] Similar to the previous structural model, 265 general four node shell elements (type S4) [32] were distributed evenly along the profile of the SCF while it had one element in width in the spanwise direction (shown in Fig. 3.13(b)). In addition, symmetry conditions were used on both SMA SCF edges in the X-Y plane to implement one element in the width making the model essentially infinitely long in span ("2.5-dimensional"). This maintained the accuracy of the results while reducing computational runtime significantly.

Contact between the SCF and the main wing or slat was modeled using the Abaqus surface-to-surface contact with the linear penetration law in the normal direction and a coefficient of friction of 0.42 in the tangential direction. The coefficient of friction was determined experimentally from friction tests with SMA and 3D printer plastic.

This structural model was built to be run with or without FSI analysis. Like the previous model, two load cases could be separately assessed without using FSI analysis: 1) static aerodynamic loading and 2) quasi-static retraction/deployment.

Aerodynamic loading of the SCF was analyzed using static analysis (`*Static`

---

[7]A thickness of 0.0762 mm corresponded to 1.22 mm (0.048 in) at full scale if the wind tunnel and full scale Mach numbers were the same or to 3.35 mm (0.131 in) at full scale for 15 m/s flow in the wind tunnel.

(a) Overall assembly.   (b) SCF Mesh.
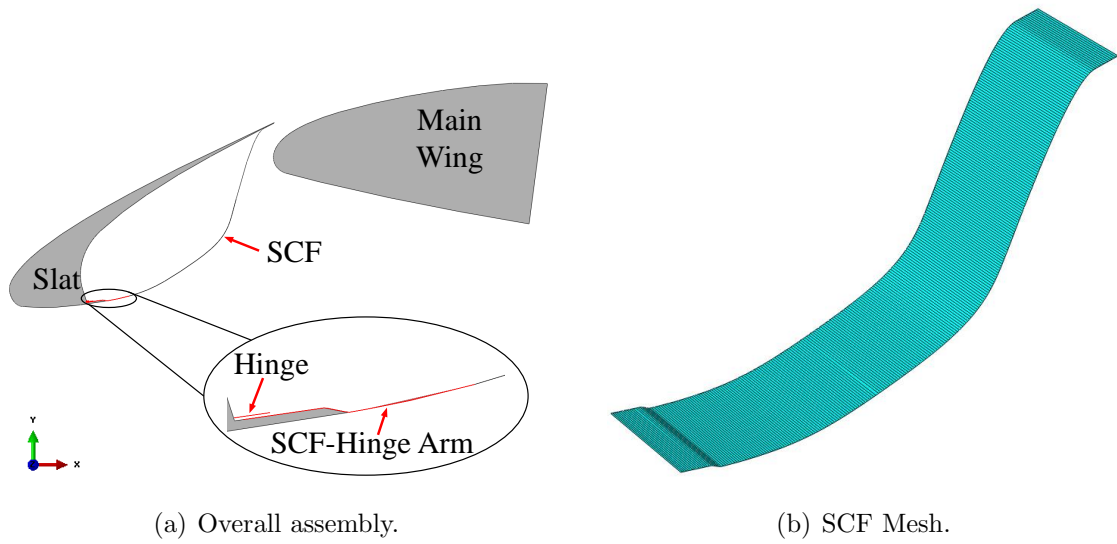
Figure 3.13: Structural FEA model of 2.5D SMA SCF assembly.
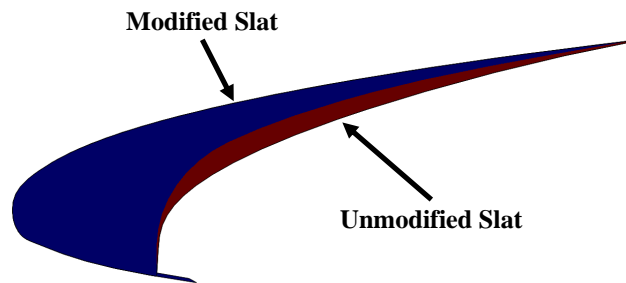
Figure 3.14: Overlay of original slat (red) and modified slat for FSI analysis (blue).

step in Abaqus). This analysis was only considered in the fully deployed SCF config-
uration. Other SCF configurations and dynamic loading were considered during FSI
analysis. The static aerodynamic loading was considered to be a uniform pressure
distribution in the spanwise direction and was implemented using X, Y, Z point data

from preliminary CFD analysis (see Fig. 3.15). The hinge was allowed to freely rotate in this load case through the use of a connector element
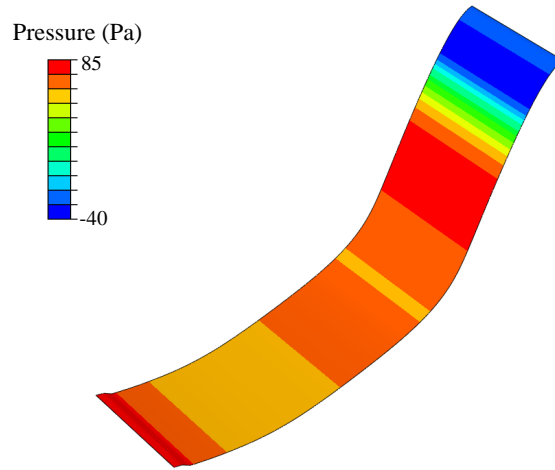
Figure 3.15: Pressure distribution on SCF from preliminary CFD.

An implicit dynamic solver (*Dynamic Implicit step in Abaqus) with a quasistatic implementation was used to analyze slat retraction/deployment since the motion of the SCF could be unstable. During this analysis, aerodynamic loading was neglected when FSI analysis was not conducted. The retraction/deployment of the slat was controlled by applying a rotation to the slat reference point. Full retraction occurred at 0.44 rad of rotation. A multi-point constraint between the slat reference point and rotation axis of the hinge was used to maintain the relation between the slat and hinge. In this analysis, the hinge was able to freely rotate.

The material properties used for this portion of the work are shown in Table 3.1. To obtain the material properties, tensions tests were performed at different temperatures on dogbone specimens (per ASTM standard [45]) cut from the same SMA material used in the physical wind tunnel model. The specimens (one heat-treated

like the physical SMA SCF and one untreated[8]) were loaded until the specimens fully transformed into the martensite phase, and then unloaded (see Fig. 3.16).

Table 3.1: SMA material properties for scaled models.

Property	Value
(Elastic Properties)	
E_A, E_M	44.2 GPa, 26.4 GPa
$\nu_A = \nu_M$	0.33
(Phase Diagram Properties)	
M_s, M_f	236.9 K, 236.5 K
A_s, A_f	266.6 K, 268.1 K
$C^A = C^M$	7.1 MPa/K, 7.7 MPa/K
(Transformation Strain Properties)	
$H = H_v$	5.15%
(Smooth Hardening Properties)	
n_1, n_2, n_3, n_4	0.5
(Other Properties)	
ρ	6480 kg/m^3
$\alpha_M = \alpha_A$	0

The hysteresis loops from the tension tests were used to calibrate the UMAT, which was then validated by superimposing the calibrated model onto the experimental results. Figure 3.17 shows the calibrated model for the treated SMA material superimposed unto experimental results at 25°C. As seen the figure, the hysteresis loops matched fairly well. Figure 3.18 shows the hysteresis loops for the treated and

[8]Shape setting of the SCF will be discussed in the next section.
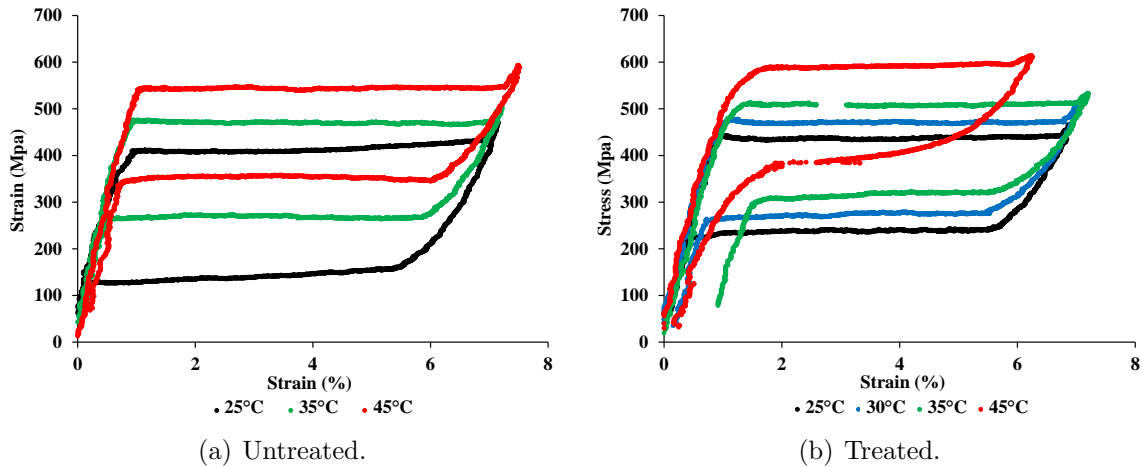
Figure 3.16: Experimental stress-strain data for untreated and heat-treated SMA specimens.

untreated specimens as well as the loop from the original material data used in the previous section at 25°C. The hysteresis loop for the heat-treated SMA exhibited similar stiffness in the austenite phase and similar forward transformation stresses to the untreated material. This showed that the heat treatment would not adversely effect the material response for low loadings such as the aerodynamic load case. The most significant difference between the untreated and treated hysteresis loops is the reverse transformation stresses. Reverse transformation occurs at a higher stress for the treated material resulting in a smaller hysteresis loop. Compared to the original material response, both the treated and untreated material responses achieve more transformation strain at lower stresses.

Linear perturbation analysis was conducted on the structural model in order to obtain the natural frequency of the structure. From the analysis it was found that the SCF had a natural frequency of 285 Hz.
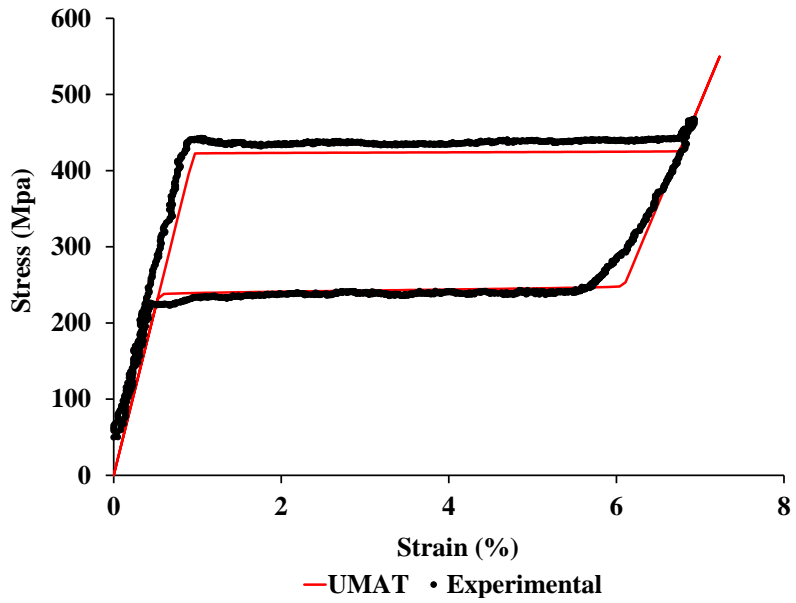
Figure 3.17: Calibrated UMAT hysteresis loop superimposed onto experimental data at 25°C.
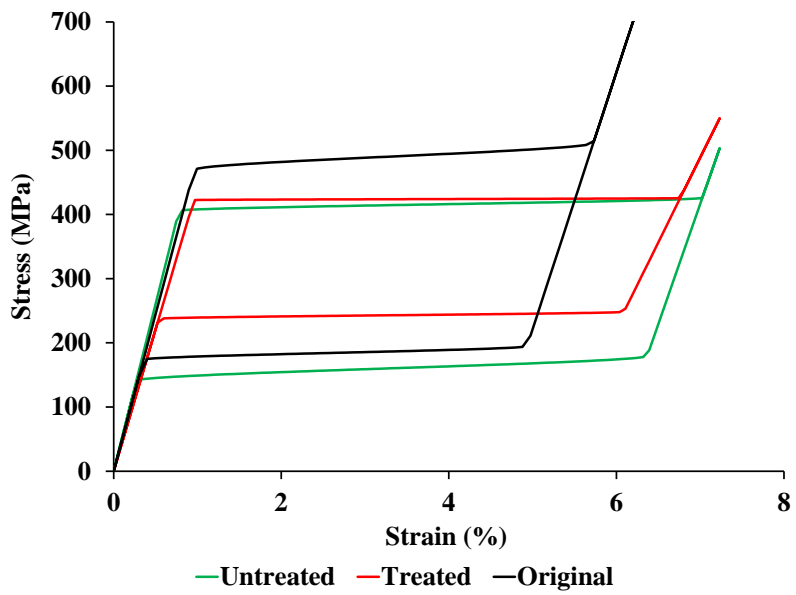
Figure 3.18: Comparison of calibrated constitutive models at 25°C.

3.4.2   Changes to Fluid Model

Many changes were required to make the fluid model compatible with FSI analysis. The most significant change was the implementation of the overset mesh. During slat retraction as the SCF is stowed into its retracted configuration, there is significant reduction and elimination of volume in the slat cove. Numerical instabilities were introduced that can make the FSI analysis unstable as elements in the fluid volume approach zero volume. The change in volume can be handled by remeshing the fluid model every cycle, but this would be very computationally expensive. An alternative is the overset mesh approach, which overlaps movable (and deformable) slave meshes onto a master mesh allowing for complex motion and contact of solid bodies. This is significantly faster as compared to remeshing. When using an overset mesh, parts of the mesh are not analyzed for the following conditions: 1) a part of the master mesh that is overlapped by the slave mesh, 2) a part of the slave mesh that does not overlap the master mesh and 3) a part of the slave mesh that overlaps a solid in the master mesh. Information is exchanged through interpolation between the nodes on the outer surface of the slave mesh and the surrounding elements in the master mesh. For better interpolation, it is recommended that the master region have a finer mesh than the slave region at the boundary between the two meshes. Note that when two slave meshes overlap each other, the section of the master mesh contained within the overlapping region of both slave meshes is used in the analysis.

For this problem, the main wing, flap and tunnel test section were set to be the master mesh since those volumes were fixed for all considered FSI analyses. The slat and SMA SCF were set as slave meshes (see Fig. 3.19) since retraction/deployment of those sections was needed for some FSI analyses. In CFD analysis, the slat and SMA SCF were combined into a single rigid solid, removing the fluid in the slat

cove. However, for FSI analysis of the SCF, the SCF and slat were separated to accommodate large changes in volume that required the reintroduction of the slat cove. As the SCF was deformed by contact with the main wing, its associated fluid mesh in the slat cove would also deform. Eventually the fluid mesh would pass through the wall of the slat while the wall boundary condition was maintained, allowing the volume in the slat cove to shrink. Due to the overlap of the slat and SCF slave meshes, some boundary conditions (specifically the wall condition of the SCF) could be ignored at the start of the analysis. This influenced how the slave meshes were designed.

Overall Mesh

Master Mesh
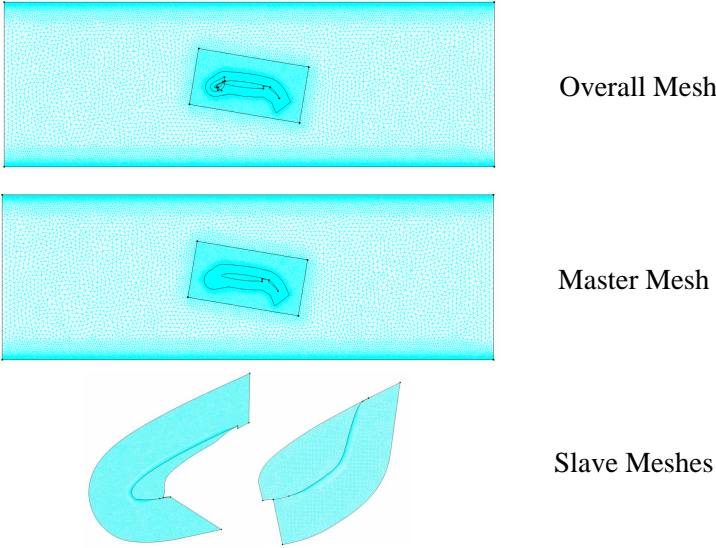
Slave Meshes

Figure 3.19: Implementation of overset mesh.

Figure 3.20 shows an example of the interaction between the slave and master meshes by separating the velocity contour between the two types of meshes. As seen in the master mesh (Fig. 3.20(a)), there were almost no flow results in the vicinity of the slat and SCF due to that region of the master mesh being overlapped with

slave meshes. Instead the flow results were present in the slave meshes, as shown in Fig. 3.20(b). In the vicinity of the slat and SCF, only in regions where both slave meshes overlapped each other (such as the slat cusp and slat trailing edge) was the master mesh used in analysis of the flow.[9] Interpolation between the slave and master meshes is also visible in Fig. 3.20. At the outer boundary of the slave meshes, the master mesh elements interpolated data from the nodes on the slave mesh. Also, at the leading edge of the main wing, the slave mesh interpolated data with the master mesh due to the presence of a solid body.

(a) Master mesh (slave meshes suppressed).   (b) Slave meshes (master mesh suppressed).
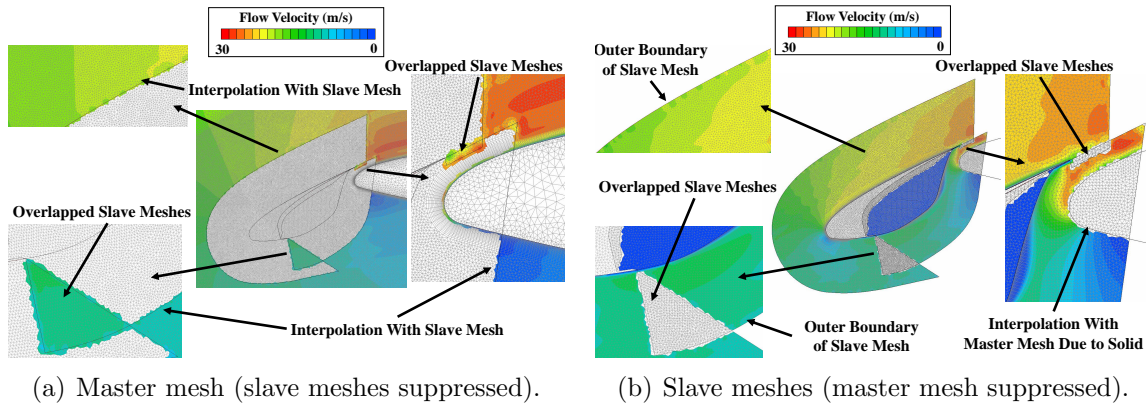
Figure 3.20: Interaction between the slave and master meshes for the CRM FSI model.

Along with the overset mesh, a new boundary condition was also needed. This boundary condition was a zero pressure applied to the fluid in the slat cove since the fluid was enclosed and incompressible while undergoing deformation. Without this condition, deformation of the SCF resulted in numerical instabilities that crashed the analysis. As a result of the slat cove containing fluid, the outer surface of the

---

[9]A small region inside the slat cove could be analyzed by the master mesh if the interior of the slat was considered to be a fluid volume.

SCF was assigned as a panel (wall that separates fluid) maintaining the no slip wall boundary conditions. Note that some FSI attempts (specifically retraction cases) showed that replacing the interior of the slat with fluid and applying a zero pressure boundary condition assisted the analysis, specifically with the interaction between the slave and master meshes.

During initial FSI analysis attempts of the SCF retraction, when the SCF came into contact with the leading edge of the main wing, numerical instabilities in the fluid model due to contact between the SCF and main wing occurred and led to the eventual crash of the analysis. To avoid this instability, the outer mold line of the main wing in the fluid model was negatively offset by 0.127 mm. As a result, when the SCF came into contact with main wing in the structural model, there was small gap between the two parts in the fluid model preventing the introduction of the instabilities associated with contact.

Finally, the other significant change to the fluid model was the size of the elements in multiple sections of the model. Multiple factors influenced the size of the elements including the implementation of overset meshes, the overlapping of the slave meshes and the transfer of data between the fluid and structure models. As mentioned earlier, the element size of a slave mesh was typically required to be larger than its corresponding master mesh. To maintain an element size in the slave meshes similar to the one used in CFD analysis, the inner region of the master mesh needed to be refined. The overlapping slave meshes was the most influential factor on the element sizes in the fluid model. Maintaining the wall boundary condition on the SCF surface required multiple iterations of adjusting the master and slave mesh element sizes to create a stable model. Finally, having a refined mesh near the surface of interest for FSI analysis allowed for more data to be transferred between the structure and fluid models, improving the results. After multiple iterations, a stable mesh was

created. The master mesh had element sizes of 0.07 mm, 0.56 mm and 2.24 mm for the inner, middle and outer regions respectively. In addition, in the vicinity of the slat and SCF, the master mesh was further refined to an element size of 0.035 mm. The slat and SCF meshes had element sizes of 0.04 mm and 0.045 mm, respectively. The change of thickness between prism layers and the total number of layers were adjusted for each mesh in order to maintain the same prism layer size as the CFD model without distorting the mesh. Note that prism layers were not inserted near the overlapping regions of both slave meshes avoid potential numerical errors.

Figure 3.21 shows the pressure coefficient distribution from CFD analysis of the CRM in the fully-deployed configuration at 6° and 8° angle of attack with an inlet velocity of 15 m/s for the original fluid model and the modified fluid model for FSI analysis. As seen in this figure, the pressure distribution across the surface of the wing was similar for the two meshes. The main difference between the two models was that the original model had a slightly more developed suction peak and distribution on the upper surface. In addition, pressure was lower at the leading edge of the main wing possibly due to interpolation between the meshes. With regards to flow separation on the upper surface of the flap, at 6° both models predicted separation in approximately the same location while at 8° the modified model predicted separation further aft than the original fluid model. The difference in pressure distribution also effected the overall lift and drag as shown in Table 3.2. The lift and drag coefficients for both models were within 10% of each other except for the drag coefficient at 8°. The drag coefficient for the modified model at this angle of attack was 57.8% higher than the drag coefficient for the original fluid model. Examining the drag from each of the components of the model at this angle showed that the main wing had significantly higher drag than it did in the original fluid model. Differences in the flow results could be due to the interpolation between the slave and master meshes

specifically at the leading edge of the main wing. In addition, the removal of prism layers near the overlapping slave regions could result in a loss of accuracy in the calculation of the drag. Further mesh refinement near the leading edge of the main wing and adjustment of the slave mesh boundaries should improve the results.

(a) 6° angle of attack.   (b) 8° angle of attack.
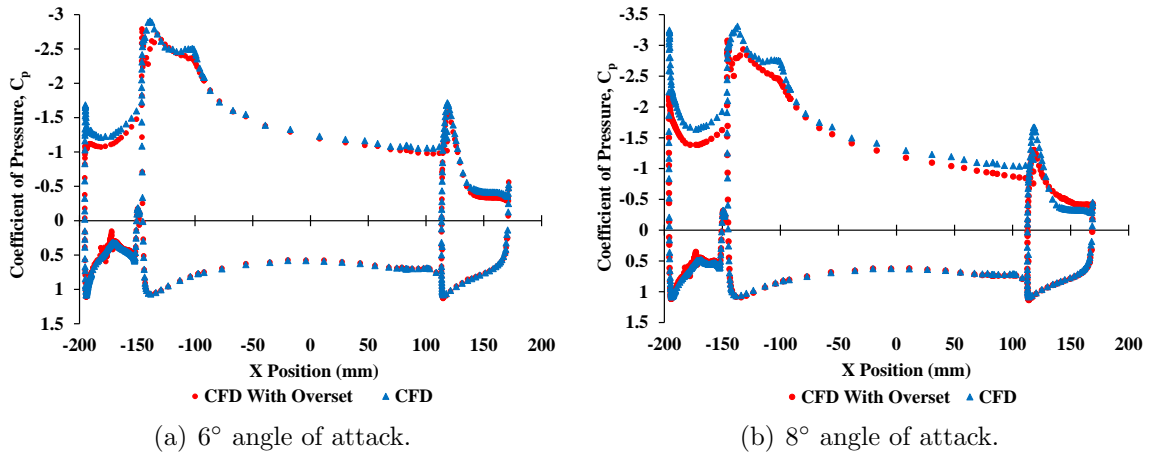
Figure 3.21: Comparison of pressure coefficient distribution between the original fluid model and modified fluid model for FSI analysis.

3.4.3   Linking the Computational Models

A significant factor for using SC/Tetra was its built-in link to the Abaqus Co-Simulation Engine. The two solvers were weakly coupled meaning that each program solved its physical quantities separately. The coupling was bi-directional so SC/Tetra sent a pressure vector acting on a specified surface while Abaqus sent displacement of that surface. The chosen time marching technique for the coupled analysis was Gauss-Seidel. In this method, Abaqus calculated cycle n+1 for the structural model based on fluid data from cycle n in SC/Tetra. Then SC/Tetra calculated the n+1 cycle for the fluid model based on the displacement data from the n+1 cycle of

Table 3.2: Lift and drag coefficient comparison for original and modified fluid models.

Angle	C_l	C_d
(Original)		
6°	2.37	0.0874
8°	2.58	0.0868
(Modified)		
6°	2.29	0.0958
8°	2.41	0.137

Abaqus. During FSI analysis, both SC/Tetra and Abaqus had the same time step. For this work, prior to running FSI analysis, CFD analysis was conducted on the fluid model at a chosen inlet speed till a specified time (cycle n). The results of the CFD analysis were then used as input data for the FSI analysis. Specifically, Abaqus would use the input data (and time of cycle n) to calculate cycle n+1. Using an initial CFD analysis as input data avoided having to increase flow velocity from zero to the desired speed during FSI analysis saving a significant amount of computational runtime. This framework is illustrated in Fig. 3.22. The time step for both solvers was 0.00005 s. Output from the structural model was recorded every 0.0005 s (Nyquist frequency of 1000 Hz) while output from the fluid model was recorded every 0.005 s. Global pressure and viscous forces acting on the surface of the wing were recorded every cycle.

Linking the structural and fluid computational models required that the same coordinate system be used. Therefore, every angle of attack considered required a unique fluid and structural model. The SCF was the only surfaced linked between the solvers since it was the only deformable part.
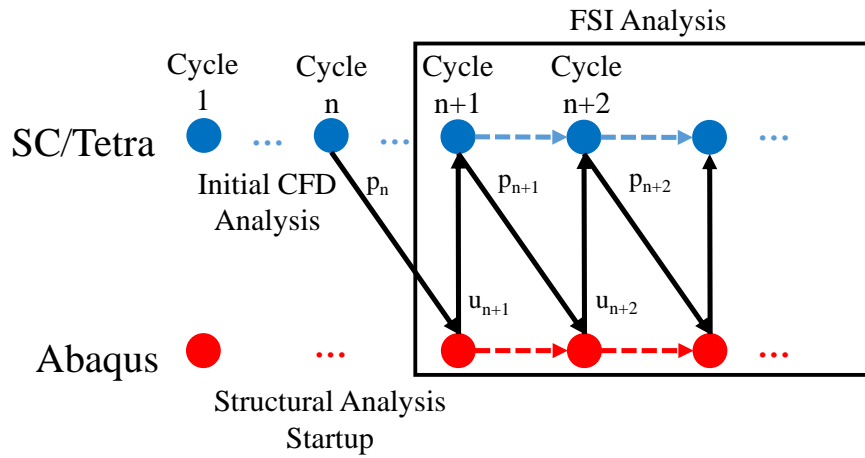
Figure 3.22: Illustration of FSI framework.

3.4.4 Load Case: Fixed Fully Deployed

The first load case considered in FSI analysis was the aerodynamic loading of the fully deployed SCF. In this analysis, the slat was fixed and the hinge was able to freely rotate. Multiple inlet speeds and angles of attack were considered for this load case.

For 15 m/s inlet flow, FSI analysis was conducted on models at 6° and 8° angle of attack using input data from initial CFD analysis of the fluid model. Computational runtime for this load case was approximately 1.5 days. Figure 3.23 shows the deflection over time at the maximum deflection point on the SCF for both angles of attack. At the beginning of the FSI analysis, the SCF displacement significantly fluctuated due to the initial interactions between the fluid and structural models, but dampened to a much smaller magnitude by 0.1 s. The average maximum displacement of the SCF at 6° and 8° angle of attack were 0.0298 mm and 0.0290 mm respectively. These

average displacements (approximately 40% of the SMA thickness) were reasonable when compared to a static analysis using the pressure distributions from CFD analysis. As seen in Fig. 3.24, the displacement of the SCF was similar in both the FSI analysis and static analysis. At 8°, the SCF had approximately the same maximum deflection in both FSI and static analysis (deflection was 0.0291 mm). However, at 6°, the SCF had a 10.7% higher defection (0.033 mm) in static analysis as compared to the deflection in the FSI analysis. Differences in the displacement could be due to slight differences in the pressure distribution between the two models. Based on the scaling laws discussed earlier in this section, this analysis corresponded to a full scale SCF with a thickness of 3.35 mm at Mach 0.2. The full scale SCF displacements at 6° and 8° angle of attack were 0.477 mm and 0.464 mm, respectively.
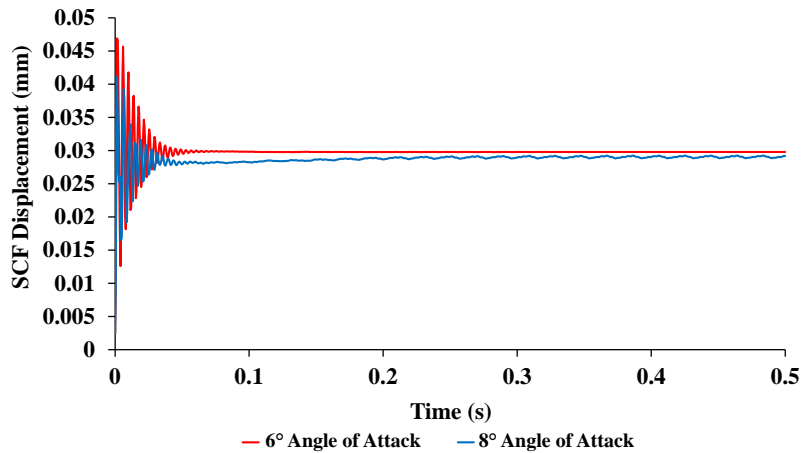
Figure 3.23: SCF displacement in FSI analysis with 15 m/s inlet flow.

As seen in Fig. 3.23, the fluctuation of the maximum SCF displacement after the dampening at the start of FSI analysis was quite small (less than 0.001 mm). To determine the frequency of the SCF deflection, a Fourier analysis was conducted using

(a) 6° angle of attack.   (b) 8° angle of attack.
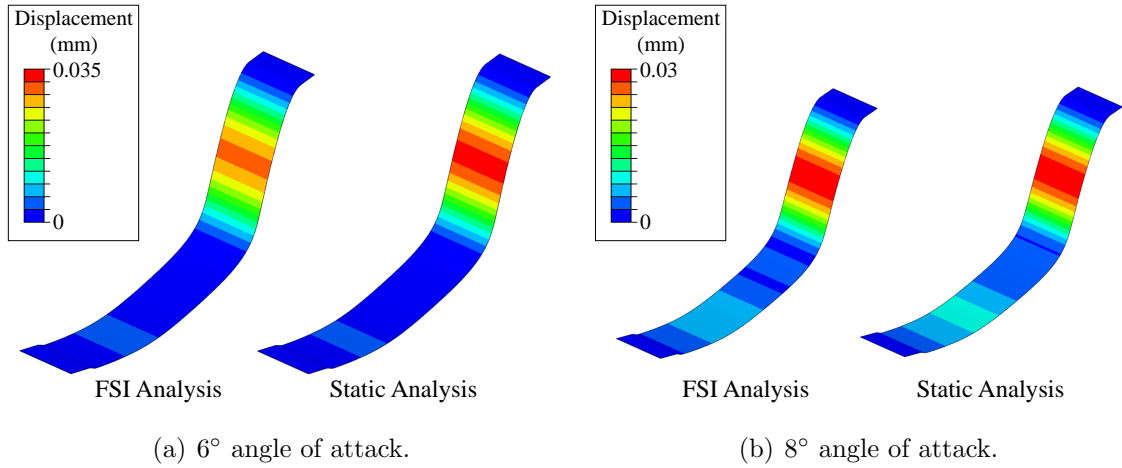
Figure 3.24: Comparison of SMA SCF deflection between FSI analysis and static aerodynamic loading.

the last 0.25 s of the FSI analysis (512 data points since displacement was recorded every 0.005 s). The resulting frequency resolution was approximately 4 Hz. As shown in Fig. 3.25, at 6° the SCF appeared to be vibrating at a frequency of 74 Hz, while at 8°, it vibrated at 50 Hz. The root mean square (RMS) value for the spectrum at 6° and 8° were 3.35*10^{-6} and 1.13*10^{-4}, respectively.[10] These frequencies appeared to be fundamental since there appeared to be harmonic frequencies. As expected, the amplitude of the frequencies at 8° was significantly higher than the ones at 6° since the fluctuation of SCF displacement was higher. Given that the amplitude of the frequencies for both angles was small, the fluctuation of SCF displacement could be due to numerical noise in the analysis.

Flow results were also re-examined to account for changes due to the introduction of a flexible SCF to the flow analysis. For 6° angle of attack, the average lift and drag coefficients were 2.29 and 0.0963, respectively. These coefficients were approximately the same as the coefficients from the initial CFD analysis (see Table 3.2). However,

---

[10]The RMS value was calculated from the spectrum plot by first summing the squared value of each magnitude, and then taking the square root of that sum and multiplying it by $\frac{\sqrt{2}}{2}$.

(a) 6° angle of attack.
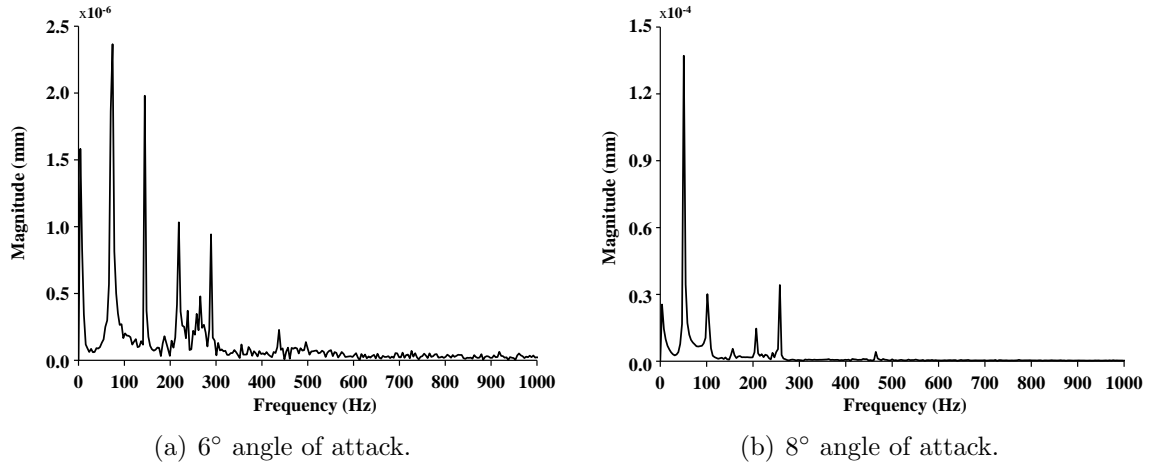
(b) 8° angle of attack.

Figure 3.25: Spectrum magnitude plot of SCF deflection at 15 m/s in fully deployed configuration.

for 8° angle of attack the average lift and drag coefficients in FSI analysis were slightly different from the values in the initial CFD. The lift coefficient was 2.35 (2.49% lower) while the drag coefficient was 0.147 (7.30% higher). Also, though it is not shown, the pressure coefficient distribution was practically unchanged for both angles. At these angles and inlet speed, the SCF does not appear to significantly change the flow results.

FSI analysis of the fixed fully deployed configuration at 6° angle of attack was also conducted with an inlet speed of 30 m/s. The SCF deflection over time is shown in Fig. 3.26(a). Similar to the results using 15 m/s inlet speed, the SCF displacement significantly fluctuated at start of the analysis, but quickly dampened. The SCF deflected shape was also similar to the 15 m/s cases, as shown in Fig. 3.26(b). The average/steady maximum displacement of SCF was 0.124 mm which was approximately four times the maximum displacement for both 15 m/s cases. Also, the maximum displacement occurred in approximately the same location (distance of 0.39 mm between the two points) as the maximum displacement for the 15 m/s case.

These results were expected given that the dynamic pressure (and thus the load acting on the SCF) increased by a factor of four. Even at 30 m/s inlet speed, the fluctuation of the SCF displacement was very small (less than 0.001 mm). Fourier analysis of the SCF displacement on the last 0.5 s of the analysis showed the SCF was vibrating at a frequency of approximately 240 Hz (see Fig.3.27). The RMS value of the spectrum was $2.87*10^{-6}$. Given the size of the amplitude, this frequency could be due to numerical noise. Performing a Fourier analysis on the lift coefficient from the initial CFD analysis showed that the lift was fluctuating at similar frequencies as the SCF displacement. This further suggested that the frequency of SCF vibration was due to numerical noise. This analysis corresponded to a full scale SCF with a thickness of 2.21 mm at Mach 0.2 and a maximum displacement of 1.984 mm.

(a) Maximum SCF displacement vs. time.　　　　(b) Contour plot.
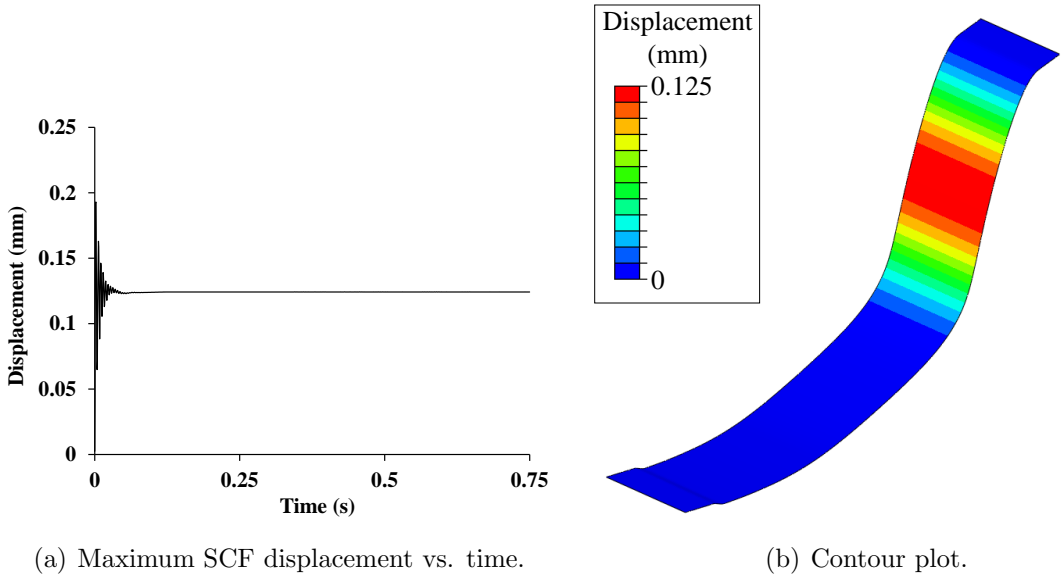
Figure 3.26: SCF displacement in FSI analysis with 30 m/s inlet flow.
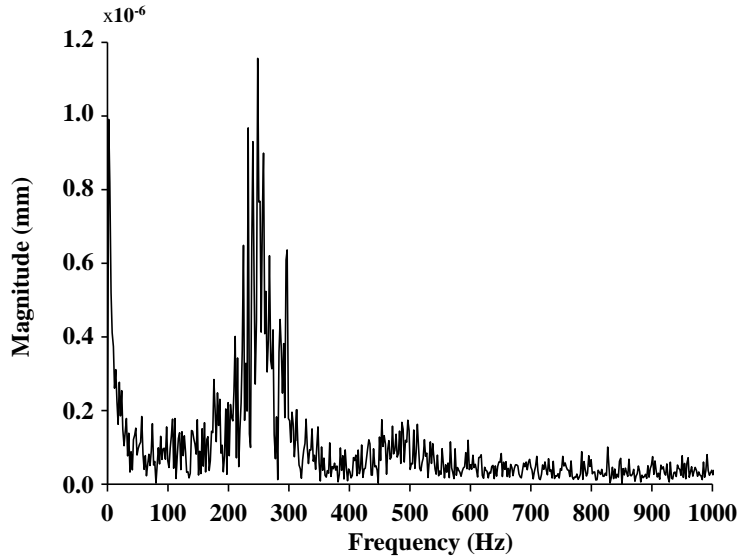
Figure 3.27: Spectrum magnitude plot of SCF deflection at 30 m/s in fully deployed configuration.

3.4.5 Load Case: 14% Slat Retraction (SCF Touching Wing)

The second load case considered was aerodynamic loading of the SMA SCF when the slat setting placed the SCF in contact with the main wing. After the initial CFD analysis of the fixed fully deployed SCF, the slat and SCF were rotated about the slat rotation center to approximately 14% retraction (0.06 radians) over 0.14 s, where the SCF first comes into contact with the main wing. The SCF was then held in this position for another 0.38 s. Note for this analysis, to assist with retraction, the interior of the slat was treated as fluid. Total runtime of the FSI analysis was approximately two days using a 4 core computer. Recall that in the FSI analysis, the outer boundary of the main wing was negatively offset in the fluid model to create a small spacing between the main wing and SCF when the two parts come into contact in the structural model. Only a 6° angle of attack configuration at 15 m/s was considered. The purpose of this load case was to begin assessment of

90

the SCF compliance to retraction. In addition, this load case provided another SCF configuration to compare with the wind tunnel model.

As shown in Fig. 3.28, there was a small region of high-velocity flow in the gap between the SCF and main wing, but it did not appear to effect the overall flow. There were also some disturbances due to interpolation at the boundaries of the slave meshes that propagated downstream. Since the boundaries were (mostly) away from the surface of the slat and SCF, the effect of the disturbances was small on the flow near the SCF. Investigation into the creation of these disturbances is currently in progress. Further refinement of the slave mesh or adjustment of its outer boundary may reduce the propogation of the disturbances. With the SCF touching the main wing, it effectively prevented fluid from flowing across the leading edge of the main wing, resulting in the separation of flow off of the slat/SCF. The separation created circulation regions on either side of the main wing's leading edge and eventually reattached to the wing further downstream. This meant that with the SCF implemented, above 14% retraction the slat was effectively an extension of the main wing and not a separate body.

The effects of the SCF contacting the main wing can be further seen in the pressure coefficient distribution shown in Fig. 3.29. On both the upper and (especially) the lower surfaces, there appeared to be a smooth transition from the pressure on the slat/SCF to the pressure on the main wing. In addition, the suction peak on the slat grew since the it was at a higher effective angle attack which also corresponded to a negative increase in the pressure on the lower surface.

The "combining" of the slat and main wing created a longer main wing with more camber, which corresponded to a slight increase in the lift coefficient (2.40). The drag coefficient also slightly increased (0.0992) more than likely due to the creation of the circulation regions between the slat and main wing. Further investigation
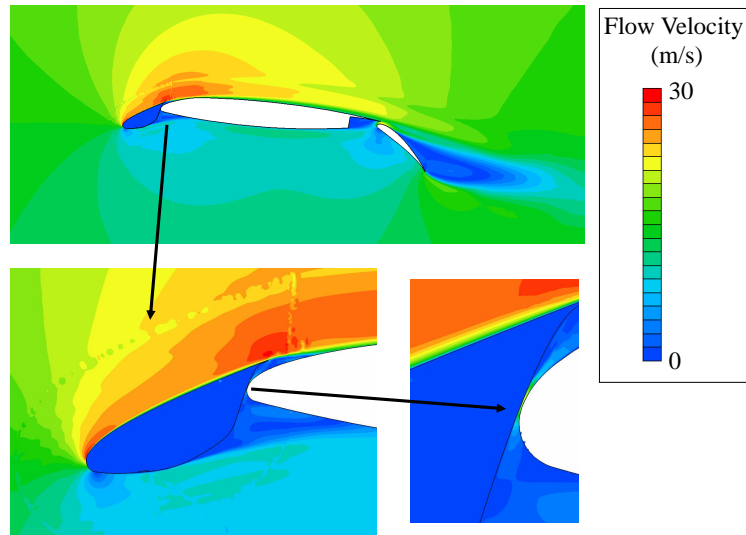
Figure 3.28: Velocity contours at 14% slat retraction.
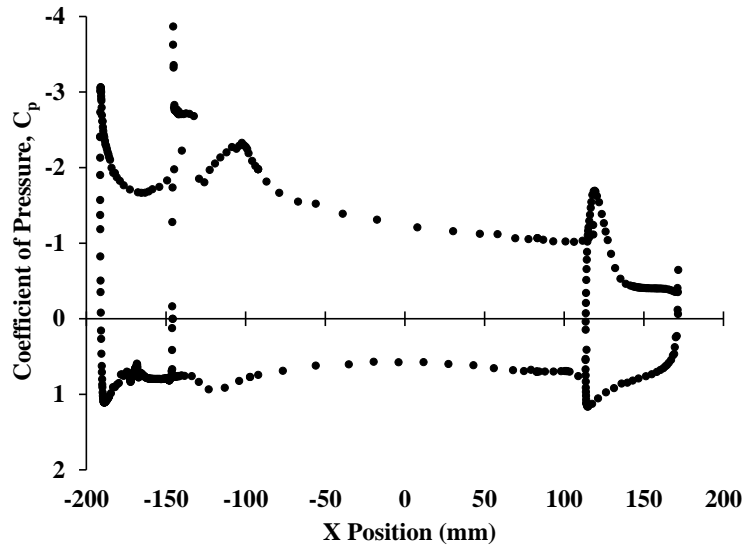
Figure 3.29: Pressure coefficient distribution at 14% slat retraction.

into the effect of the SCF at this retraction level (and higher) on the overall flow is necessary since above 14% retraction the SCF created a morphing wing whose camber could be set by simply retracting/deploying the slat. However, aeroacoustic

effects will also need to be taken into consideration since two circulation regions were created.

In order to obtain the frequency of any SCF vibrations in this configuration, Fourier analysis was conducted on the displacement of the SCF once it was in contact with the main wing. As with the previous load case, the last $0.25\,\mathrm{s}$ of the FSI analysis was used (512 data points). From Fig. 3.30, it can be seen that the SCF was vibrating at approximately $84\,\mathrm{Hz}$. The RMS value for this spectrum was $1.44*10^{-5}$. Given the small spectral magnitude at that frequency, this vibration could be the result of numerical noise.
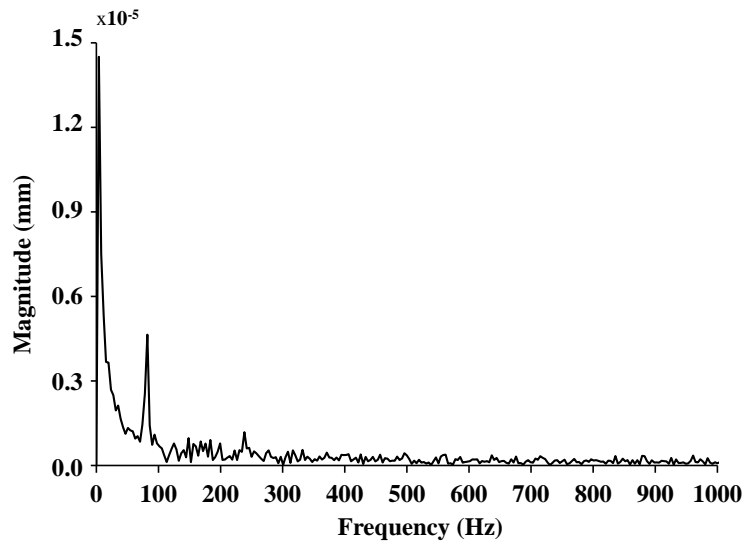
Figure 3.30: Spectrum magnitude plot of SCF deflection at $15\,\mathrm{m/s}$ at 14% retraction.

3.4.6   Load Case: Full SCF Retraction/Deployment

The final load case was FSI analysis of the full retraction/deployment of the slat. However, at the time of this work only slat retraction was performed. Note

that slat retraction under flow was not a physically meaningful case. However, this analysis deformed the meshes of the slat and SCF into a configuration suitable for slat deployment while the boundary conditions of the slat-cove and walls of the SCF and slat were maintained. This analysis was conducted with a previous iteration of the fluid model (prior to mesh refinement and prism layer studies) which was used to develop the techniques and modeling choices used in the current iteration. The model had approximately 1,360,000 elements (1,351,000 prism and 9000 hexahedron). In addition, an artificial thickness of 0.25 mm was added to the main wing in the structural model such that the SMA SCF never contacted the main wing in the fluid model. This was essentially the opposite of what was done in the most recent iteration of the fluid model. In addition, this analysis was conducted prior to the tension tests of the SMA so SMA material properties from Section 2 were used.[11] The slat in both the fluid and structural models was set to rotate over 2 s about the same point (slat reference point), which was faster than flight hardware (typically 10 s to 20 s) but necessary for reasonable computational runtime. As with the previous load cases, the FSI analysis used input data from CFD analysis of the model with an inlet speed of 15 m/s. The computational runtime for this analysis was significant, requiring multiple days to complete. The analysis crashed at approximately 94% slat retraction due to a zero volume element in the fluid mesh associated with the SCF. The mesh deformation due to the slat retraction, hinge rotation and SCF deformation contributed to the creation of the zero volume element. The velocity contours at various stages of slat retraction are shown in Fig. 3.32. Note that any velocity inside the slat cove was also a result of the overlap between the slave meshes, but in this case could not be prevented. Local disturbances due to interpolation between the slave

---

[11]The wind tunnel version of the SCF had also not been constructed yet. The hinge was set to 0.5 mm away from the slat-cove wall and the hinge arm length was set to 1.5 mm.

94

and master meshes was evident at all retraction levels. As with the 14% retraction load case, there was a small region of high-speed flow in the gap between the SCF and main wing. In addition, the SCF created two circulation regions on either side of the leading edge of the main wing at multiple retraction levels. However, this effect appeared to diminish near the end of slat retraction. The deformation of the fluid volume inside the slat cove is also shown in Fig. 3.32. At 40% retraction, there were local disturbances near the upper surface of the slat. These disturbances were due to the outer boundary of the SCF fluid mesh, originally in the slat cove, passing through the slat slave mesh. As the slat was further retracted, the disturbances moved further from the upper surface of the slat to accommodate the shrinking slat cove volume. This proved that the treatment of the slat cove as a fluid and the separation of the slat and SCF was a good modeling choice.
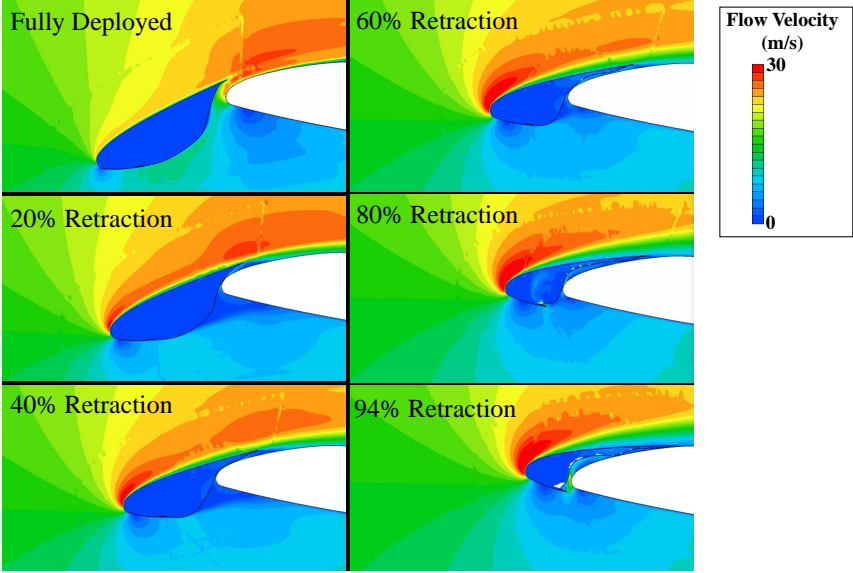
Figure 3.31: Velocity countours of FSI retraction analysis.

Figure 3.32 shows the actuation force about the slat rotation center versus percent retraction for slat retraction with flow (FSI analysis) and without flow (structural analysis) up to 94% retraction. As seen in the figure, the actuation force curve from FSI analysis oscillated slightly while the curve from structural analysis was smoother. The oscillations were due to the aerodynamic loading of the SCF. Under flow, the actuation force was decreased for most of the slat retraction as compared to retraction without flow. The aerodynamic loading on the SCF assisted with its retraction. Past 75% slat retraction during FSI analysis, most of the SCF was essentially untouched by airflow resulting in approximately the same actuation force curve as the structural analysis. Note that since the outer mold line of the main wing was extended by 0.25 mm, the actuation force was artificially higher due to the smaller space between the main wing and slat. Prior to contact with the main wing (approximately 14%), the aerodynamic loading of the SCF resulted in negative actuation force. This meant that the aerodynamic loading was attempting to further retract the slat/SCF. For the scale (6.25%), inlet speed (15 m/s) and span (12.7 mm), the peak actuation force was approximately 0.35 N. The corresponding peak actuation force at full scale was 1850 N for a SCF with 2.23 mm and a spanwise length of 203.2 mm at Mach 0.2. Note that the optimal design for the SCF profile from Section 2 had a maximum actuation force of 22.3 N for a 19.05 mm spanwise section at 75% scale. At full scale and with a spanwise length of 203.2 mm, the optimal SCF design had a maximum actuation force of 310 N (approximately six times smaller than).
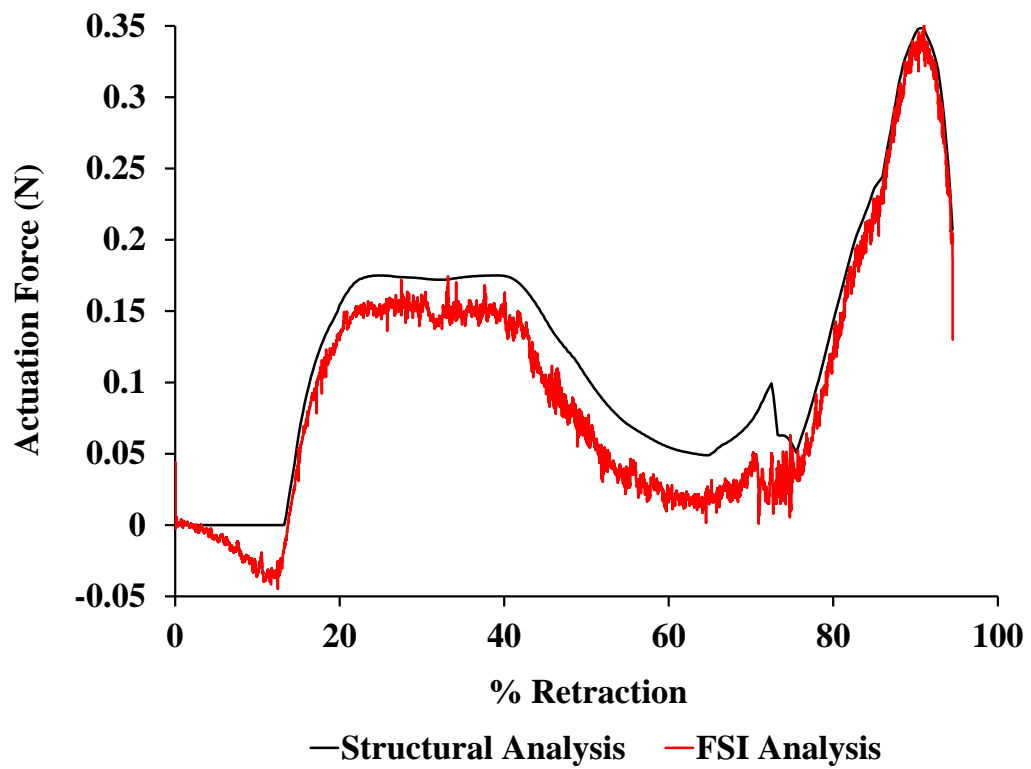
Figure 3.32: Actuation force for FSI and structural analysis.

4. WIND TUNNEL TESTING AND VALIDATION OF SCF FOR CRM GEOMETRY

While CFD and FSI results were useful in understanding how the SCF behaved under flow, the computational models needed to be validated against a physical model. Validation of the computational model would allow for its results to be trusted. A validated model could then be used to consider load cases and scales (full scale and higher speeds) that as of now cannot be physically tested.

4.1 Physical Wind Tunnel Model Description and SCF Implementation

The physical model was constructed and tested in parallel with the computational model. Section 4.1 presents a general description of the wind tunnel model, the instrumentation and test methods used used to study it and the implementation of the SCF.

4.1.1 Wind Tunnel Model Description

The physical wind tunnel model was also based on a 6.25% scaled 2D section of the CRM at mid-span of the outboard slat and parallel to freestream flow. Solidworks was used to design the model (see Figure 4.1). An aluminum spar consisting of two plates and a web served as the main structural support for the wing. 3D printed, plastic shells were connected to the spar to obtain the shape of the main wing outer mold ling (see Fig. 4.2).

Remote controlled, Firgelli L12 linear actuators were installed inside the main wing and connected to the slats and flaps (see Fig. 4.3) allowing for the testing of multiple slat/flap configurations. Three actuators (one at each end and one in the middle of the wing) were used for each high-lift device. The retraction/deployment
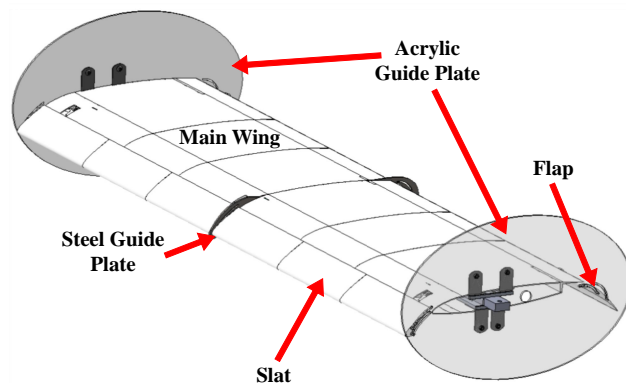
Figure 4.1: SolidWorks model of wind tunnel model.
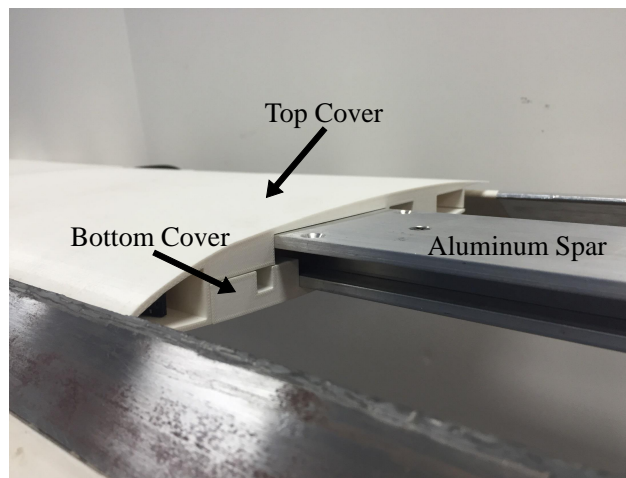
Figure 4.2: 3D plastic covers connected to aluminum spar.

path for the slat and flap were defined by tracks in a steel plate at the middle of the main wing (separating the wing into two $0.61\,\mathrm{m}$ spanwise sections) and two acrylic splitter plates at either end of the wing. Due to their small size, the slats and flaps were also built using a 3D printer and stiffened with embedded steel rods (see Fig. 4.4). The steel rods also served as pins, passing through the tracks in the steel and

acrylic plates. Two variations of slats were built: 1) an unmodified slat based on the CRM geometry and 2) a modified slat that was compatible with stowage of the SCF. The latter slat had a steel trailing edge to allow for better bonding with the SCF, a steel cusp and paper hinges bonded to the cove wall to allow for the SCF to freely rotate. The hinge axis for the paper hinges was against the cove wall and the hinge length was approximately 8 mm. In addition, the cove in the slat was increased, relative to the unmodified slat, by removing material from the slat along the cove wall, thereby creating more space to stow the SCF
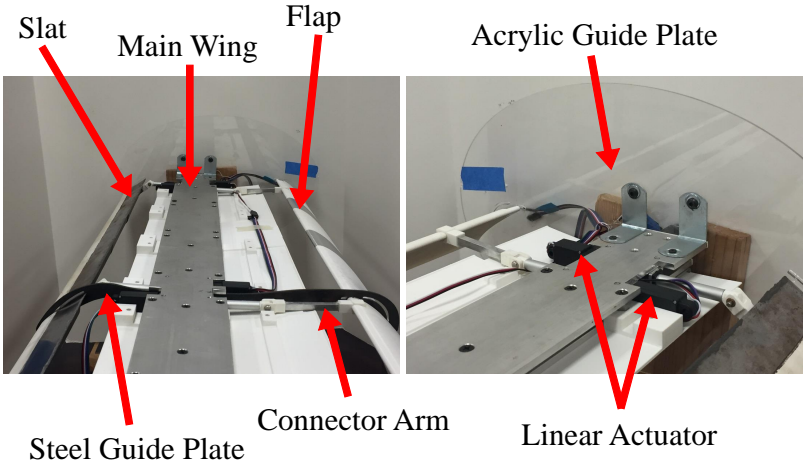
Figure 4.3: Linear actuators and slat/flap tracks.

The model was connected at both ends to ATI Delta F/T load cells in a test section for the Texas A&M University 3 ft-by-4 ft tunnel (see Fig. 4.5). One load cell was connected to a gear system that controlled the angle of attack of the wing while the other was free to rotate. The load cells were to able measure forces and moments in all three directions. However, only the forces corresponding to lift and drag were of interest in this work. The model was also connected to a US Digital inclinometer
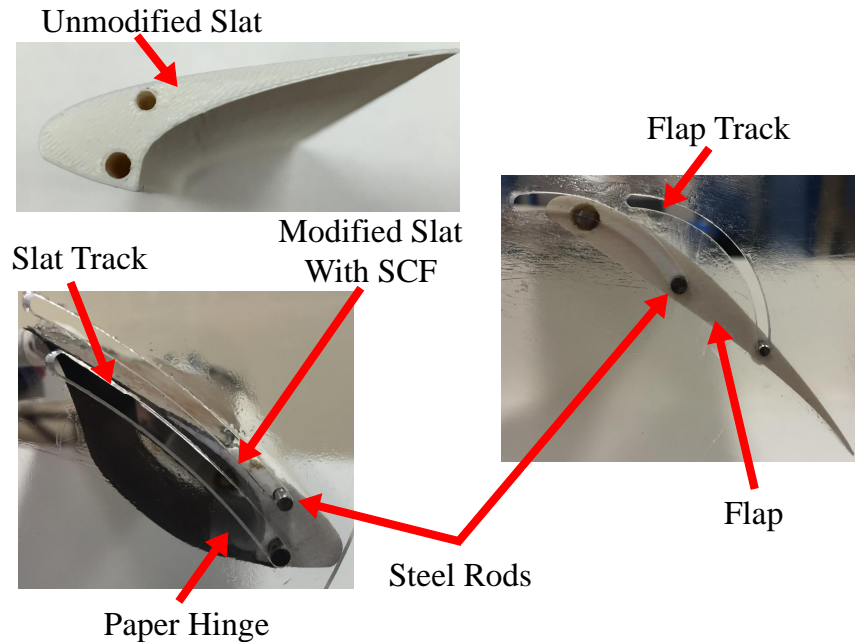
Figure 4.4: Trailing-edge flap and leading-edge slats.

for angle of attack measurements. The inclinometer was tared when the spar was approximately 0° (horizontal) using a Lucas AngleStar digital protractor.[1]

Pressure along the surface of the main wing was measured at quarter-span using a Pressure Systems Minature Electronic Pressure Scanner (shown in Fig. 4.6). Medical grade tubes were glued to drilled holes in the surface of 3D printed sections of the main wing and connected to the pressure scanner outside of the tunnel. The location of each hole was marked during the printing of the parts to ensure accurate hole placement. Figure 4.7 shows an illustration of the locations where pressure was measured. Pressure measurements at a wind-off (no flow) condition were used to tare the measurements at other conditions. Due to their small size, pressure measurements could not be taken on the slat and flap with the current system.

---

[1]An angle of 0° corresponds to an angle of attack of -1.48°. This was determined in the SolidWorks model by measuring the angle between the retracted chord line and the horizontal. This was taken into account during the post processing.
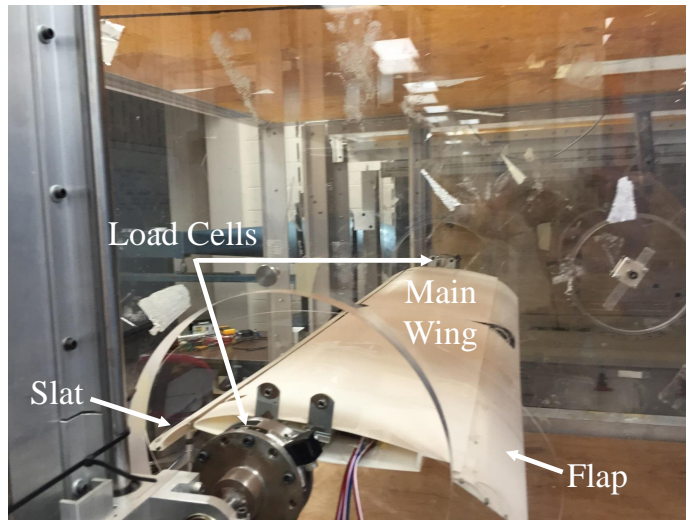
Figure 4.5: Wind tunnel model of CRM wing 2D section.

Figure 4.6: Pressure scanner with tubing.

The displacement of the SCF was to be measured using a Keyence IL-600 Laser Displacement Sensor (Fig. 4.8(a)). The sensor was connected to a custom fixture (shown in Fig. 4.8(b)) that could translate in the chordwise direction and rotate in
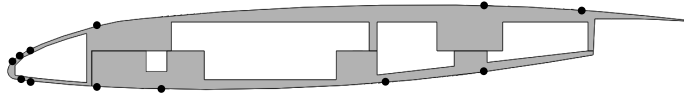
Figure 4.7: Illustration of locations for pressure measurements on the main wing.
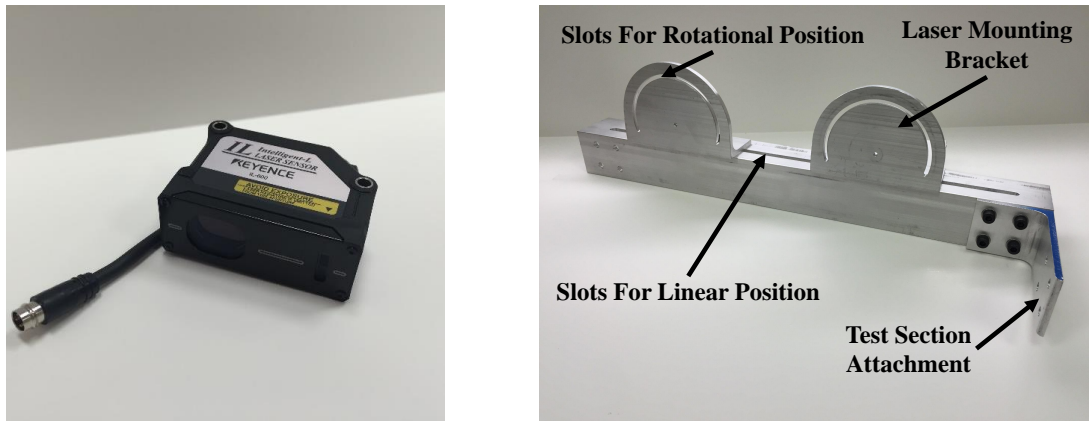
(a) Laser sensor.

(b) Laser mount.

Figure 4.8: Laser displacement measuring system.

the spanwise direction. The fixture was connected to a support beam underneath the test section. Slots were cut into the floor of the test section to allow for the laser to be pointed at the wing. The sensor was set to measure the dynamic displacement with a bandwidth of 0-500 Hz. The fixture could accommodate two sensors, but at the time of this work only one sensor was ready for use.

4.1.2   SCF Implementation

Due to the small size (curvilinear length of the SCF was approximately 5 cm), creating a segmented, multi-flexure SCF would be difficult to manufacture. Thus, to simplify the manufacturing process, only a monolithic SCF was considered. In the

determination of the SMA thickness, a formal design optimization was not conducted since manufacturing SMA panels with a custom thickness at the current scale (less than 0.1 mm) was expensive. Instead discrete thicknesses were evaluated using the load cases of the structural model. Also note, as this analysis was conducted prior to purchasing the SMA material for the SCF, material properties shown in Section 2 were used. In addition, the hinge length was held at approximately 1.8 mm long and hinge location was held at approximately 0.5 mm away from the cove wall for this design since the hinge had not been constructed at the time. A thickness of 0.0762 mm (0.003 in) required a reasonable amount of actuation force and it did not significantly deflect under static aerodynamic loading[2]. In addition, this thickness of SMA was readily available so it was used in the FSI analysis and physical wind tunnel model.

The fully deployed SCF profile was the zero stress state. Since the SMA sheet was flat, shape setting using a heat treatment was required to obtain the desired SCF profile. Due to size constraints in the furnace, creating a single SCF spanning the entire length of the wing was not possible. Instead multiple smaller SCF sections were created. The shape setting was performed by placing the flat SMA sheet into a custom mold (see Fig. 4.9(a)), which was then placed in a furnace at 600°C. Smaller SCF sections were treated for 22.5 min, while larger sections were treated for 30 min due to the increase in thermal mass. After the allotted time, the molds with the SCF sections were water quenched. Each mold was 7.62 cm (3 in) in length, but larger SCF sections could be created by linking the molds together (see Fig. 4.9). The treated dogbone specimen discussed in the previous section was also heat treated in this way.

Due to the small size of the SCF, it could not be connected to the slat using

---

[2]The pressure distribution for the static load was extracted from an early CFD analysis.
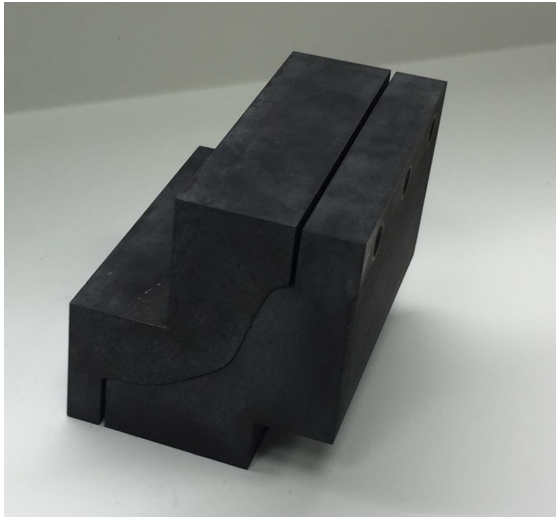
(a) Single SCF mold.   (b) SCF molds linked together.

Figure 4.9: SCF molds used for shape setting.

conventional means (bolts, screws, etc.). Instead it was bonded to the steel trailing edge and paper hinge using JB-Weld. SCF sections were installed over the entire slat expect in the vicinity of the linear actuators.

4.2   Wind Tunnel Results and Comparisons

All wind tunnel tests were conducted in the Texas A&M University 3 ft-by-4 ft tunnel. Both retracted and deployed configurations were considered with a freestream velocity of approximately 15 m/s. Lift-AoA curves for the retracted configuration from the CFD model and wind tunnel tests are shown Fig. 4.10. As seen in the figure, both the CFD and wind tunnel lift-AoA curves were linear at low angles of attack, and began to flatten at higher angles of attack as the wing approached maximum lift. With the exception of the lift-AoA curve from laminar inlet flow at high angles of attack, CFD results had a slightly higher lift than the wind tunnel results at every angle of attack. Also, the difference between the CFD and wind tunnel lift-AoA curves increased at higher angles of attack. The difference

in the lift-AoA curves was expected since the CFD model was a rigid body with smooth surfaces that did not have the geometric discontinuities caused by screws, bolts, actuator arms, etc.. The CFD model with turbulent inlet flow matched the experimental results better than the laminar inlet flow case. The lift-AoA curve from the CFD model using laminar inlet flow flattened significantly as compared to the other lift-AoA curves. In addition, stall only occurred for the CFD model under laminar inlet flow. These results suggested that the flow at the inlet of the wind tunnel test section was not laminar.
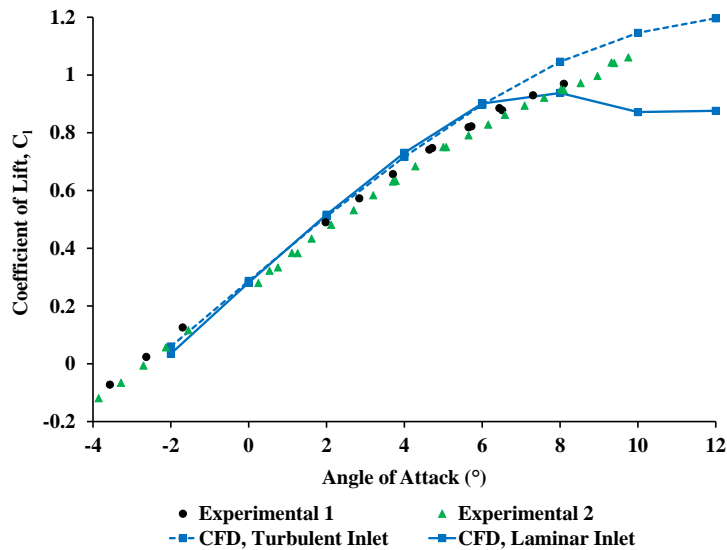
Figure 4.10: Comparison of CFD and wind tunnel lift-AoA curves for the retracted configuration.

The lift-AoA curves for the deployed configurations from CFD analysis and experimental data are shown in Fig. 4.11. Like the CFD results, the experimental results for both fully deployed configurations had similar lift-AoA curves. This showed that the addition of the SCF did not significantly effect the lift of the fully deployed

106
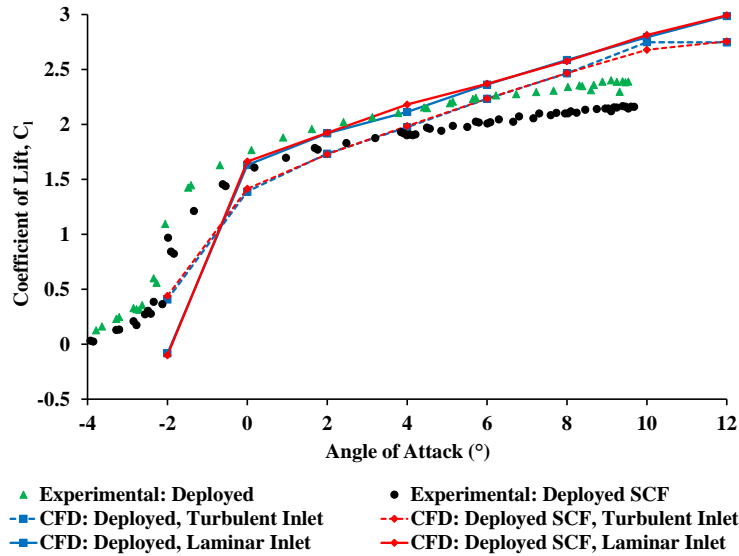
Figure 4.11: Comparison of CFD and wind tunnel lift-AoA curves for the deployed configurations.

configuration. Both CFD and experimental results showed a significant nonlinear increase at low angles of attack followed by a more linear curve starting near 0°. At low angles of attack, the linear portion of the lift-AoA curves from experimental data was between the CFD lift-AoA curves for laminar inlet flow and turbulent inlet flow. This suggested that the inlet flow was neither fully developed turbulent flow or laminar flow. Measurement of the turbulence properties at the inlet of the test section in the wind tunnel will improve the computational results. At higher angles of attack, the lift-AoA curve for the CFD model was higher in value than experimental results. The same factors affecting the results for the retracted configuration (surface roughness, geometric discontinuities) would also contribute to differences between CFD and experimental results in the deployed configurations. In addition at higher angles of attack, the slat and flap could be slightly fluttering, potentially lowering the lift. The slat and flap were rigid bodies in the CFD model, but in the

wind tunnel model they could slightly bend. Also, at higher angles of attack, there could have been blockage effects that lowered the freestream velocity in the tunnel and thus the lift of the wing. This was not present in the CFD model since the inlet speed was always set to 15 m/s. The motor for the wind tunnel was constant power driven so the drop in velocity could be counteracted by an increase in the revolutions per minute (RPM). However, the current setup for the tunnel increases the RPM of the tunnel motor in increments of 20 RPM which could make the tunnel faster than intended. An alternate solution would be to include real-time measurements of velocity into the data collection process.

The drag polars for the retracted configuration from CFD and wind tunnel tests are shown in Fig. 4.12. Note that the CFD drag polars were shifted to the right such that the drag at 0°angle of attack was the same for both experimental and CFD results. The shift was done to account for any aspects of the wind tunnel model not captured in the current iteration of the fluid model such as surface roughness in the physical model, geometric discontinuities and wall effects from tunnel walls, all of which would have increased the drag. Unmodified CFD drag polars generally had lower drag at the same lift coefficient than the wind tunnel model. As shown in the figure, at low angles, an increase in lift due to a change in angle of attack did not significantly change the corresponding drag. As maximum lift was approached, the change in drag per unit angle increased while the change in lift per unit angle decreased. One difference between these drag polars was that the wind tunnel model exhibited a decrease in drag for a corresponding increase in lift at angles of attack lower than 0°while the drag polars from the CFD model did not significantly change. Between 0° and 6° angle of attack, the shifted CFD drag polar for the laminar inlet flow case was approximately aligned with the experimental results while the shifted polar for the turbulent flow case had higher drag. Having fully developed turbulent

flow at the inlet allowed for flow to stay attached at higher angles of attack, but resulted in a loss of accuracy on the drag. Above 6°, the laminar inlet flow case no longer matched experimental results since maximum lift and stall occurred for that case resulting in significant increases in drag.
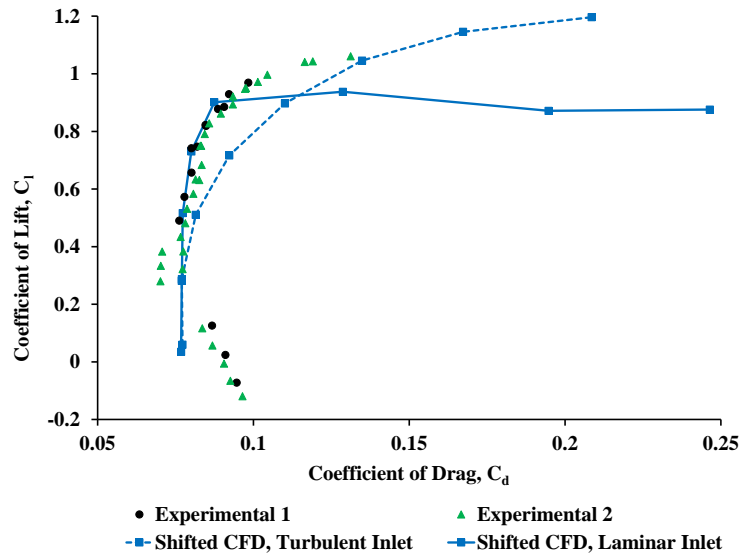
Figure 4.12: Comparison of CFD and wind tunnel drag polars for the retracted configuration.

Figure 4.13 shows the drag polars for the deployed configurations from CFD and wind tunnel tests. As with the retracted case, the CFD drag polars were shifted to the right such that the drag at 0°angle of attack was the same for both experimental and CFD results. Note that the drag polars for the turbulent inlet flow cases were shifted significantly less than the laminar inlet flow cases. There were multiple differences between the CFD and experimental drag polars. The wind tunnel results generated a smoother curve with more variation in drag while the polar from CFD results with laminar inlet flow showed little variation in drag for the highest and lowest considered

angles of attack. Above 0° angle of attack, the drag polars from CFD results with turbulent inlet flow had more gradual curves as compared to experimental results. Also, the CFD Maintaining a constant velocity may change the drag polar for the wind tunnel model to one more similar to either of the CFD results. In addition, measuring the turbulence properties at inlet will improve the accuracy of the CFD results. Further mesh refinement may also be needed to better capture the boundary layer which would improve the drag measurement. Another difference between the experimental and CFD results was the change in drag with the addition of the SCF. Based on the unmodified CFD drag polars, the SCF had negligible effects on the drag. However, based on experimental results, the SCF noticeably shifted the drag polar. This shift in drag was possibly due to the increased number of geometric features (slat cusp, spaces between SCF sections and imperfections associated with assemblage of those features.).
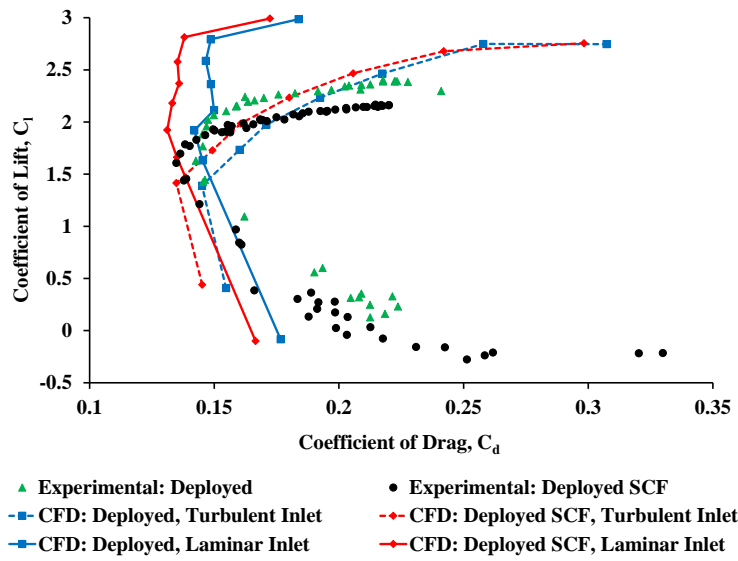
Figure 4.13: Comparison of CFD and wind tunnel drag polars for the deployed configuration.

110

(a) 4° angle of attack.   (b) 6° angle of attack.   (c) 8° angle of attack.
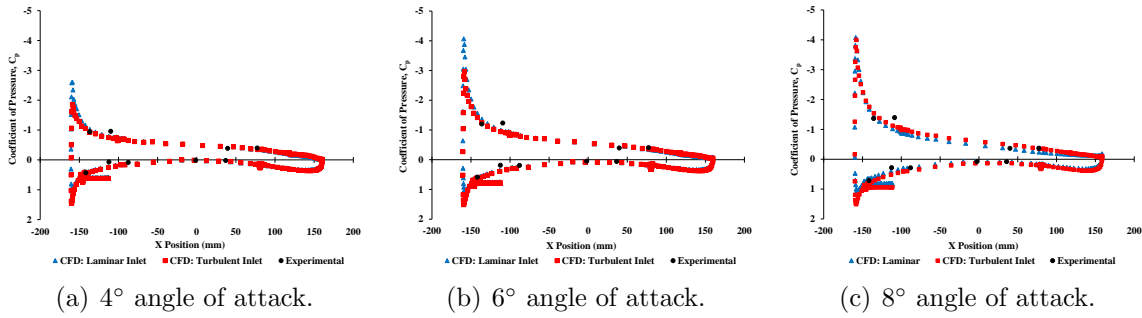
Figure 4.14: Comparison of coefficient of pressure distribution for CFD and experimental results in retracted configuration.

Pressure measurements along the surface of the main wing were taken for the retracted, deployed and deployed with SCF configurations at 4°, 6° and 8° angle of attack. The coefficient of pressure distributions from wind tunnel testing and CFD analysis for the retracted configuration are compared in Fig. 4.14. Note that three of the pressure ports were covered by the retracted slat so pressure measurements As seen in the figure, the distribution from CFD analysis for both inlet casesmatched well with the experimental results at all angles of attack. This was expected since the experimental and CFD lift-AoA curves were similar.

Figures 4.15 and 4.16 show the coefficient of pressure distribution for both deployed configurations from CFD analysis and wind tunnel testing. As with the results for the retracted configuration, the distribution from CFD analysis for both deployed configurations was close to the experimental results in terms of value and overall shape of the distribution. Both the characteristics on the lower surface and trailing edge of the upper surface were accurately captured. The main difference between experimental and CFD results were the values at the leading edge of the main wing. Experimental results showed a higher suction peak on the upper surface than the CFD results. In addition, as the angle of attack increased, the difference

111

between CFD and experimental results grew. The pressure distribution on the main wing from CFD analysis for both configurations was approximately the same indicating that the SCF did not significantly affect the distribution on the main wing. However, pressure distributions from experimental results showed that the deployed with SCF configuration had a higher suction peak at the leading edge than the distribution from the deployed configuration. Away from the upper surface of the leading edge, the experimental distribution for both configurations was approximately the same. In general, the pressure distribution from CFD analysis with laminar flow better matched the experimental results since it had a higher suction peak at the leading edge of the main wing.

(a) 4° angle of attack.   (b) 6° angle of attack.   (c) 8° angle of attack.
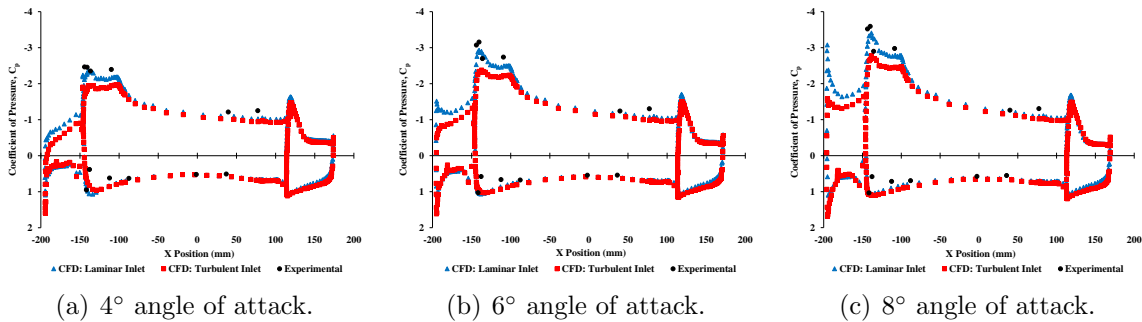
Figure 4.15: Comparison of coefficient of pressure distribution for CFD and experimental results in deployed configuration.

Measurements of the SCF displacement response were attempted. The laser was aimed at the region of the SCF with the largest displacement in FSI analysis. However, the surface of the SMA SCF was highly reflective and the location where the laser was aimed was very close to the surface of the main wing (which was white). Both of these caused significant scattering of the laser and thus significant scattering of the measured displacement. In addition, there appeared to be some slight rotation

(a) 4° angle of attack.　　(b) 6° angle of attack.　　(c) 8° angle of attack.
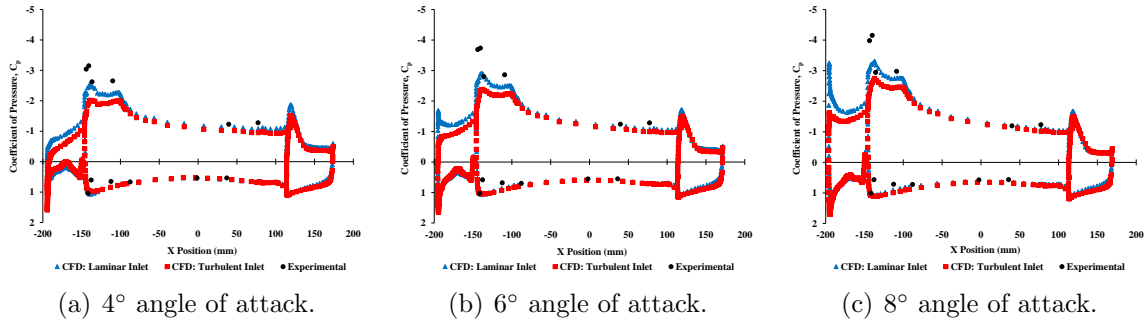
Figure 4.16: Comparison of coefficient of pressure distribution for CFD and experimental results in deployed with SCF configuration.

of the slat when the tunnel was turned on, resulting in a shift of the SCF by a few millimeters. Future work will need to address the rotation of the slat and reduce the reflectiveness of the SCF.

Wind tunnel testing was also conducted for a 14% retracted slat configuration where the SCF was touching the main wing. Figure 4.17(a) shows the lift-AoA curve for the 14% retracted configuration in comparison to the curve from the fully deployed configuration, both with the SCF. The lift for both configurations was approximately the same at every angle of attack. With regards to computational results, at 6° angle of attack, for the 14% retracted slat configuration, FSI analysis predicted a lift coefficient of 2.4, which was slightly higher (5%) than the lift coefficient for the fully deployed configuration. The measured drag polar for the 14% retracted slat configuration was similar in shape to the corresponding polar for the fully deployed configuration (see Fig. 4.17(b)). However, the values of the drag coefficient were different between these two configurations. At low angles of attack, the drag from the 14% retracted slat configuration was significantly larger than the fully deployed configuration. The difference in drag between the two configurations decreased at higher angles of attack till there was no difference. Computational results predicted

113

only a 3% increase in drag which was comparable to the experimental results at high values of lift. More angles of attack need to be considered in the FSI analysis for the 14% retracted slat configuration to make better comparisons to experimental results regarding lift and drag.

Pressure along the surface of the main wing was also measured for the 14% retracted slat configuration. Figure 4.17 shows the pressure coefficient distribution at 6° angle of attack for both experimental and computational results. The distribution from computational analysis was close to the experimental results in terms of value and overall shape of the distribution. Characteristics of the distribution were accurately captured on both the upper and lower surfaces. In addition, the computational results seemed to better match the measured pressure at the suction peak than either fully deployed case.

(a) Lift-AoA curve.

(b) Drag polar.
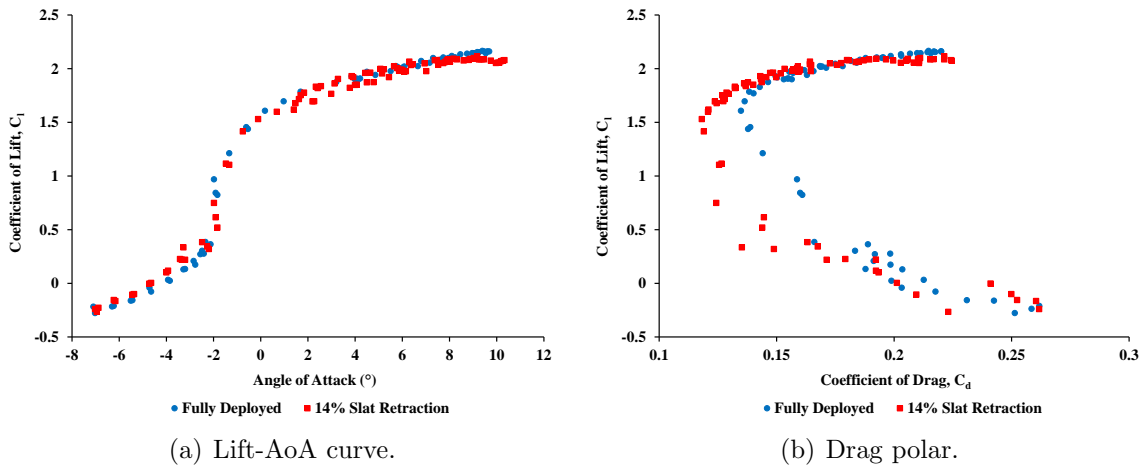
Figure 4.17: Comparison of lift and drag for fully deployed and 14% retracted slat configurations.
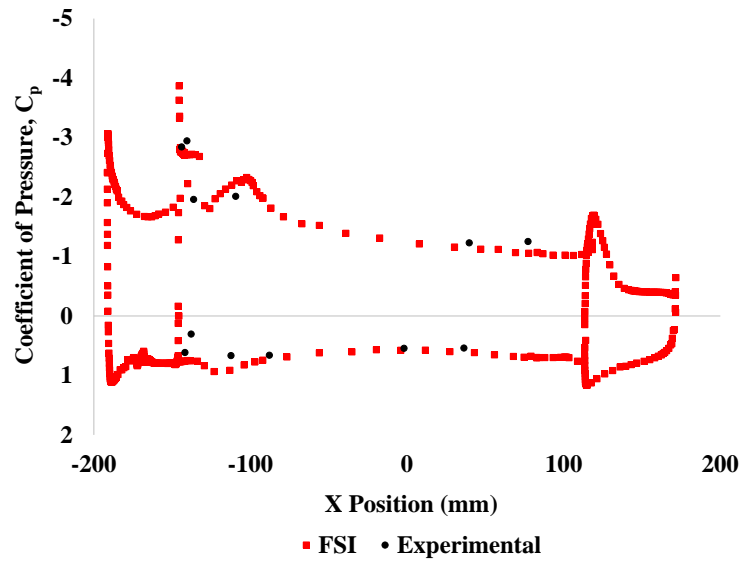
Figure 4.18: Comparison of coefficient of pressure distribution for CFD and experimental results at 14% slat retraction.

5. CONCLUSIONS AND FUTURE WORK

5.1 Summary and Conclusions

The goal of this work was to further the development and understanding of a SMA SCF that would reduce the noise produced by the wing of a typical transport-class aircraft using both computational and physical models. Specifically this work focused on three tasks: 1) develop and optimize a structural model of the SCF considering aerodynamic and retraction/deployment load cases, 2) develop and analyze CFD and FSI models of a scaled SCF at various angles of attack and slat/flap deployment and 3) develop and test a scaled wind tunnel model of the SCF to validate computational models using experimental results.

To be a viable addition to known and desirable airframe configurations, the SCF needed to satisfy three contradictory characteristics: 1) stiffness during aerodynamic loading, 2) compliance for morphing during slat retraction and 3) low weight. These characteristics drove designers to consider shape memory alloys. Finite element analysis models of a physical benchtop prototype were constructed to perform analysis-driven design optimization using a proven framework. Design of experiment studies were first conducted to understand how the design variables influenced model response and to more efficiently perform the optimization. It was found that an approximately-monolithic, short-hinge SCF with a forward flexure thickness of $0.103\,\mathrm{cm}$ and an aft flexure thickness of $0.0975\,\mathrm{cm}$ minimized the actuation force. This design was similar to the physical model developed by NASA engineers.

The success of the design optimization motivated further studies into the SMA SCF concept. Work specifically focused on how the SCF behaved under flow using computational models. The computational tools consisted of finite element structural

models and finite volume fluid models based on a wind tunnel model of a scaled 2D section of the Boeing-NASA CRM. Prior to FSI analysis of the SCF, CFD analysis was performed on multiple configurations of the CRM to examine how flow characteristics were affected by the SCF. Results from CFD analysis showed significant increases in lift for the deployed configurations relative to the retracted configuration.

Also, incorporation of the SCF eliminated the circulating flow region in the slat cove without significantly effecting the overall flow characteristics, complying with known SCF behavior. This was mirrored in the drag polars and pressure distributions. Two inlet flow cases were also considered: laminar flow and fully developed turbulent flow.

FSI analysis of the fixed-fully-deployed case at two angles of attack with an inlet speed of $15\,\mathrm{m/s}$ resulted in a maximum SCF displacement of approximately $0.03\,\mathrm{mm}$, which was similar to the displacement of a static analysis of the SCF. There was some fluctuation in the SCF displacement, however the amplitude and frequency of this fluctuation suggested that it might be due to numerical noise in the analysis. FSI analysis was also conducted for the case of the SCF touching the main wing (14% slat retraction). At this retraction level, the SCF prevented air from flowing around the leading edge of the main wing. This essentially made it an extension of the main wing. Finally, FSI analysis of full slat retraction was conducted, but the analysis crashed at 94% retraction due to a zero volume element. This was possibly the first FSI analysis of a morphing structure on a moving rigid body relative to fixed rigid body with massive changes in volume. Overset meshes were used to assist with the deformation of the SCF in the fluid model during FSI analysis which introduced local disturbances into the flow. However, the disturbances did not appear to significantly alter the flow in the vicinity of the wing.

A scaled physical wind tunnel model of the CRM geometry was built and tested

for the purpose of validating computational results. This model incorporated the first flexible SMA SCF in a wind tunnel. The lift-AoA curves from wind tunnel testing and CFD analysis had similar trends for both the retracted and deployed configurations. In general for all configurations, the CFD model had lower drag than the wind tunnel model. However, shifting the CFD drag polar such that the drag at 0° was the same for both experimental and computational results, showed that the polars were of similar shape. This may have been due to surface roughness, some geometric features not captured in the CFD model and side wall effects. The pressure distributions along the main wing from CFD and experimental results matched well except for the upper surface near the suction region for both deployed configurations which would be sensitive to angle of attack. Attempts were made to measure the displacement of the SCF, but the surface of the SCF was too reflective and slat appeared to rotate slightly when the tunnel was activated preventing accurate readings.

5.2   Future Work

Future work will continue the development of the computational models. Improvements of the overset mesh will be investigated to remove the downstream propagation of the local disturbances at the mesh boundaries. This in turn will improve the overall accuracy of the analysis. Additionally, measurement of the turbulence properties will be conducted in order to more accurately model the flow of the inlet. Future work will also focus on the further development of the wind tunnel model. During this work, slight rotations of the model may have caused some wing twist and prevented accurate measurements of the SCF displacement. Reinforcing the model and developing means to account for the rotation will improve these measurements. To observe more aeroelastic responses in the computational and physical models, a thinner SMA may be considered. Finally, future work will consider the creation of

nonlinear reduced order models for the SCF under flow. The current implementation is not feasible for use in a design optimization due to the exceptionally long runtimes. Reduced order models will significantly reduce the runtime allowing for analysis of the SCF under flow to be considered in design studies.

REFERENCES

[1] M. Khorrami and D. Lockard. Effects of geometric details on slat noise generation and propagation. *AIAA Paper*, 2664, 2006.

[2] K. Mau and W. Dobrzynski. Aerodynamic noise reducing structure for aircraft wing slats. US Patent 6,789,769, 2004.

[3] W. Gleine, K. Mau, and U. Carl. Aerodynamic noise reducing structure for aircraft wing slats. US Patent 6,394,396, 2002.

[4] C. Streett, J. Casper, D. Lockard, M. Khorrami, R. Stoker, R. Elkoby, W. Wenneman, and J. Underbrink. Aerodynamic noise reduction for high-lift devices on a swept wing model. *AIAA Paper*, 212, 2006.

[5] W. Horne, K. James, T. Arledge, P. Soderman, N. Burnside, and S. Jaeger. Measurements of 26 percent-scale 777 airframe noise in the nasa ames 40 by 80 foot wind tunnel. *AIAA Paper*, 2810, 2005.

[6] T. Imamura, H. Ura, Y. Yokokawa, S. Enomoto, K. Yamamoto, and T. Hirai. Designing of slat cove filler as a noise reduction device for leading-edge slat. *AIAA Paper*, 3473, 2007.

[7] L. Campanile. Lightweight shape-adaptable airfoils: A new challenge for an old dream. In D. Wagg, I. Bond, P. Weaver, and M. Friswell, editors, *Adaptive Structures: Engineering Applications*, pages 89–135. John Wiley and Sons, Chichester, UK, 2007.

[8] W. Scholten, D. Hartl, T. Turner, and R. Kidd. Development and analysis-driven optimization of a superelastic slat-cove filler for airframe noise reduction. *AIAA Journal*, 54(3):1078–1094, 2015.

[9] D. Hartl and D. Lagoudas. Aerospace applications of shape memory alloys. *Proceedings of the Institution of Mechanical Engineers, Part G: Journal of Aerospace Engineering*, 221(4):535–552, 2007.

[10] D. Hartl, D. Lagoudas, and F. Calkins. Advanced methods for the analysis, design, and optimization of sma-based aerostructures. *Smart Materials and Structures*, 20(9):094006, 2011.

[11] S. Oehler, D. Hartl, R. Lopez, Malak R., and D. Lagoudas. Design optimization and uncertainty analysis of sma morphing structures. *Smart Materials and Structures*, 21(9):094016, 2012.

[12] C. Lan, J. Wang, and C. Fan. Optimal design of rotary manipulators using shape memory alloy wire actuated flexures. *Sensors and Actuators A: Physical*, 153(2):258–266, 2009.

[13] R. Widdle, M. Grimshaw, and M. Shome. Optimal design of a shape memory alloy actuated composite structure with iterative finite element analysis. *Proceedings of SPIE*, 7288, 2009.

[14] G. Dumont and C. Kuhl. Finite element simulation for design optimization of shape memory alloy spring actuators. *Engineering computations*, 22(7):835–848, 2005.

[15] O. Ozbulut, P. Roschke, P. Lin, and C. Loh. Ga-based optimum design of a shape memory alloy device for seismic response mitigation. *Smart Materials and Structures*, 19(6):065004, 2010.

[16] F. Calkins, J. Mabe, and G. Gutler. Boeing's variable geometry chevron: morphing aerospace structures for jet noise reduction. *Proceedings of SPIE*, 6171, 2006.

[17] D. MacPhee and A. Beyene. Fluid-structure interaction of a morphing symmetrical wind turbine blade subjected to variable load. *International Journal of Energy Research*, 37(1):69–79, 2011.

[18] H. Heo, J. Ju, and D. Kim. Compliant cellular structures: Application to a passive morphing airfoil. *Composite Structures*, 106:560–569, 2013.

[19] K. Maute and G. Reich. Integrated multidisciplinary topology optimization approach to adaptive wing design. *Journal of Aircraft*, 43(1):253–263, 2006.

[20] D. Willis, E. Israeli, P. Presson, M. Drela, and J. Peraire. A computational framework for fluid structure interaction in biologically inspired flapping flight. *AIAA Paper*, 3473, 2007.

[21] S. Daynes and P. Weaver. Design and testing of a deformable wind turbine control surface. *Smart Materials and Structures*, 21(10):105019, 2012.

[22] C. Nam, A. Chattopadhyay, and Y. Kim. Application of shape memory alloy (sma) spars for aircraft maneuver enhacement. *Proceedings of SPIE*, 226, 2002.

[23] J. Strelec, D. Lagoudas, M. Khan, and J. Yen. Design and implementation of a shape memory alloy actuated reconfigurable airfoil. *Journal of Intelligent Material Systems and Structures*, 14(4-5):257–273, 2003.

[24] S. Oehler, D. Hartl, T. Turner, and D. Lagoudas. Modeling fluid structure interaction with shape memory alloy actuated morphing aerostructures. *Proceedings of SPIE*, 8343, 2012.

[25] S. Barbarino, E. Flores, R. Ajaj, and M. Friswell. A review on shape memory alloys with applications to morphing aircraft. *Smart Materials and Structures*, 23(6):063001, 2014.

[26] R. Ruggeri and D. Arbogast. Wind tunnel testing of a lightweight 1/4-scale actuator utilizing shape memory alloy. *Proceedings of SPIE*, 6930, 2008.

[27] J. Kudva. Overview of the darpa smart wing project. *Journal of Intelligent Material Systems and Structures*, 15(4):261–267, 2004.

[28] A. Popov, T. Girgorie, and R. Botez. Modeling and testing of a morphing wing in open-loop architecture. *Journal of Aircraft*, 47(3):917–923, 2010.

[29] T. Turner, R. Kidd, D. Hartl, and W. Scholten. Development of a sma-based slat-cove filler for reduction of aeroacoustic noise associated with transport-class aircraft wings. *ASME 2013 Conference on Smart Materials, Adaptive Structures and Intelligent Systems*, 3100, 2013.

[30] *Metallic Materials Properties Development and Standardization (MMPDS-08)*. Battelle Memorial Institute, 2013.

[31] D. Lacy and A. Sclafani. Development of the high lift common research model (hl-crm): A representative high lift configuration for transonic transports. *AIAA Paper*, 0308, 2016.

[32] Dassault Systemes of America Corp., Woodlands Hills, CA. *Analysis User's Manual*, 2011.

[33] Phoenix Integration, Philadelphia, PA. *Model Center 9.0 User's Manual*, 2009.

[34] D. Lagoudas, Z. Bo, and M. Qidwai. A unified thermodynamic constitutive model for sma and finite element analysis of active metal matrix composites. *Mechanics of Composite Materials and Structures*, 3(2):153–179, 1996.

[35] D. Lagoudas, D. Hartl, Y. Chemisky, L. Machado, and P. Popov. Constitutive model for the numerical analysis of phase transformation in polycrystalline shape memory alloys. *International Journal of Plasticity*, 32:155–183, 2012.

[36] ASTM International. F-2516: Standard test method for tension testing of nickel-titanium superelastic materials. 2006.

[37] D. Lagoudas (Editor). *Shape Memory Alloys: Modeling and Engineering Applications.* Springer Science+Business Media LCC, New York, NY, 2008.

[38] A. Bertram. *Elasticity and Plasticity of Large Deformations: An Introduction.* Springer Science+Business Media LCC, New York, NY, 2005.

[39] W. Scholten, T. Turner, and D. Hartl. Analysis-driven design optimization of a sma-based slat-cove filler for aeroacoustic noise reduction. *ASME 2013 Conference on Smart Materials, Adaptive Structures and Intelligent Systems*, 3104, 2013.

[40] J. Vassberg, M. DeHann, S. Rivers, and R. Wahls. Development of a common research model for applied cfd validation studies. *AIAA Paper*, 6919, 2008.

[41] J. Heeg, C. Spain, and J. Rivera. Wind tunnel to atmospheric mapping for static aeroelastic scaling. *AIAA Paper*, 2044, 2004.

[42] Software Cradle Co., Ltd., Woodlands Hills, CA. *SC/Tetra User's Guide*, 2015.

[43] F. Menter. Zonal two equation k-ω turbulence models for aerodynamic flows. *AIAA Paper*, 2906, 1993.

[44] David C. Wilcox. *Turbulence Modeling for CFD.* DCW Industires, Inc., 1998.

[45] ASTM International. E345:standard test methods of tension testing of metallic foil. 2016.

[46] P. Spalart and S. Allmaras. A one-equation turbulence model for aerodynamic flows. *AIAA Journal*, 94, 1992.

APPENDIX A

MESH AND PRISM LAYER STUDIES

A.1   Mesh Study

Mesh refinement studies were conducted on the CFD model in the fully deployed with SCF configuration at an angle of attack of 8°in order to obtain an accurate mesh that did not require a significant amount of computational runtime. It was assumed that obtaining a refined mesh for this configuration would be sufficient for obtaining accurate results for other configurations and angles of attack. The mesh study focused on setting the mesh sizes of the outer, middle and inner regions. Three mesh sizes were considered since flow results near the surface of the wing were more important than results at freestream. Different mesh sizes also significantly reduced computational runtime. During the study, the mesh size for one region would be changed while the mesh sizes for the other two regions would be held constant at a base size (12.8 mm, 1.6 mm and 0.4 mm for the outer, middle and inner regions, respectively). This study was conducted prior to the study of the prism layer so default parameters (3 layers, thickness based on element size) were used. In addition, inlet turbulence were set to default values (k=$0.0001\,m^2/s^2$ and $\varepsilon = 0.0001\,m^2/s^3$). During this study, changes in both the lift and drag coefficient were examined. Tables A.1, A.2 and A.3 show the results of the mesh studies. In general, the more refined the mesh was, the longer. Note that only four meshes sizes were considered for the inner region due to significant computational runtimes for fine meshes. For all meshes considered, the lift coefficient did not significantly change which means that a coarse mesh would be sufficient to capture the pressure distribution (and thus the lift) of

the wing. However, there was significant variation in the drag coefficient. For both the outer and middle regions, there was a approximately 10% difference between the minimum and maximum drag coefficients. Changes to the inner region exhibited significantly more variation in the drag coefficient. This was expected since the prism layer elements (and thus the boundary layer) were directly effected by the mesh size of the inner region. A prism layer study would better capture the boundary layer and thus the drag coefficient than significant mesh refinement of the inner region. Based on the low variation of lift coefficient, the mesh sizes for the outer and middle regions were set to 25.6 mm and 6.4 mm, respectively. The mesh size for the inner region was set to 0.8 mm since prism layer studies would better refine the mesh near the surface of the wing. This refined mesh resulted in a lift coefficient of 2.88 and a drag coefficient of 0.0872 which were to values observed in the mesh study.

Table A.1: Mesh study of outer region.

Element Size (mm)	25.6	12.8	6.4	3.2	1.6
C_L	2.779	2.815	2.777	2.790	2.720
C_D	0.116	0.108	0.106	0.119	0.118
% change in C_L	-	1.31	-1.34	0.45	-2.50
% change in C_D	-	-6.43	-1.51	11.89	-0.89

A.2 Prism Layer Study

Prism layer elements were inserted along the surface of the wing and tunnel wall in order to improve the calculation of the boundary layer. Accuracy of the prism layer was dependent on the selection of the prism layer paramters: the thickness of

Table A.2: Mesh study of middle region.

Element Size (mm)	6.4	3.2	1.6	0.8	0.4
C_L	2.765	2.815	2.815	2.820	2.846
C_D	0.111	0.113	0.108	0.111	0.102
% change in C_L	-	1.80	-0.01	0.17	0.94
% change in C_D	-	1.84	-4.31	2.52	-8.09

Table A.3: Mesh study of inner region.

Element Size (mm)	1.6	0.8	0.4	0.2
C_L	2.810	2.845	2.815	2.879
C_D	0.0765	0.0934	0.108	0.0860
% change in C_L	-	1.27	-1.09	2.29
% change in C_D	-	22.19	15.74	-20.45

the first layer, change of thickness between layers and total number of layers (and in turn overall thickness of the prism layer). A preliminary study of the prism layer was conducted to find a prism layer that sufficiently captured the boundary layer. Note that the same prism layer was applied to each wall. As with the mesh study, it was assumed that a refined prism layer for one configuration (fully deployed SCF at an angle of attack of 8°) would be sufficient for all other configurations. At the time of this study, the Spalart-Allamaras (SA) turbulence model [46] was being used for CFD analysis. [1] To quickly assess multiple cases, the mesh size of the inner region

---

[1]The SA turbulence model was not chosen as the final turbulence model due to its significant dependence on the element size of the inner region and it required significant computational runtime to converge to a near steady solution for refined meshes.

was set to 0.0016 mm while the mesh sizes for the other regions were set to the sizes chosen in the mesh study. The study was split into two parts. The first part of the study focused on the effect of the total prism layer thickness while the second part focused on the thickness of the first layer (which directly effected the normalized wall distance y^+).

During the first part of the study, the thickness of the first layer was set to 0.04 mm while the number of layers and variation of thickness were adjusted to achieve different total thicknesses and keep the thickness of the last layer similar to the element size of the inner region. Table A.4 shows the variation of lift and drag with the total thickness. As shown in the table, the lift and drag converged as the total thickness of the prism layer was increased. A total thickness of 2.46 mm (Case 4) was chosen based on the results. The number of layers and variation for Case 4 were 12 and 1.27 respectively.

Table A.4: Total thickness of prism layer study.

Case	1	2	3	4	5
Total Thickness (mm)	1.04	1.58	2.02	2.46	2.97
C_L	2.62	2.44	2.38	2.34	2.33
C_D	0.0886	0.118	0.122	.122	0.121
% change in C_L	-	-6.74	-2.72	-1.48	-0.254
% change in C_D	-	33.1	3.46	-0.344	-0.893

The prism layer parameters from Case 4 were used as the initial case for the second part of the prism layer study which evaluated the effect of the thickness of the first layer. The thickness of the first layer directly corresponded to the normalized

128

wall distance y^+. During this portion of the study the total thickness was held to approximately 2.46 mm. As with the previous part of the study, the number of layers and variation of thickness were adjusted to a desired total thickness while keeping the thickness of the last layer similar to the inner region mesh size. Results for this portion of the study are shown in Table A.5. For all thicknesses considered, there was little change in either lift or drag. Also, as the thickness of the first layer decreased, the computational runtime increased. Since only the runtime increased with change in the thickness of the first layer, the prism layer parameters corresponding to Case 4 were chosen for CFD analysis of the CRM configurations. Note that for models used in FSI analysis, the same thickness of the first layer and total thickness were used, while the variation and number of elements were adjusted to prevent mesh distortion which resulted in more elements for the prism layer.

Table A.5: First layer thickness of prism layer study.

Case	4	6	7	8	
First Layer Thickness (mm)	0.04	0.03	0.02	0.01	0.003
$Maxy^+$	6.01	4.69	3.21	1.66	0.55
C_L	2.34	2.34	2.35	2.34	2.35
C_D	0.122	0.121	0.122	.122	0.122
% change in C_L	-	0.181	0.103	-0.111	0.134
% change in C_D	-	-0.745	1.21	-0.2	-0.0626